Westbrook, G.K., Carson, B., Musgrave, R.J., et al., 1994
Proceedings of the Ocean Drilling Program, Initial Reports, Vol. 146 (Part 1)

6. SITE 891[1]

Shipboard Scientific Party[2]

HOLE 891A

Date occupied: 24 October 1992

Date departed: 25 October 1992

Time on hole: 1 day, 2 hr

Position: 44°38.648′N, 125°19.550′W

Bottom felt (rig floor; m, drill-pipe measurement): 2674.3

Distance between rig floor and sea level (m): 11.0

Water depth (drill-pipe measurement from sea level; m): 2663.3

Total depth (rig floor; m): 2683.8

Penetration (m): 9.5

Number of cores (including cores with no recovery): 3

Total length of cored section (m): 9.5

Total core recovered (m): 9.49

Core recovery (%): 99

Oldest sediment cored:
Depth (mbsf): 9.5
Nature: clayey silt
Earliest age: Pleistocene

HOLE 891B

Date occupied: 25 October 1992

Date departed: 1 November 1992

Time on hole: 6 days, 20 hr, 53 min

Position: 44°38.660′N, 125°19.561′W

Bottom felt (rig floor; m, drill-pipe measurement): 2674.0

Distance between rig floor and sea level (m): 11.0

Water depth (drill-pipe measurement from sea level; m): 2663.0

Total depth (rig floor; m): 3146.3

Penetration (m): 472.3

Number of cores (including cores with no recovery): 58

Total length of cored section (m): 469.3

Total core recovered (m): 54.03

Core recovery (%): 11

Oldest sediment cored:
Depth (mbsf): 466.0
Nature: sandy silt
Earliest age: Pleistocene

HOLE 891C

Date occupied: 1 November 1992

Date departed: 6 November 1992

Time on hole: 4 days, 18 hr

Position: 44°38.638′N, 125°19.533′W

Bottom felt (rig floor; m, drill-pipe measurement): 2675.0

Distance between rig floor and sea level (m): 11.00

Water depth (drill-pipe measurement from sea level; m): 2664.0

Total depth (rig floor; m): 3167.0

Penetration (m): 492.0

Number of cores (including cores with no recovery): 0

Principal results: Ocean Drilling Program (ODP) Site 891 (proposed Site OM-3) lies on the westernmost ridge of the accretionary wedge at the foot of the Oregon continental margin, 2663 m below sea level (mbsl). The ridge is an anticlinally folded thrust sheet formed by movement along the frontal, landward-dipping fault that foots in the décollement beneath the wedge. The thrust fault is imaged on seismic-reflection profile OR-5 at a depth of about 375 m below seafloor (mbsf) at Site 891. The negative polarity of that reflector suggested that it may contain overpressured fluids or that more consolidated sediments, with higher density and seismic velocity, have been thrust over less consolidated footwall sediments. Site 891 was drilled to determine whether fluid advection occurred at this site and, if it did, whether it was focused along the fault zone or through stratigraphic aquifers elsewhere in the section. The realization of these objectives required analysis of the pore fluids and diagenetic products associated with them and determination of the physical properties and stratigraphic and structural characteristics of the entire section, particularly of the intervals that support flow.

Three holes were drilled at Site 891. Only three cores were collected using the advanced hydraulic piston corer (APC) in Hole 891A (total depth [TD] = 9.9 mbsf). Hole 891B provided cores to a depth of 472 mbsf although recovery was poor (11%). Hole 891C was drilled to 491 mbsf and logged with the geophysical and geochemical strings and the Formation MicroScanner (FMS). Both a vertical seismic profile (VSP) and a two-ship oblique seismic experiment (OSE) were conducted at Hole 891C.

Because of the poor recovery and the compositional and textural similarity of all sediments recovered at Site 891, only one lithostratigraphic unit was designated, which was divided into three subunits. Subunit IA (0–198.2 mbsf) displays cross-lamination, tilted beds, and convolute deformation. Subunit IB (198.2–383.9 mbsf) is marked by an increase in induration and fracturing, and a decrease in the degree of sorting. Subunit IC (383.9–472.3 mbsf TD) marks a return to less consolidated, less fractured, and better sorted sediments. The lithologies sampled consist dominantly of clayey silts and fine to medium sand. Allochthonous pebbles and diagenetic carbonate concretions are distributed randomly throughout the section. Several cores below 200 mbsf contain wood fragments.

Biostratigraphic and paleomagnetic results are consistent with a post-middle Pleistocene age for the entire column. The structural position, age, and composition of the sediments suggest that Site 891 accumulated as proximal deposits on Astoria Fan before uplift.

Steeply inclined turbidite beds that dip about 60° above 84 mbsf overlie variably dipping beds (0°–50°) to 198 mbsf. Deformation bands appear

---

[1] Westbrook, G.K., Carson, B., Musgrave, R.J., et al., 1994. *Proc. ODP, Init. Repts.,* 146 (Pt. 1): College Station, TX (Ocean Drilling Program).

[2] Shipboard Scientific Party is as given in the list of participants preceding the contents.

sporadically in the interval between 100 and 198 mbsf, but no other strain indicators are present above 198 mbsf. In contrast, numerous discrete fractures are visible in the intervals 198–278 and 321–375 mbsf. Two fault zones (263 and 375 mbsf) were recognized within these intervals by the development of shear fabrics and polished and slickenlined surfaces. Between the two fractured zones (278–321 mbsf), no shear fractures occur, but development of a bedding plane fissility suggests a compaction fabric. Below 375 mbsf, few fractures were observed and bedding dips 14°–20°.

Pore-water chemistry and physical properties define three distinct zones in Hole 891B. Zone 1 extends from the surface to 200 mbsf, coincident with Subunit IA. This interval is characterized by (1) porosity that declines regularly from about 50% at the seafloor to about 38% at depth; (2) low concentrations of methane and carbon dioxide and a virtual absence of higher hydrocarbons; (3) a low Cl^- concentration, the presence of sulfate, low alkalinity, and a stable Mg/Ca ratio. Zone 1 appears to be a region of normal gravitational compaction that is dominated by sulfate reduction.

Zones 2 and 3 do not coincide with the lithostratigraphic subunits. Zone 2, between 200 and 440 mbsf, differs significantly from Zone 1, and there appears to be little hydraulic communication between the two. Methane concentrations increase abruptly in Zone 2 and vary sympathetically with the organic carbon content, which indicates bacterial methanogenesis. Ethane, higher hydrocarbons, and carbon dioxide appear below 240 mbsf and define maxima at 314, 340, 367, and 410 mbsf. These maxima represent incursions of thermogenic (hydrothermal) hydrocarbons that indicate at least localized fluid advection. The presence of the olefin ethene (C_2H_4), which is unstable, suggests that the fluid dispersal system is active. The total nitrogen/organic carbon ratio indicates that organic components have a mixed terrestrial/marine origin. Concentrations of Cl^- in Zone 2 are high and relatively constant, SO_4^{2-} is absent, and Mg^{2+} is low. These concentrations indicate that Zone 2 waters belong to a separate hydrologic system from those in Zone 1, and the interface between the two shows little evidence of diffusion between them. Carbonate cementation at 191 mbsf, which is suggested by high velocities (2.2 km/s) and high resistivities (2.6 Ωm) measured by the logs, may form a barrier to fluid exchange.

Fault zones or intervals of anomalous compaction produce several discontinuities (at 260, 308, 375, and 440 mbsf) in the porosity distribution in Zone 2. The two upper zones/intervals are apparent in the pore water (Li^+, Mg/Ca ratio, and SiO_2) and gas (ΣC_2–C_6) chemistry; these anomalies probably reflect flow along permeable faults or sand beds. The lack of a significant geochemical anomaly at 375 mbsf suggests that the thrust imaged on the seismic-reflection profile may support little or no active fluid flow.

Zone 3 lies below 440 mbsf and is defined primarily on the basis of a pronounced increase in porosity (from 40% to 60%) at this depth. Fluids beneath this boundary exhibit consistently high values of methane and low concentrations of higher hydrocarbons and carbon dioxide. The pore waters are also characteristically low in Cl^- and high in Ca^{2+}, suggesting that they have been affected by clay dehydration reactions. Zone 3 appears to represent the footwall section beneath the frontal thrust fault. The porosity inversion and geochemical signature suggest that the active portion of the frontal thrust may have stepped down to the section between 412 and 437 mbsf.

The pore-water chemistry in Hole 891A (0–9.9 mbsf) is substantially different from that characteristic of seawater or of Zone 1 in Hole 891B. The concentrations of Cl^-, SiO_2, phosphate, Mg^{2+}, Na^+, and Ca^{2+} are similar to those observed in Zone 2, suggesting a minimum depth of origin of 200 mbsf. The disparity in pore-water composition between Holes 891A and 891B, which are separated by 30 m, emphasizes the spatial heterogeneity of fluid flow in this accretionary setting.

BACKGROUND AND OBJECTIVES

Site 891 (proposed Site OM-3) lies at the foot of the continental slope off central Oregon, at a depth of 2663 mbsl (Fig. 1). The site is situated at 44°38.66′N, 125°19.56′W, in a small, headless submarine canyon that incises a portion of the lowermost ridge of the continental slope. The ridge is the surficial expression of an anticlinally folded thrust sheet that overlies a landward-dipping fault (Fig. 2). The fault, which is inferred to be a significant aquifer, was the primary target at Site 891.

Cascadia Basin sediments lie immediately west of the ridge and Site 891 (Fig. 2). These deposits are 3.5–4.0 km thick (MacKay et al., 1992), and the upper portion of the section is dominated by thick, upper Pleistocene sands associated with the southern reaches of the Astoria Fan. These silty sands overlie silt turbidites characteristic of the lower, abyssal plain deposits (von Huene and Kulm, 1973) above oceanic basement. Incipient thrust faults (protothrust zone; Fig. 2) occur in the Cascadia Basin deposits as much as 6 km west of the surface trace of the frontal thrust. These blind faults extend to within 800 m of basement and may be important conduits by which the undeformed basin deposits initially dewater before uplift (Carson et al., 1991).

The marginal ridge is a seaward-vergent ramp anticline that is cut by a prominent, westward-dipping backthrust and several related, secondary faults (Moore et al., 1990; MacKay et al., 1992). The basal décollement of the accretionary wedge, in which the frontal thrust is rooted, lies about 1.6 km above oceanic basement (Fig. 2). This geometry dictates that approximately 45% of the sedimentary section is, at present, underthrust beneath the toe of the wedge, and about 55% is accreted. The ridge stands 700 m above Cascadia Basin and extends approximately 10 km along strike. The northern end of the ridge is defined by a large submarine canyon (Fig. 1) and the southern end by a left-lateral, strike-slip fault (Goldfinger et al., 1992). The eastern limb of the anticline lies unconformably beneath a cover of turbidites that fills a lower slope basin (Lewis and Cochrane, 1990). Biostratigraphic ages derived from the top of the anticline indicate that the ridge was elevated less than 4.5×10^5 yr ago (Kulm et al., 1986).

The seaward limb of the ridge anticline is exposed in the two submarine canyons that incise it: the large canyon at the northern end of the ridge and the small canyon in which Site 891 was drilled. Detailed mapping and sampling in these canyons (Moore et al., 1990) indicate that the ridge is composed of thinly to thickly bedded silty sands and interbedded silty clays. The canyon where Site 891 is located is cut by a prominent 10-m scarp downslope from the site at a depth of 2770 mbsl, which is probably the surface trace of the frontal thrust (Moore et al., 1990). Outcrops in the upper portion of the canyon reveal rollover from seaward- to landward-dipping bedding. Evidence for fluid venting, which consists of numerous clam shells, bacterial mats, and carbonate crusts, was found at both the fault trace at 2770 mbsl and near the top of the canyon (2150–2250 mbsl). In the former occurrence, the flow indicators are clearly fault controlled; in the latter, fluid venting appears to be stratigraphically controlled, as it occurs at the apex of the fault-propagation fold and probably reflects seaward flow along a landward-dipping, permeable interval (Moore et al., 1990).

The primary objectives at Site 891 were to sample the pore fluids within the frontal thrust fault, to measure their temperature, to determine the in-situ permeability of the fault zone, and to characterize the changes in physical properties associated with the structural elements and with diagenesis. We hoped to determine if fluids moving along the fault originate from source zones as deep as 3 km within the accretionary complex or within the underlying, underthrust sedimentary sequence.

SEISMIC STRATIGRAPHY

The available seismic-reflection data define well the geometry of the major structures of the seaward-verging portion of the Oregon accretionary prism. The line drawings of time and depth sections (Figs. 2–3) clarify the major structural features; the actual seismic data are presented in a separate chapter in larger scale format (Moore et al., this volume), and details of the seismic-reflection profiles are discussed in the "Downhole Logging" section (this chapter).

Along line OR89-05, the upper 1.6 km of the incoming section is scraped off whereas the lower 1.6 km is underthrust. The deformation

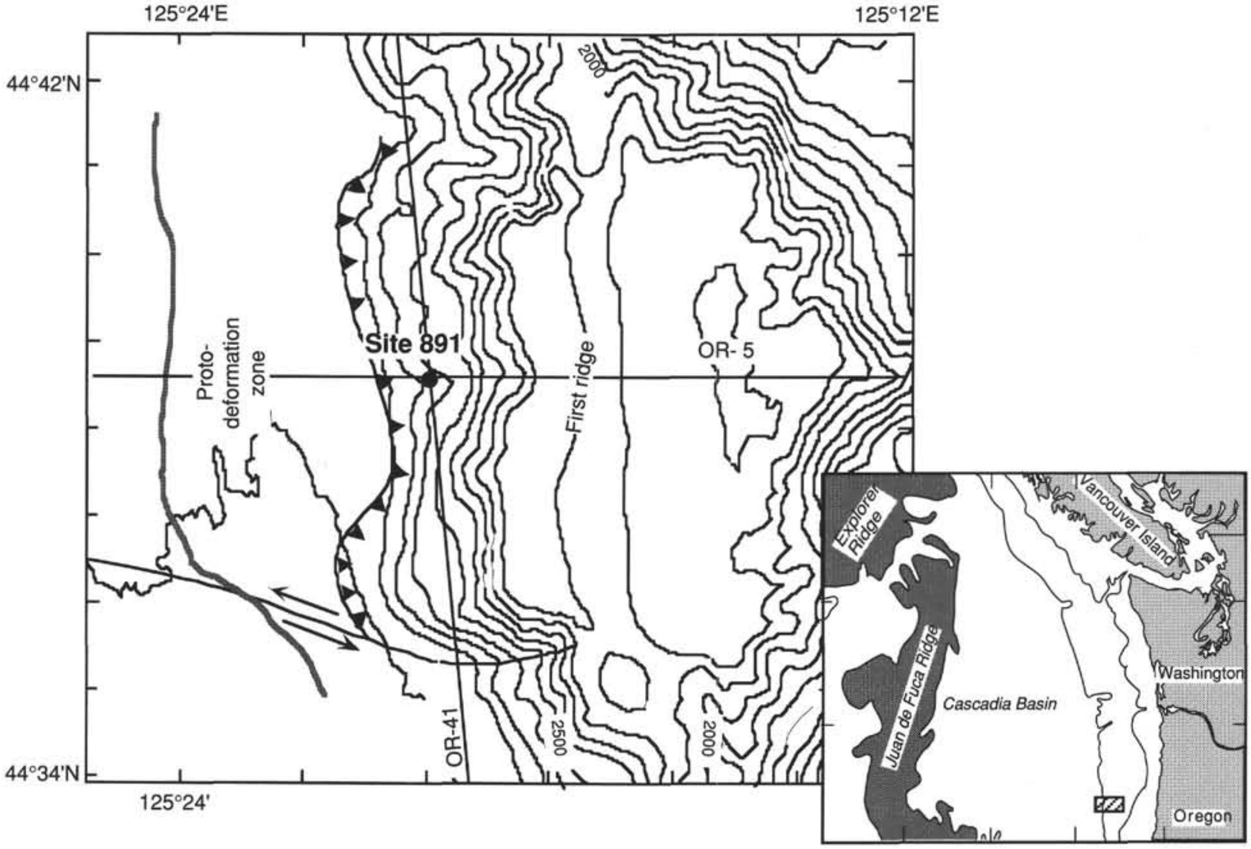

Figure 1. Position of Site 891, seismic reflection lines OR-5 and OR-41, and adjacent bathymetry on the Oregon continental margin. The seaward extent of the protothrust zone is indicated by the stippled gray line, and the location of the thrust fault trace is shown by the heavy, toothed line.

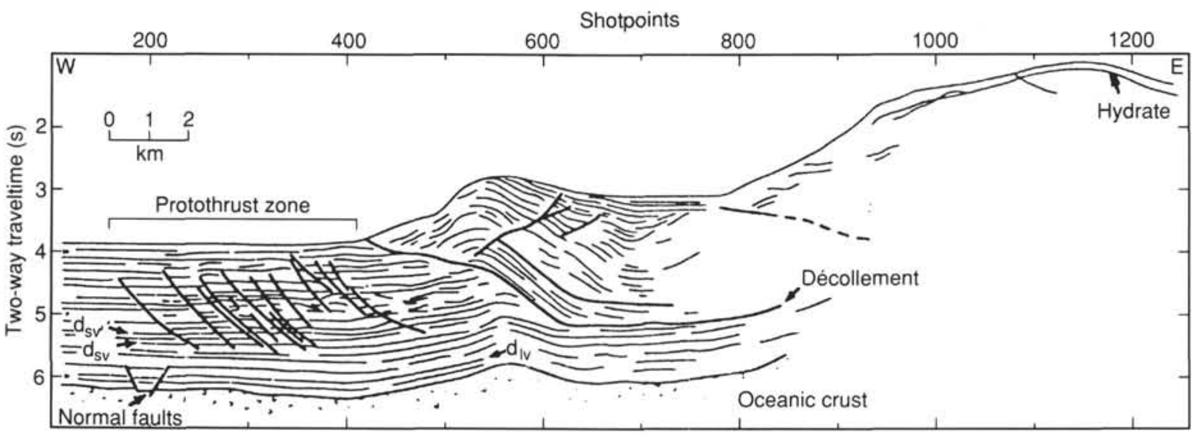

Figure 2. Line drawing of multichannel seismic line OR-5 (from MacKay et al., 1992). Site 891 is located at Shotpoint 440. Vertical exaggeration is approximately 2:1 at the seafloor.

front is marked by protothrusts that develop about 6 km seaward of the base of the slope. These faults commonly dip about 45° landward and root near the stratigraphic level of the décollement (Fig. 3). On closely adjacent parallel seismic lines, landward-dipping protothrusts are complemented by seaward-dipping conjugate thrusts. The frontal thrust emerges at the base of the slope and consists of a ramp dipping 20° east. The deepest rollover of the hanging wall indicates the overthrust sediment was been displaced 2.7 km along the ramp with a throw or vertical rise of 1 km.

Portions of the frontal thrust and protothrusts display negative polarity reflections. Such reflections here and elsewhere along the Oregon Margin have been interpreted as dilational zones associated with excess pore pressures (Moore et al., 1991; MacKay et al., 1992). However, the substantial throw on the frontal thrust suggests that a simple inversion of higher velocity and density sediment over lower velocity and density sediment could explain some of the negative polarity reflections; elsewhere, especially in the protothrust zone, negative polarity reflections may be the result of dilation.

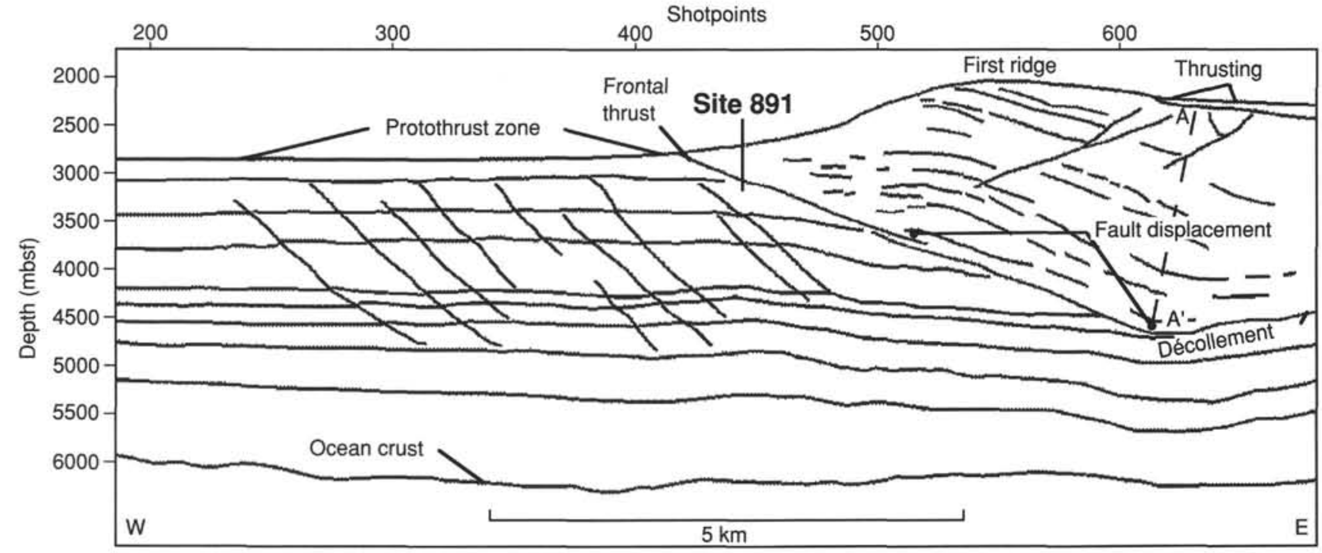

Figure 3. Depth section along seismic line OR89-05. Fault displacement was determined by the distance that "cut-off" layers have moved up the frontal thrust ramp from the décollement. The décollement and subjacent oceanic crust appear to rise in a landward direction, probably because inappropriately low velocities were used in this area of the depth section. Dashed line A–A′ is discussed in the text.

Active thrusting displaces the seabed on the landward side of the first ridge. These thrusts may be explained by a simple backthrust cutting across the ramp anticline or by compression in a synclinal fold formed above the intersection of the décollement and frontal thrust. The latter alternative is supported by the geometric coincidence of active surface thrusting along the upward continuation of the fold's axial plane (A–A′ in Fig. 3).

We restored the depth section to a prefaulted configuration (Fig. 4). Because the velocities, and presumably porosities, within the first ridge are nearly identical to those in the protothrust zone (Cochrane et al., this volume), no corrections were made for compaction in the restoration. Restoration of the first ridge to its prefaulted position produces a void in the seafloor as a result of erosion, subsidence of the fault ramp, and the rise of the current seafloor level because of sedimentation. The seabed at the restored Site 891 lies 800 m below the projected depth of the current abyssal plain (Fig. 4). Of this distance, about 300 m is because of subsidence of the footwall in response to loading during overthrusting (Fig. 4). The sediment accumulation since fold formation can be estimated from the age of the fold and rate of sedimentation during this time. Evaluation of the prism growth rates suggests that the fold formed since 0.25–0.30 Ma (see Westbrook, this volume). The accumulation rate of the Astoria

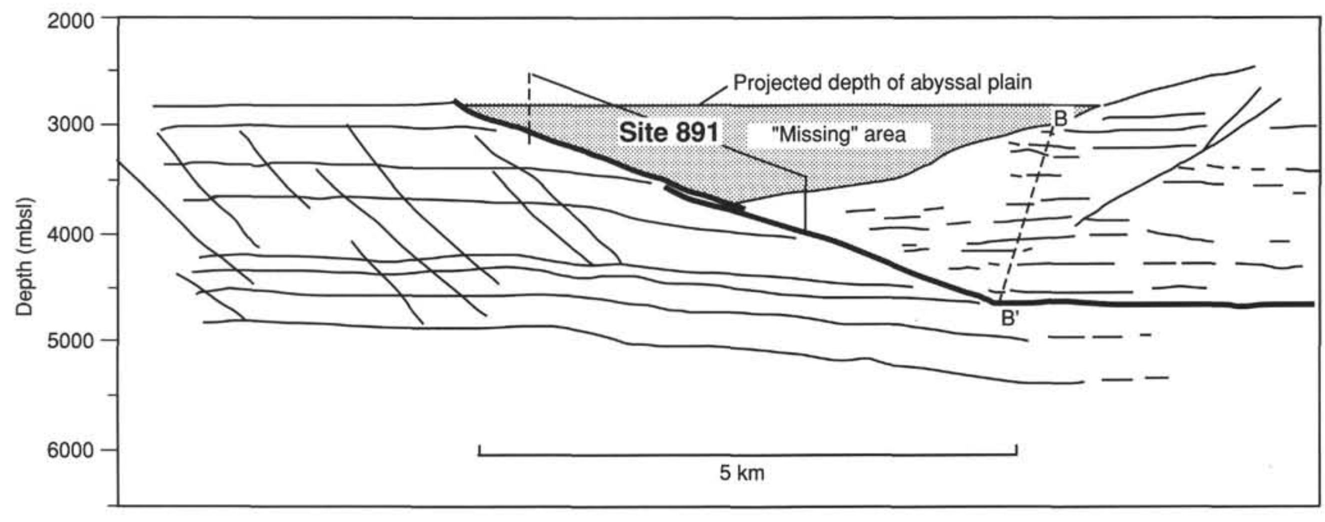

Figure 4. Restored cross section along seismic line OR89-05 was created by restoring displacement on the frontal thrust while preserving constant line lengths. Independently restoring the line lengths of reflectors implicitly assumes a flexural-slip mechanism of fold development, which is partially violated as evidenced by thrusting and thickening of the section on the landward flank of the first ridge. The décollement was flattened to account for the improbable seaward dip as shown on the depth section (Fig. 3). The "missing" area represents the cross-sectional area (actually volume) absent in the restoration. This deficit is explained by sedimentation since the formation of the fold, by subsidence of the footwall, and by erosion of the hanging wall. Dashed line B–B′ is the axial surface around which the fold was flattened. Landward of this line, the restored current seafloor exceeds the projected depth of the abyssal plain, which indicates thickening of the hanging wall. Because no slope basin deposits are apparent this far west, this thickening must be the result of structural processes (thrusting, layer-parallel shortening?) occurring as the hanging wall rides up the frontal thrust ramp.

Fan is estimated to be 370–940 m/m.y. at Site 174 (von Huene and Kulm, 1973); because the current drilling site is closer to the margin than Site 174 is, we used a sedimentation rate of 1000 m/m.y. Accordingly, 250–300 m of sediment has accumulated since the initiation of folding. Thus, the gross thickness of the missing section of 800 m is reduced by 500 m (300 m subsidence, 250–300 m sedimentation). The remaining missing section (200–250 m) is ascribed to erosion of the rising ramp anticline.

OPERATIONS

Site 891

The transit of about 270 nmi from Site 857 to Site 891 (prospectus Site OM-3) was made in 25 hr at an average speed of 10.9 kt. Weather conditions were moderating but remained rough for most of the move. Television reconnaissance of the seafloor and a jet-in test were conducted in anticipation of drilling a reentry hole. An extended core barrel/advanced piston corer (APC/XCB), bottom-hole assembly (BHA) was made up, and the APC spud of Hole 891A was observed on television.

Hole 891A

Seafloor depth in Hole 891A was established by the mud line in Core 146-891A-1H at 2663.3 mbsl (Table 1). Cores 146-891A-2H and -3H were stroked incompletely, and the advance-by-recovery technique resulted in only 9.5 m total advance for the three cores. An attempt at a fourth core also incompletely stroked, and the APC barrel became stuck outside the bit, forcing a round trip and ending Hole 891A.

Hole 891B

The drill string was run back to the seafloor and Hole 891B was spudded with an XCB core at 1000 Universal Time Coordinated (UTC), 26 October. The cause of the bent core barrel in Hole 891A appears to have been unconsolidated sand, which was also largely unrecoverable in the XCB cores. Core recovery was only 1.4% for the first 110 m. Water sampling-temperature probe (WSTP) runs were made at 30, 56, 92, 136, and 163 mbsf. Core recovery increased to about 10% in the interval between 110 and 160 mbsf. Core recovery with the motor-driven core barrel (MDCB) was attempted at 101 and 172 mbsf, with no recovery on the first attempt and 13% recovery on the second. Average recovery then increased to about 20% and persisted at this level to about 340 mbsf, where it dropped back to about 10%. Although no serious hole problems were encountered, hole fill of 1–5 m persisted on connections throughout the coring. Severe-weather and high-heave conditions for most of the interval made control of weight on bit extremely difficult and adversely affected core recovery.

An attempt to take a core with the pressure core sampler (PCS) core was made after Core 146-891B-43X at 339 mbsf. The PCS barrel, and a sinker bar/jar assembly run in on the wireline to retrieve it, became stuck in the pipe. Inability to circulate, or even to rotate the pipe, threatened to result in a stuck pipe. Eventually the barrel and sinker bar were freed, and normal circulation parameters were reestablished.

The drill string was run back to TD, where 14 m of fill was encountered. The fill was flushed from the hole with a 20-bbl mud sweep and XCB coring resumed. Heavy swells produced heave-compensator strokes of up to 5 m and reduced weight control on the bit to about ±20,000 lb. Alternating sand and clayey silt strata, together with the difficult environmental conditions, held core recovery to about 8%. Average recovery increased to 23% below about 440 mbsf, and hole conditions improved, with only about 1 m of fill noted on connections. At 472 mbsf, drilling objectives were declared fulfilled and preparations were begun for logging.

Table 1. Coring summary, Site 891.

Core no.	Date (October 1992)	Time (UTC)	Depth (mbsf)	Cored (m)	Recovered (m)	Recovery (%)
146-891A-						
1H	25	1300	0.0–4.7	4.7	4.67	99.3
2H	25	1510	4.7–7.3	2.6	2.63	101.0
3H	25	1600	7.3–9.5	2.2	2.19	99.5
Coring totals				9.5	9.49	99.9
146-891B-						
1X	26	1110	0.0–12.0	12.0	0.03	0.3
2X	26	1250	12.0–20.8	8.8	0.03	0.3
3X	26	1410	20.8–29.6	8.8	0.03	0.3
4X	26	1655	29.6–38.4	8.8	0.05	0.6
5X	26	1800	38.4–47.3	8.9	0.00	0.0
6X	26	1900	47.3–56.2	8.9	0.01	0.1
7X	26	2120	56.2–65.2	9.0	0.01	0.1
8X	26	2230	65.2–74.1	8.9	0.37	4.2
9X	26	2320	74.1–83.1	9.0	0.00	0.0
10X	27	0040	83.1–92.0	8.9	0.51	5.7
11X	27	0340	92.0–100.9	8.9	0.50	5.6
12N	27	0615	100.9–102.9	2.0	0.00	0.0
13X	27	0725	102.9–109.5	6.6	0.00	0.0
14X	27	0845	109.5–118.4	8.9	0.99	11.1
15X	27	1030	118.4–127.3	8.9	1.06	11.9
16X	27	1200	127.3–136.2	8.9	0.87	9.8
17X	27	1440	136.2–145.1	8.9	0.00	0.0
18X	27	1630	148.1–153.9	5.8	0.55	9.5
19X	27	1745	153.9–162.7	8.8	0.65	7.4
20X	27	2040	162.7–171.6	8.9	1.85	20.8
21N	27	2225	171.6–176.1	4.5	0.57	12.6
22X	28	0000	176.1–180.5	4.4	1.02	23.2
23X	28	0225	180.5–189.4	8.9	2.25	25.3
24X	28	0405	189.4–198.2	8.8	0.00	0.0
25X	28	0550	198.2–207.1	8.9	1.10	12.3
26X	28	0730	207.1–215.9	8.8	0.48	5.5
27X	28	0910	215.9–224.7	8.8	0.57	6.5
28X	28	1110	224.7–233.6	8.9	0.95	10.7
29X	28	1330	233.6–237.6	4.0	0.93	23.2
30X	28	1525	237.6–242.4	4.8	2.04	42.5
31X	28	1745	242.4–251.4	9.0	2.06	22.9
32X	28	1955	251.4–260.2	8.8	0.95	10.8
33X	28	2150	260.2–263.1	2.9	0.75	25.8
34X	28	2350	263.1–269.0	5.9	1.86	31.5
35X	29	0225	269.0–277.8	8.8	1.93	21.9
36P	29	0440	277.8–278.8	1.0	0.06	6.0
37X	29	0720	278.8–286.4	7.6	0.26	3.4
38X	29	0935	286.4–295.1	8.7	3.07	35.3
39X	29	1140	295.1–304.0	8.9	2.27	25.5
40X	29	1400	304.0–312.8	8.8	2.10	23.8
41X	29	1730	312.8–321.6	8.8	2.81	31.9
42X	29	1950	321.6–330.4	8.8	1.54	17.5
43X	29	2220	330.4–339.3	8.9	2.38	26.7
44X	30	1450	339.3–348.2	8.9	0.48	5.4
45X	30	1640	348.2–357.1	8.9	0.65	7.3
46X	30	1810	357.1–366.1	9.0	0.00	0.0
47X	30	2045	366.1–375.0	8.9	2.45	27.5
48X	30	2235	375.0–383.9	8.9	0.83	9.3
49X	31	0025	383.9–392.8	8.9	0.36	4.0
50X	31	0225	392.8–401.7	8.9	0.52	5.8
51X	31	0440	401.7–410.5	8.8	0.00	0.0
52X	31	0715	410.5–419.3	8.8	1.06	12.0
53X	31	0840	419.3–428.2	8.9	0.00	0.0
54X	31	1010	428.2–437.0	8.8	0.00	0.0
55X	31	1235	437.0–445.8	8.8	3.11	35.3
56X	31	1530	445.8–454.7	8.9	2.11	23.7
57X	31	1710	454.7–463.5	8.8	0.63	7.2
58X	31	1925	463.5–472.3	8.8	2.37	26.9
Coring totals				469.3	54.03	11.5

A wiper trip was made to 52 mbsf with an overpull of up to 60,000 lb experienced most of the way. Some drag persisted as the bit was run back down the hole. The drilling crew removed 54 m of fill from the hole, flushed the hole with 50 bbl of viscous mud, and pulled the bit to 97 mbsf for logging. While rigging for logging, a bridge formed under the bit and free movement of the pipe was prevented. The presence of the side-entry sub (SES) prevented rotation of the pipe and restricted vertical motion even after the logging tools began their descent. A few meters above seafloor, the tool string came to a halt inside the pipe. Bent pipe was indicated by the nature of the set-down and pickup, so the logging tools were pulled back to the surface. Loss of BHA weight was indicated when the drill string was raised as far as the SES configuration would permit. The SES and logging tools then were rigged down so that the vibration-isolated television (VIT) could be deployed.

The VIT was lowered until it showed the end of the drill string at the bottom of the uppermost drill collar, which confirmed that the break was above the seafloor. Review of pipe and BHA records placed the break about 7 m above the seafloor, and a bright spot inside the crater on the sonar presentation appeared to represent the broken BHA. Efforts to view the crater were abandoned because of the low visibility, and the drill pipe was recovered.

Hole 891C

As Hole 891B could not be plugged to isolate it hydraulically from the planned reentry hole at Site 891, plans were altered to place the reentry/CORK installation at proposed Site OM-7. Because important logging objectives of Site 891 had not been fulfilled and because core recovery had been low, preparations were made to drill a dedicated hole for downhole measurements at Site 891 as at Site 888. An additional constraining factor was the planned two-ship oblique seismic experiment that had to be done during the window of opportunity for operations with the *New Horizon.*

A 9⅞-in. tricone drill bit and drilling BHA were assembled and the drill string was run back at an offset location about 40 m south-southeast of Hole 891B. The seafloor was "felt" at 2664 mbsl and the new hole was spudded at 1015 UTC 2 November.

Drilling proceeded smoothly, with precautionary mud sweeps at 200, 300, and 400 mbsf. No excess torque, hole fill, or other indications of unstable hole were noted. At the TD of 492 mbsf, a 50-bbl sweep of viscous mud was circulated through the hole. A wiper trip to 70 mbsf encountered only minor resistance at a few depths and 6 m of fill at TD. After another mud sweep of 50 bbl, the mechanical bit release (MBR) was actuated.

When the MBR had been pulled to 95 mbsf, the logging sheaves were rigged. Before the first logging tool string could be assembled, however, the drill string began sticking. The circulating head was attached and the pipe was "worked" for about half an hour with water circulation before it suddenly came free. A lack of any residual drag suggested that the sticking had been caused by sand/silt cuttings falling into the hole around the BHA. With the pipe completely free at 103 mbsf, logging operations resumed.

The geophysical tool string was stopped by a bridge at 295 mbsf; a good log was recorded up to the pipe from that depth. Because the lower portion of the hole was the primary logging target, the SES was deployed to provide the capability of placing the logging tools deep in the hole. With the quad-combo back inside the pipe, the BHA was run into the hole to open it for the logging tool. First resistance was met when the end of the string reached 231 mbsf; the pipe was firmly stuck when the weight was picked up. The incident seemed identical to that at Hole 888B in which a fall of sand apparently overtook the drill string.

The tool string was removed through the SES. Overpull approaching the tensile-strength limit of the drill pipe then was required to free the pipe. The MBR was pulled to 138 mbsf, where the pipe was free in the hole and the SES was removed from the pipe. The hole was then cleaned to TD with the open-ended BHA. Mud sweeps were used to remove 5 m of fill and to restore the hole to apparently acceptable logging condition. The end of the pipe was pulled back to 333 mbsf for another attempt to access the lower part of the hole.

With the pipe deep in the hole, the geophysical tool string reached a bridge at 431 mbsf (61 m off TD) and a log was recorded for most of the lower hole. The pipe stuck again as the logging tools were changed. Pipe was pulled against moderate drag to 280 mbsf where the top drive was again deployed to clean the hole (7 m of fill remained). The top drive was left attached after the pipe had been pulled to 315 mbsf for the two-ship Oblique Seismic Experiment (OSE).

After establishing a good geophone position in the hole at about 400 mbsf, the OSE was commenced, but after only half an hour an air-compressor failure on *New Horizon* forced interruption of the OSE while the compressor aftercooler was transferred to *JOIDES Resolution* for repairs. Because the Woods Hole Oceanographic Institution downhole hydrophone was already in place, a VSP was conducted using the 300-in.^{3} air gun and 400-in.^{3} water gun suspended over the side of the *Resolution.* Attempts to raise the pipe in the derrick for the upper two VSP stations of this set found the pipe stuck again. The pipe was freed after a few minutes and was then raised 10 m for completion of the VSP.

Formation MicroScanner (FMS) and geochemical logging runs following the VSP were recorded over about 130 m of the lower part of the hole.

With the downhole measurement program complete in the lower hole with the exception of the OSE, the pipe was raised for additional work in the upper hole section. When the MBR had been pulled to 235 mbsf, tension and torque increased until the pipe was stuck fast. After 2 hr of unsuccessfully attempting to free the pipe, the conclusion was drawn that the pipe would have to be severed above the BHA to permit recovery of the drill pipe. With the pipe immobilized, the hole below it was protected from falling debris and the pipe noise level was reduced, producing improved conditions for the OSE. Compressor repairs had been completed and the OSE resumed. The scope of the OSE was limited by the inability to clamp the geophone in large-diameter hole intervals. A full series of measurements were run with the geophones clamped at about 280 mbsf. Further attempts to occupy a geophone position deeper in the hole were thwarted by the formation of a bridge at about 300 mbsf. This problem, and the scheduling constraints on operation time available at Site 891, forced the termination of the OSE after a further 2.5 hr of work.

After the annulus and drill string below the seafloor had been filled with weighted mud, a severing charge was run on the logging line and exploded at 143.5 mbsf in the second joint of drill pipe above the drill collars. The logging line and drill pipe then were recovered, ending operations at Site 891.

LITHOSTRATIGRAPHY

Introduction

Two holes were cored at Site 891. Three APC cores at Hole 891A penetrated sediments to a total depth of 9.5 mbsf. Hole 891B was cored using the XCB and MDCB to 472.3 mbsf. Cores generally showed extremely poor recovery (see master chart, Fig. 60) and intense drilling disturbance.

No major changes occurred in the lithology of the sediments recovered at Site 891 that allow different lithostratigraphic units to be identified. Although various lithologies were identified, their distribution with depth shows no clear pattern. Therefore, a single unit is defined on the basis of the mineralogic and lithologic composition. Lithostratigraphic Unit I consists of clayey silt, silt, and very fine to medium sand, varying in color from dark gray to dark greenish and olive gray, as well as olive black, with sporadic coarse sand, gravel, pebbles, carbonate concretions, mud clasts, wood, and shell fragments. Sedimentary structures, where preserved, show parallel, convolute, and cross lamination. Sediments throughout the unit show weak reaction with HCl, indicating a small percentage of carbonate. Unit I is divided into three subunits on the basis of fabric and sorting (Fig. 5).

Subunit IA (0–198.2 mbsf; Cores 146-891A-1H to -3H and Cores 146-891B-1X to -24X) consists of clayey silt interbedded with silt and fine to medium sand, with faint parallel lamination in the silts and sands. Convolute- and cross-lamination were noted in Cores 146-891B-15X to -20X (118.4–171.6 mbsf). Tilted beds and convoluted deformation were observed in Cores 146-891A-2H and -3H (4.7–9.5 mbsf).

Subunit IB (198.2–383.9 mbsf; Cores 146-891B-25X to -48X) is composed of firm, fractured, unsorted clayey silt with minor amounts of dark gray silt and sand. Sediments of the subunit are less sorted in comparison with the adjacent subunits. Inclined layers (dips of 15°–20°) and broken formation are present. The lower boundary of the subunit is transitional and was identified according to a downhole decrease of fracturing and an improvement in sorting.

Subunit IC (383.9–472.3 mbsf; Cores 146-891B-49X to -58X) includes clayey silt, sandy silt, and fine to medium sand. The sediments are softer than in Subunit IB, show less evidence of drilling disturbance, and demonstrate well preserved planar-, convolute-, and cross-lamination.

Lithostratigraphic Unit I

Subunit IA

Intervals: Hole 891A, Cores 146-891A-1H to -3H; Hole 891B, Cores 146-891B-1X to -24X
Depth: Hole 891A, 0–9.5 mbsf; Hole 891B, 0–198.2 mbsf
Age: Quaternary

Lithostratigraphic Subunit IA consists of dark greenish to olive gray clayey silt interbedded with silt and very fine to medium sand, dark gray to very dark greenish gray in color.

The upper part of Subunit IA (Hole 891A; see Fig. 5) is well represented in Cores 146-891A-1H to -3H (0–9.5 mbsf). Two varieties of silt were identified in Core 146-891A-1H (0–4.7 mbsf). The green silt is enriched in diatoms (up to 15% according to smear slide analysis, see "Petrography" in this section), whereas the gray silt contains carbonate bioclasts and dolomite grains. Beginning with Core 146-891A-2H (4.7 mbsf) firmer clayey silt, mostly dark gray in color, with sand and pebbles (up to 2 cm in diameter), occurs downsection. Sediments observed in Cores 146-891A-2H and -3H (4.7–9.5 mbsf) contain convoluted, folded, and inclined layers and structures (Fig. 6) that might have resulted from slumps and/or debris flows (Fig. 7).

Commonly, the clayey silt contains patches of thin (millimeter-scale) sandy layers, as well as pebbles of basalt, carbonate concretions, and quartzite. Silt and sand in places form faintly laminated beds (Fig. 8). Coarse sand is rare and was observed as dispersed grains in a finer matrix. Randomly distributed gravel grains are composed of chert, claystone, and quartzite (e.g., Core 146-891B-10X; 83.1–92.0 mbsf). Convolute- and cross-lamination were noted through Cores 146-891B-15X to -20X (118.4–171.6 mbsf).

Disseminated pyrite and an enrichment in dolomite (up to 15% according to smear slide analysis) were identified in the silt fraction in Core 146-891B-20X (162.7–171.6 mbsf).

Subunit IB

Intervals: Cores 146-891B-25X to -48X
Depth: 198.2–383.9 mbsf
Age: Quaternary

Lithostratigraphic Subunit IB is composed of firm, fractured, unsorted clayey silt, dark to very dark greenish gray in color with minor amounts of dark gray silt and sand.

The clayey silt is mostly indurated and fragmented into angular pieces up to 5 cm across. Sets of fractures show orientation in two directions with dips at about 45°–47° (Core 146-891B-30X; 237.6–242.4 mbsf), 20°–65° (Core 146-891B-32X; 251.4–260.2 mbsf), 30°–65° (Core 146-891B-33X; 260.2–263.1 mbsf), and 22°–37° (Core 146-891B-35X; 269.0–277.8 mbsf). Silt occurs in thick (up to 1 m) and thin (millimeter-scale) layers, some of which are inclined at 15°–20° (Cores 146-891B-31X [242.4–251.4 mbsf] and -44X [339.3–348.2 mbsf]). Some silt layers contain disseminated sulfides (Core 146-891B-28X [224.7–233.6 mbsf]). Isolated clasts (about 2 cm across) of firm dark greenish gray carbonate-cemented silt were observed in Core 146-891B-29X (233.6–237.6 mbsf). Silt with pebbles (up to 3 cm in diameter) occurs in Cores 146-891B-34X (263.1–269.0 mbsf) and -35X (269.0–277.8 mbsf).

Quartzite, basalt pebbles, mudstone clasts, and carbonate concretions were found randomly distributed in a silty matrix.

Silty sand and very fine to medium sand, which is very poorly sorted and commonly micaceous, occur throughout the subunit as patches or thin (1 to 3 mm) layers. Faint parallel lamination is the most common sedimentary structure. Convolute- and cross-lamination were observed only in Core 146-891B-41X (312.8–321.6 mbsf).

Wood fragments of various sizes and shapes were observed in Cores 146-891B-26X, -37X, -39X, and -41X (from 207.1 to 321.6 mbsf in total; e.g., Fig. 9). Shell fragments were found in Cores 146-891B-34X (263.1–269.0 mbsf) and -37X (278.8–286.4 mbsf).

A zone of broken formation is present in Core 146-891B-33X (260.2–263.1 mbsf), where the sand and silt sediment is disrupted in 0.5- to 1.0-cm-size pieces surrounded by a matrix of black mud (see "Structural Geology" section, this chapter).

The upper boundary of lithostratigraphic Subunit IB is sharp and marks the contrast between the undisturbed sediments above and fractured and poorly sorted sediments below. The location of the upper boundary correlates well with the geochemical and physical properties data (see "Organic Geochemistry," "Inorganic Geochemistry," and "Physical Properties" sections, this chapter). The lower boundary of the subunit is transitional and identified according to a downhole decrease in fracturing and an improvement in sorting.

Subunit IC

Intervals: Cores 146-891B-49X to -58X
Depth: 383.9–472.3 mbsf
Age: Quaternary

Subunit IC includes dark greenish gray to dark gray clayey silt, sandy silt, and fine to medium sand. Fissile sediments occur only from 445.8 to 463.5 mbsf in Cores 146-891B-56X and -57X. Soft sediments below Core 146-891B-57X (463.5 mbsf) show no evidence of drilling disturbance and contain well preserved planar-, convolute-, and cross-lamination. Fragments of wood and carbonate concretions, black sulfides, rare quartzite, and coated pebbles are present throughout the subunit.

Grain Size

Grain-size analysis of 39 samples collected in the finest fraction of the sediments of Hole 891B did not provide additional useful information for the distinction of lithostratigraphic units.

Figure 10 shows that the mean grain size of the finest fraction of the recovered sediments is rather uniform, in the range of fine silt, throughout the hole (we remind the reader that the absolute value of the grain sizes might have to be changed after post-cruise calibration of the analysis with the "pipette" method). We did not observe here the large excursions from very fine silt to medium silt that were correlated with major changes in the sedimentary environment at Site 888 (see "Lithostratigraphy" section, "Site 888" chapter, this volume). Sorting and skewness (Fig. 10) further indicate the extreme homogeneity of the samples. The cumulative histogram of grain-size classes (Fig. 11) suggests that the main variations in grain size occur within the silt range, and in particular among very fine (4–8 μm), fine (8–16 μm), and medium (16–31 μm) silt. Nevertheless, no clear trends can be identified in these changes.

Some indications of downhole trends are provided by the histogram of the recovery of each lithology identified in each core through visual description and smear slide analysis (Fig. 12). The distribution of clayey silt (Fig. 12) indicates four peaks in Cores 146-891B-14X (109.5–118.4 mbsf), -31X (242.4–251.4 mbsf), -43X (330.4–339.3 mbsf), and -55X (437.0–445.8 mbsf). The distribution of the poorly sorted lithologies (sand-silt-clay and clayey sand) shows a broad maximum between Cores 146-891B-34X and -41X (interval from 263.1 to 321.6 mbsf; Fig. 12). The distribution of the coarser sorted

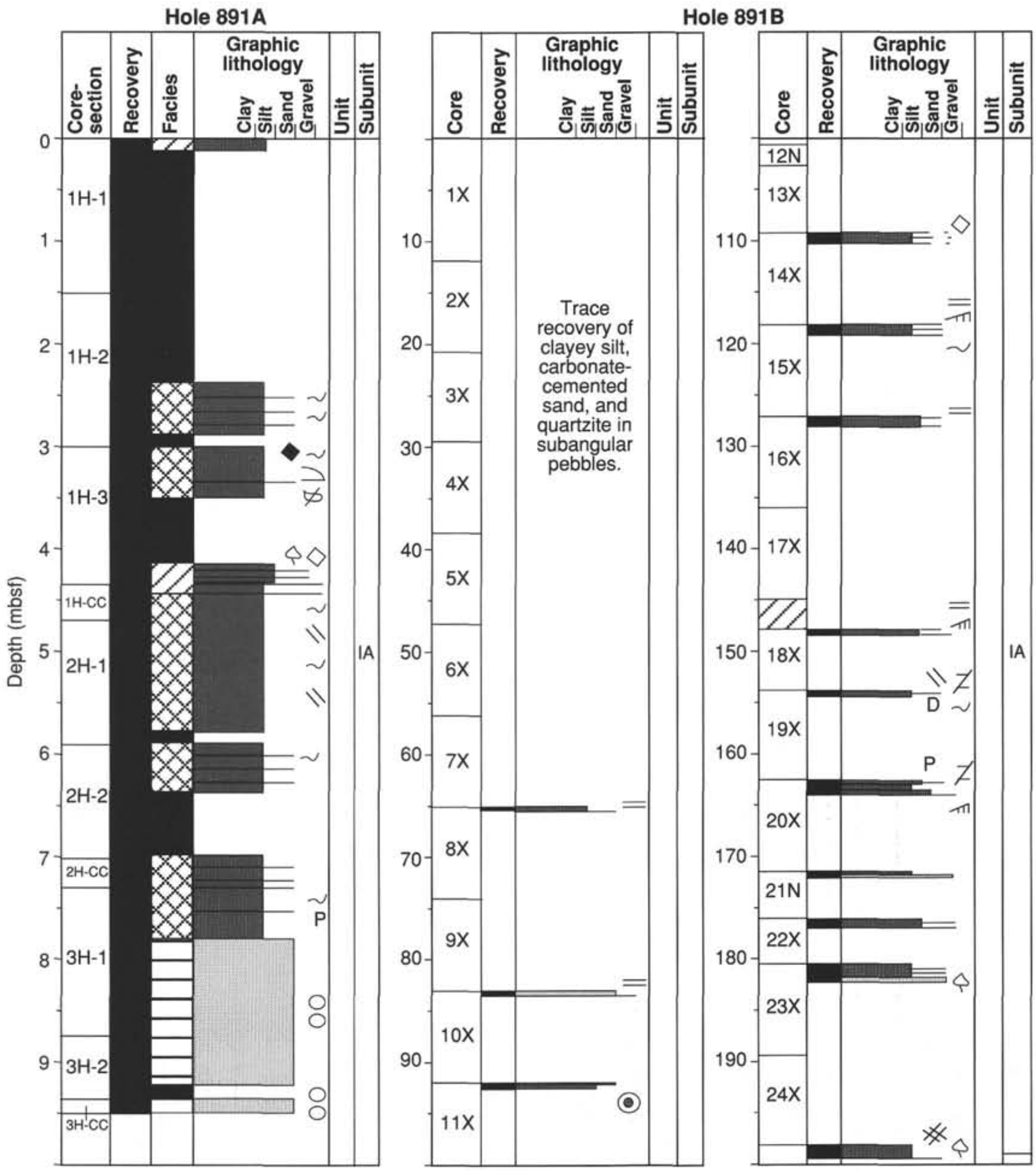

Figure 5. Sediment column and facies type for Holes 891A and 891B (facies interpretation according to table 2 in "Lithostratigraphy" section, "Site 888" chapter, this volume).

material (silt, sand, and silty sand) shows peaks in Cores 146-891B-23X (180.5–189.4 mbsf) and -58X (463.5–472.3 mbsf) (Fig. 12). This distribution of lithologies supports the transition from Subunit IA to IB between Cores 146-891B-24X and -25X at the depth of 198.2 mbsf as a sharp decrease of the coarse, sorted sediment and a gradual increase of the poorly sorted lithologies.

The changes in degree of sorting outlined by visual description and smear slide analysis are not reflected in the grain size of the fine fraction (Fig. 12). The poor sorting results from the presence of a coarse fraction that was not sampled for shipboard grain-size analysis. Representative coarse-grained samples have been collected for post-cruise studies.

Sediment Petrography

The composition of sediments in Hole 891 was estimated visually from smear slides and grain mounts. There are no systematic changes in any of the components with depth, although there are marked changes in composition with grain size. No further subdivision of the single lithostratigraphic unit defined at Site 891 is possible on the basis of the sediment composition.

Coarse Silts and Sands

The sands and coarse silts in Hole 891B rarely preserved any sedimentary structures. Commonly a high proportion of clay is mixed with the coarser sediment. It is possible that some of these mixed sediments were produced by drilling disturbance. These apparently disturbed parts of the cores were avoided when sampling for smear slides. Even so, the sediments were generally found to be poorly sorted, and relatively few layers consisting solely of sand or silt were sampled. The composition of the smear slides was found to depend strongly on the degree of grain-size sorting: certain mineral and rock

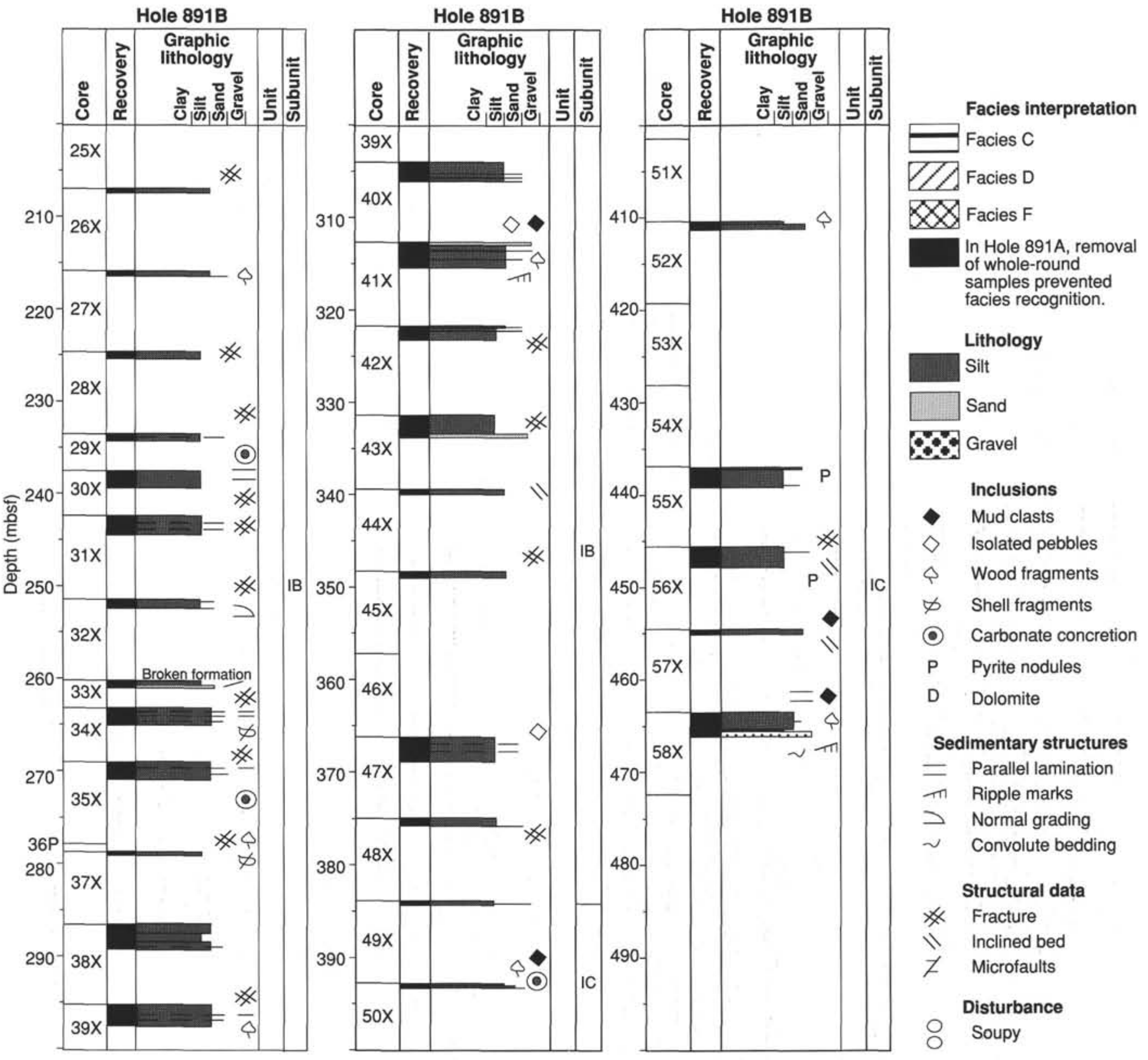

Figure 5 (continued).

grains, particularly heavy minerals and opaque minerals, were concentrated in a particular size range.

Quartz

Quartz occurs in amounts up to 40% in the smear slides of coarse silts and sands. It is generally angular and unstrained, but rounded, polycrystalline strained quartz and quartz with numerous fluid inclusions were also found in small quantities.

Feldspars

Feldspars were found in amounts ranging from 10% to 25% in the smear slides of coarse silts and sands. Plagioclase is the dominant mineral, showing some twin sets from which an oligoclase to andesine composition was determined. More commonly the plagioclase is cloudy and zoned, with poorly discernable twinning. Microcline is conspicuous in a number of samples. Perthite is present in at least four samples. Other potassium feldspars are present in small quantities in most of the sands and silts, as confirmed by X-ray diffraction (XRD; see "Fine Silts and Clayey Silts" section, below).

Lithic Fragments

Lithic fragments comprise up to 30% of the coarser sands in Hole 891. More generally, 10%–20% lithic fragments were found in smear slides of the silts and fine sands. Almost all lithic fragments are fine-grained igneous rocks of basic to intermediate composition. Some chert fragments and very rare schist fragments were also found.

Micas

Micas are present throughout the coarse silts and sands. The quantity of micas in the smear slides ranges from 2% to 12%. White, green, and brown micas were found together.

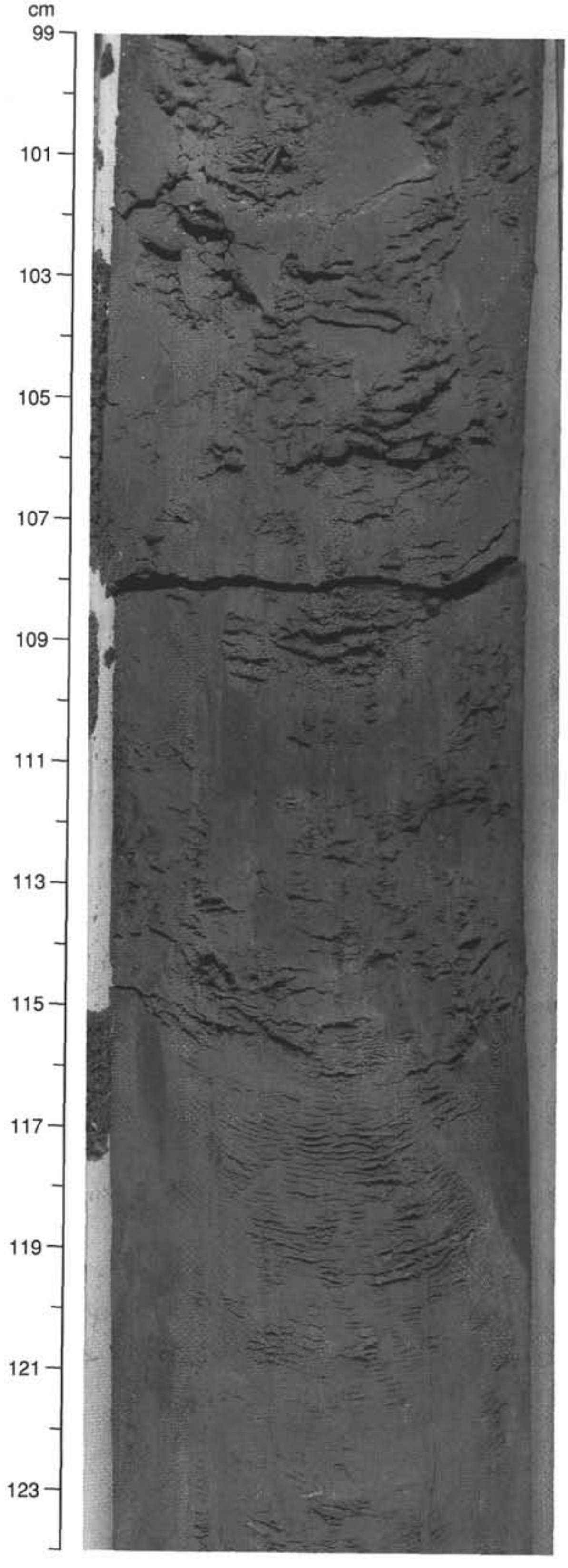

Figure 6. Tilted bedding planes in sediments of Section 146-891A-1H-2, 99–124 cm.

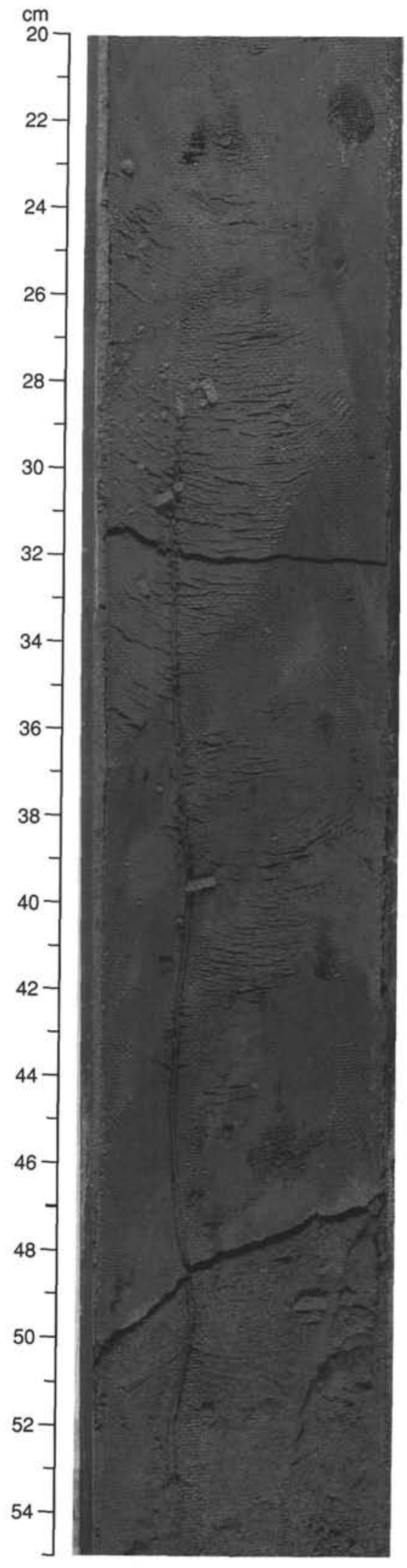

Figure 7. Debris-flow deposits in Section 146-891A-3H-1, 20–55 cm.

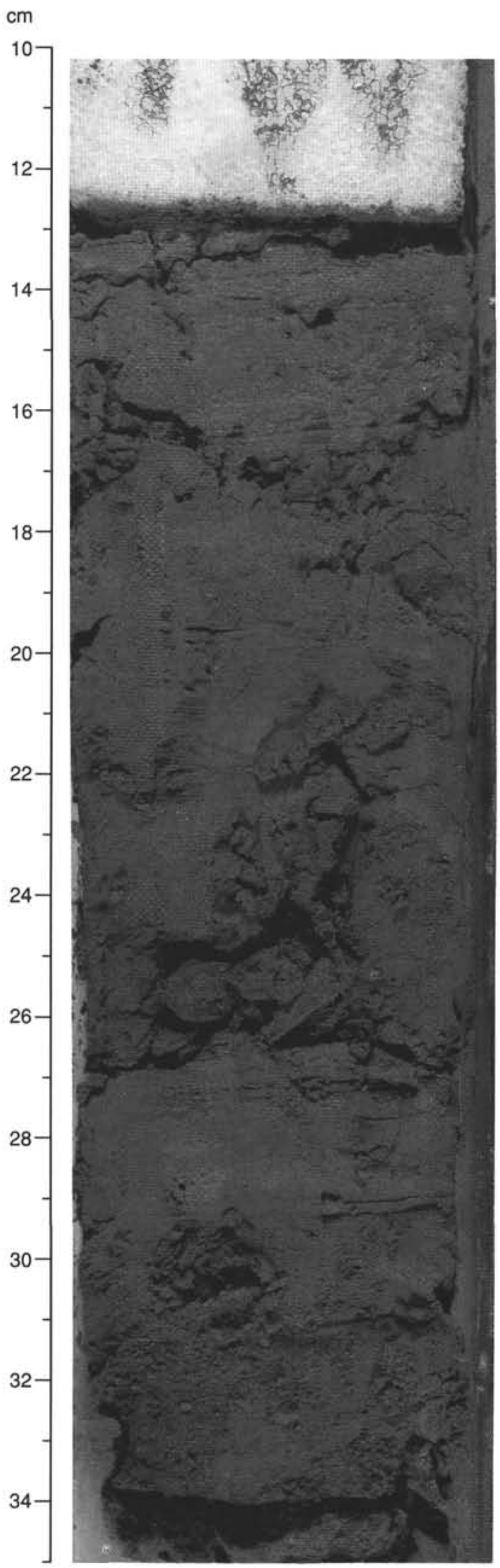

Figure 8. Fine horizontal lamination in Section 146-891B-8X-1, 10–35 cm.

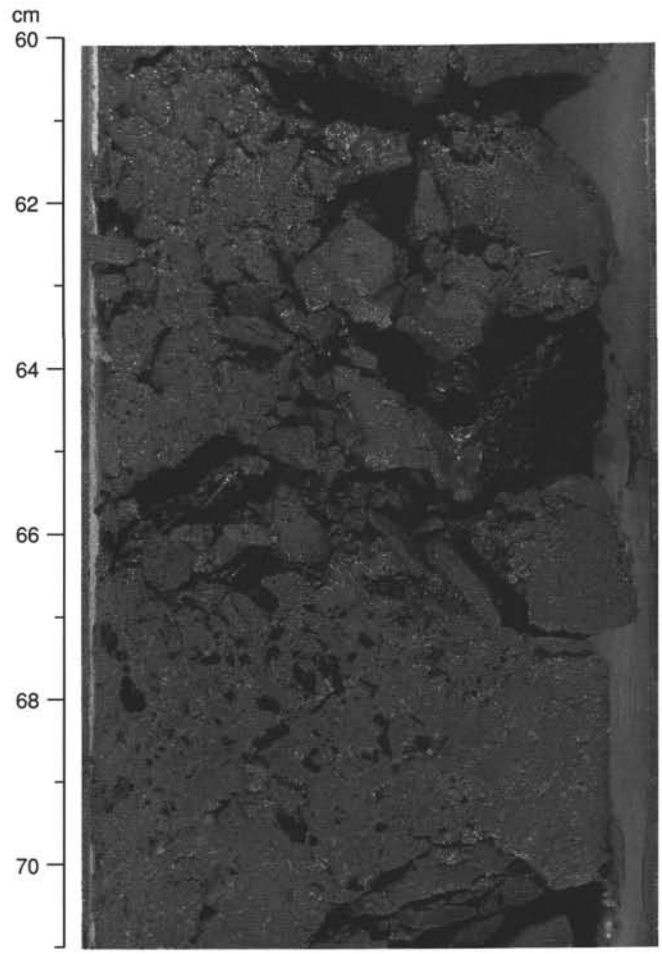

Figure 9. Wood fragments in silt of Section 146-891B-39X-1, 60–71 cm.

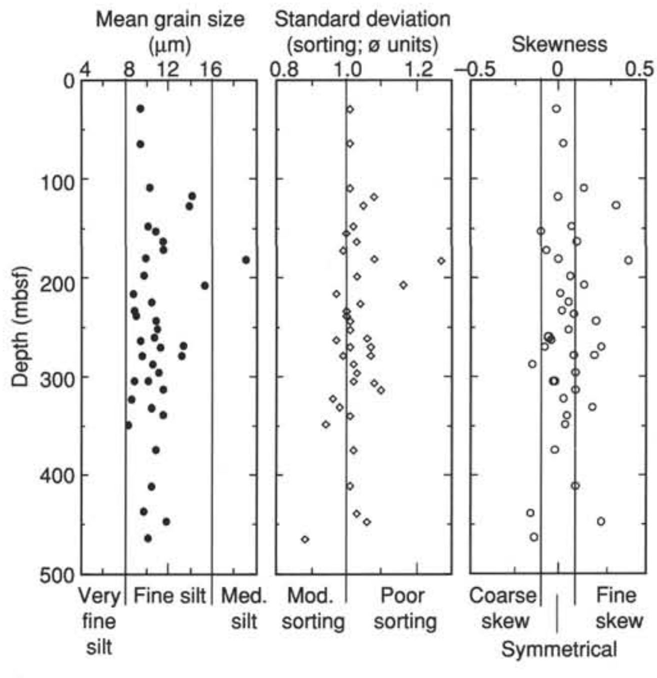

Figure 10. Results of shipboard grain-size analysis on the fine fraction of the sediment. Mean grain size, sorting, and skewness do not indicate major changes with depth in Hole 891B. Med. = medium, and Mod. = moderate.

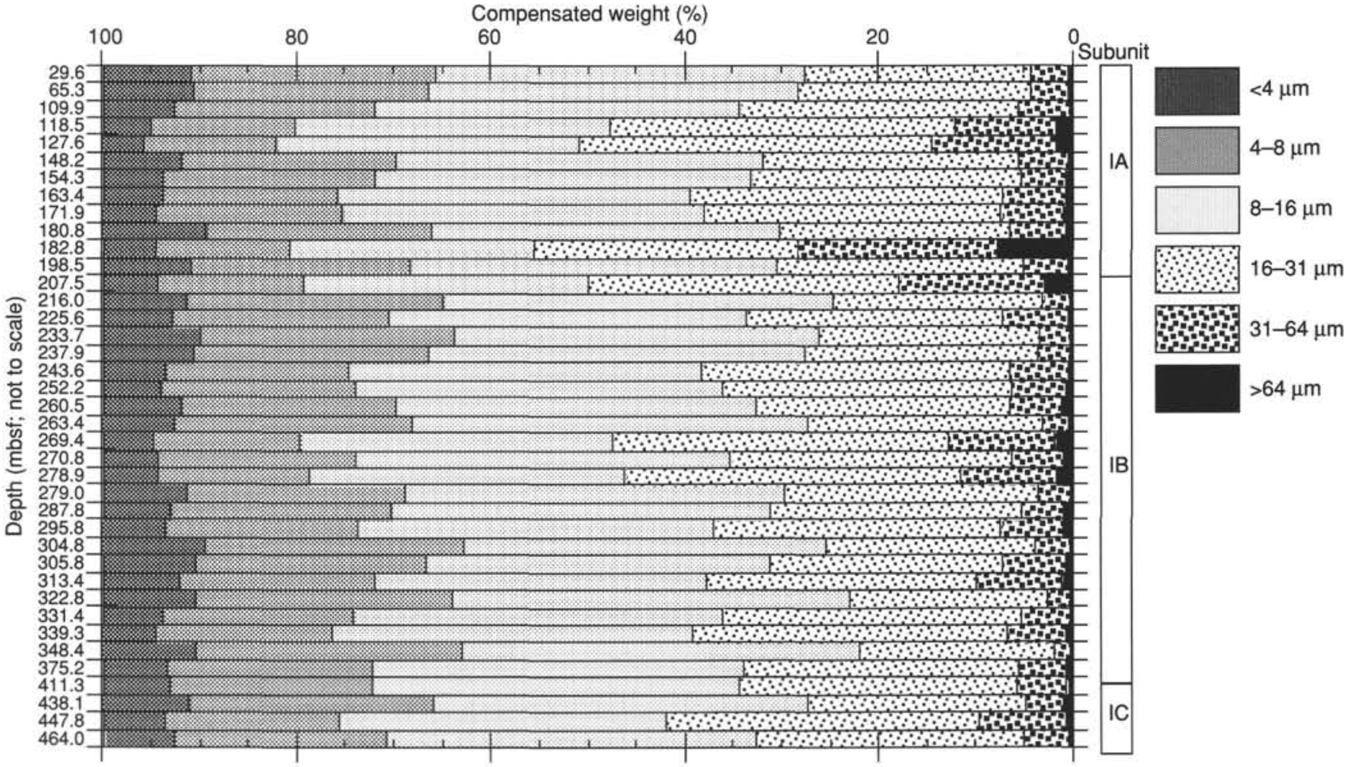

Figure 11. Cumulative histogram of the fine fraction of grain-size classes identified in Hole 891B. The main variations in grain size occur within the silt range, and in particular among very fine (4–8 µm), fine (8–16 µm), and medium silt (16–31 µm).

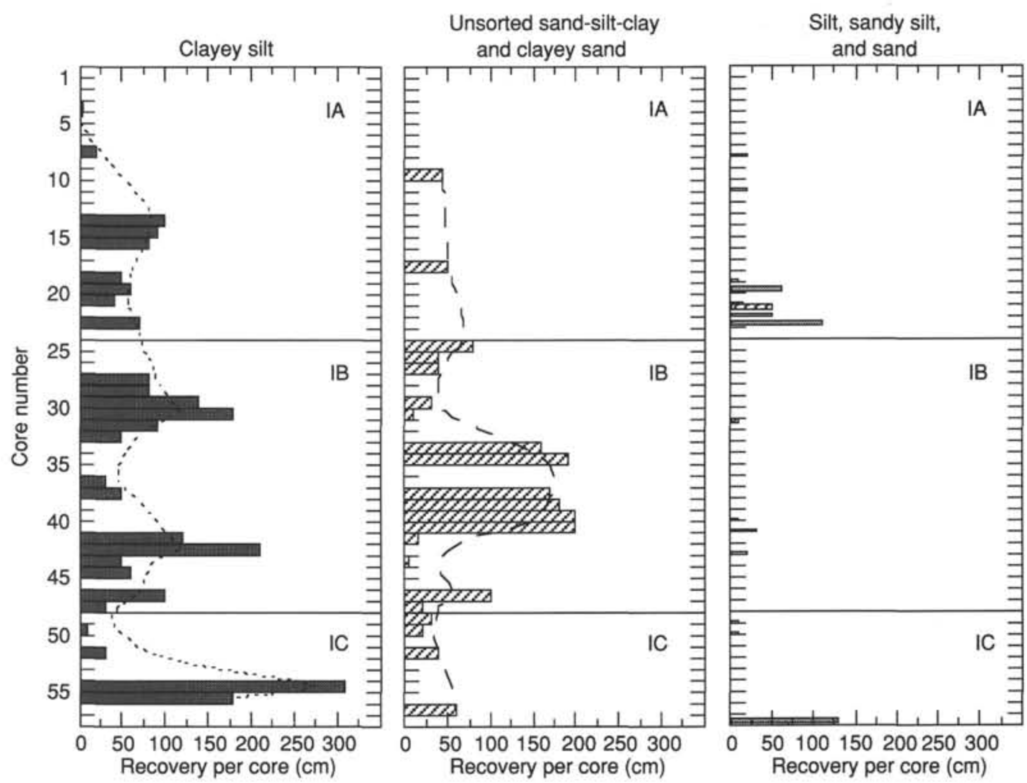

Figure 12. Histograms of the recovery of the lithologies (clayey silt, unsorted coarser sediment, and sorted coarser sediment) identified in each core through visual description and smear slide analysis supporting the distinction between Subunits IA, IB, and IC.

Volcanic Glass

Volcanic glass is a common constituent of the coarse silts and sands. Pale green, dark green, and almost colorless varieties occur. Glass is most abundant in the more micaceous silts and fine-grained sands.

Accessory Minerals

Accessory minerals in the coarse silts and sands include, most abundantly, amphiboles and pyroxenes. Hornblende, with subdued green and brown pleochroism, and a probable ferroactinolite, with a dark green body color, are the most common amphiboles, forming 2%–10% of the sediment. Pale green clinopyroxene and colorless orthopyroxene are present in quantities of up to 5% in well-sorted sands. Less well-sorted sands and silts typically contain 1%–2% of these two phases. Garnet (as colorless, pale green, or pink varieties) is present in amounts up to 4%, notably in Cores 146-891B-14X (109.5–118.4 mbsf), -31X and -32X (242.4–260.2 mbsf), -39X through -41X (295.1–321.6 mbsf), -52X (410.5–419.3 mbsf), and -56X (445.8–454.7 mbsf). Other accessory minerals were rarely found in quantities greater than 1%. Epidote is relatively common in some lithic sands (e.g., Samples 146-891B-34X-1, 38 cm; -35X-CC, 14 cm; and -50X-1, 44 cm). Apatite, zircon, rutile, and tourmaline are almost ubiquitous in trace amounts. Topaz was found in conspicuous quantities in Samples 146-891B-55X-2, 102 cm, and -55X-3, 53 cm. Glaucony is present in trace amounts in Core 146-891A-2H (4.7–7.3 mbsf) and below 65.2 mbsf in Hole 891B (Cores 146-891B-8X to -16X, and Cores 146-891B-21N, -34X, -56X, and -58X); amounts of up to 1%–5% are estimated. The glaucony grains are dark, rounded, and abraded, and appear to be detrital in origin.

Opaque Minerals

Opaque minerals were found in sediments throughout Holes 891A and 891B; 1%–5% is common. The opaque mineral grains are rarely well shaped, but in some cases euhedral magnetite could be distinguished. Sulfides are common as cubes or framboids. Sulfides account for more than half of the opaque grains counted in the smear slides. Sulfides are most abundant in samples with high concentrations of wood fragments (e.g., Sample 146-891B-32X-1, 31 cm).

Biogenic Skeletal Material

Biogenic skeletal material is rare in the sediments of Hole 891B. Foraminifers are usually absent or were found only in trace amounts. In Sample 146-891B-29X-1, 51 cm, 5% foraminifers was estimated. These are broken and abraded and may be a reworked concentrate. Biogenic silica is generally absent from the sediments, or occurs only in trace quantities. In two intervals, however (278.8–304.0 and 437.0–445.8 mbsf; Cores 146-891B-37X through -39X and Core 146-891B-55X, respectively), 5%–15% biogenic silica (mainly diatoms) is present. The diatoms in these intervals were found mainly in dark greenish gray clays and clayey silts, which may represent intervals of high productivity or slow sedimentation rate.

Carbonate

Carbonate, in the form of small rhombs and irregular grains, is present in almost all samples of coarse silt and sand throughout Hole 891B, typically in amounts from 2% to 10%. These visual estimates agree well with chemical analyses of inorganic carbonate (see "Inorganic Geochemistry" section, this chapter). The XRD studies reveal that most of the carbonate present is dolomite (see the following).

Fine Silts and Clayey Silts

Fine-grained sediments were examined in smear slides and by XRD. Most of the fine sediments are clayey silts; intervals with a predominance of clay are rare. The fine-silt fraction is broadly similar in composition to the coarser silts and sands described previously, but with rather more quartz, less feldspar, and fewer lithic fragments.

The quartz and feldspars produce the most intense peaks in the diffractograms. Low quartz and plagioclase feldspar, along with lesser quantities of potassium feldspar, were recognized in all samples. A trace amount of amphiboles is also ubiquitous. Sample 146-891B-47X-1, 36–37 cm, shows an intense peak at 8.35Å, which may be caused by either amphibole or a zeolite mineral.

Clay minerals are present in all the samples analyzed, but in samples from the first seven cores in Hole 891B they are present only in trace amounts, reflecting the relatively coarse grain size of the material recovered. The clay minerals present below this depth are illite/micas, chlorite and kaolinite, and mixed-layer clays (probably of the illite/smectite series). Both the micas and the chlorites produce sharp peaks, and they are thought to be of detrital rather than authigenic origin (Fig. 13). The ratio of chlorite to micas is variable in different samples, but shows no systematic change with depth. It is probable that the change in ratio is at least partly related to the grain size of the sediment analyzed: more mica, and less chlorite are present in coarser grained samples.

The ratio of kaolinite to chlorite is also variable; rather more kaolinite is present in the samples from greater depth than in samples from the upper part of Unit I. The kaolinite peak is typically 30%–60% of the height of the chlorite peak, which suggests that markedly less kaolinite than chlorite is present.

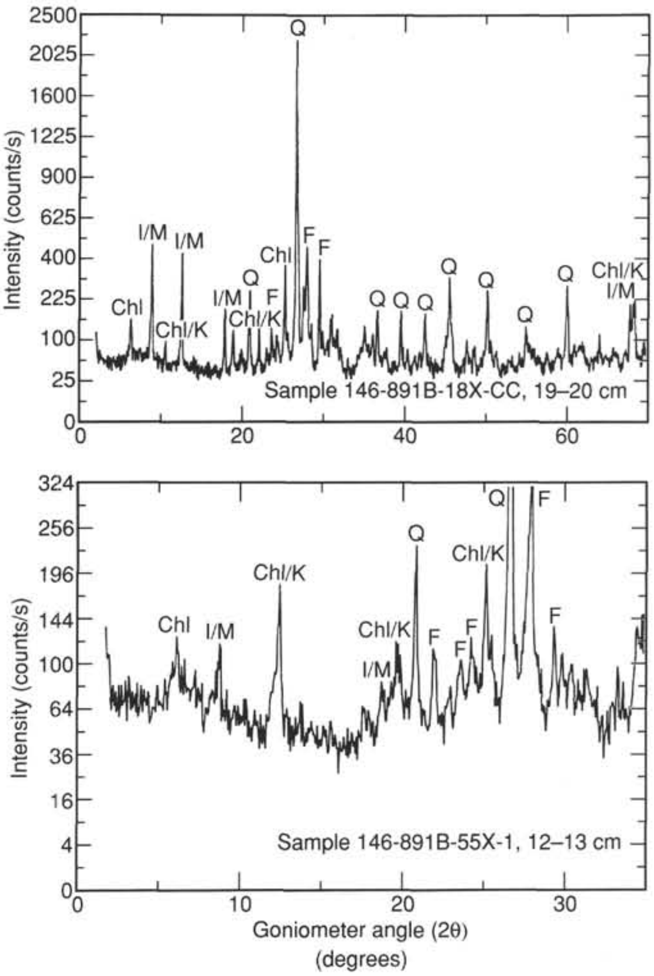

Figure 13. Results from XRD measurement of two samples from Hole 891B. Q = quartz, Chl = chlorite, K = kaolinite, I/M = illite/micas, and F = feldspar.

Mixed-layer clays are detected as a higher background of irregular peaks in the 17–10 Å region (Fig. 13). They are a minor constituent of all samples. There is a possible increase in the amount of mixed-layer clays with depth in Hole 891B, but this trend is largely lost when corrections are made for grain size.

SEDIMENTARY ENVIRONMENT

Because the sediments recovered at Site 891 account for <11% of the total sedimentary sequence, unequivocal identification of the environment of deposition is impossible. However, general considerations and observations on cores provide useful information.

General Considerations

1. Site 891 is located on the lower slope of the Oregon margin, at the mouth of a deep-sea canyon cut by erosion of the first ridge of the slope (see "Background and Objectives" and "Seismic Stratigraphy" sections, this chapter). The site is elevated 150 m above the abyssal plain.
2. Site 891 cored the upper, faulted portion of a 3-km-thick, layered seismic sequence (see "Seismic Stratigraphy" section, this chapter). Because the cored interval falls within the Brunhes Chron (see "Paleomagnetism" section, this chapter) and no tectonic thickening has occurred in the section above the fault zone at 263 mbsf (see "Structural Geology" section, this chapter), the accumulation rate at Site 891 is on the order of 100 m/m.y. The presence of sand in the sediment section is required to explain such a high accumulation rate.
3. Site 891 appears to be located on an erosional surface (see "Seismic Stratigraphy" section, this chapter). The shear strength of the surface sediments cored in Hole 891A indicates some overconsolidation (see "Physical Properties" section, this chapter), possibly produced by a burial depth estimated as 300 m (see "Seismic Stratigraphy" section, this chapter).

It follows that the sediments cored at Site 891 were not deposited in the present-day lower slope physiographic setting.

Observations on Cores

1. Sediments cored in Hole 891B are represented by clayey silt, silt, and sand, which are mostly poorly sorted. Massive sand was recovered only in Cores 146-891A-3H (7.8–9.5 mbsf) and 146-891B-11X (92.0–92.1 mbsf). The latter core was made up of material recovered on the outer surface of the WSTP.
2. The sedimentary structures observed are parallel-, cross-, and convolute lamination that suggest the presence of Bouma sequence T_{cde} (Bouma, 1962). The thickness of the laminated sequences rarely exceeds 1 m. These structures originate by turbidity current deposition.
3. In terms of the classification proposed by Mutti and Ricci Lucchi (1972), the observed sediments represent Facies C and D (see Table 2, "Site 888" chapter, this volume).

It is possible that significant amounts of poorly sorted sediment were not recovered. Logging results, particularly gamma-ray values, suggest a wide distribution of grain size (see "Downhole Logging" section, this chapter). Facies C and D alone indicate a turbidite depositional environment on outer deep-sea fans (outer fan subassociation 2D; see table 2, "Site 888" chapter, this volume). However, the association of these facies with coarser material suggested by gamma-ray and caliper data (see "Downhole Logging" section, this chapter) and the aforementioned general considerations may also indicate either a middle fan or inner fan environment of deposition.

Sediments in the uppermost portion of the unit (Cores 146-891A-2H to -3H [4.7–9.5 mbsf]) contain convoluted, folded, and inclined layers and structures that are indicative of slump and/or debris-flow processes. The dominance of clayey silt in these sediments indicates a slope depositional environment, where mass movement of uncon-

Table 2. Distribution of planktonic foraminifers in core-catcher samples from Site 891, including coiling, zonation, and surface water paleotemperature.

Core, section	Depth (mbsf)	Abundance	Preservation	*Globigerina bulloides*	*Globigerina quinqueloba*	*Globigerina umbilicata*	*Globigerinita glutinata*	*Globigerinita uvula*	*Globorotalia crassula*	*Globorotalia hirsuta*	*Globorotalia scitula*	*Neogloboquadrina dutertrei*	*Neogloboquadrina pachyderma* (d)	*Neogloboquadrina pachyderma* (s)	*Orbulina universa*	Planktonic spp.	Paleotemperature	Coiling dominance zone	Epoch
146-891A-																			
1H-CC	4.7	C	G	F		R	R						R	F			Cool	CD1 to CD8	late Quaternary
2H-CC	7.3	A	G/M	F	C		R	R			R		F	A					
3H-CC	9.5	R	M	R										R					
146-891B-																			
1X-CC	0	C	G	C	R		R	R			R		F	C					
2X-CC	12.0	A	G	C	F	R					R	R	F	C	R		- - -		
3X-CC	20.8	F	G	R	R		R							R			Cold surface waters		
4X-CC	29.7	C	M	F	R						R	R	R	F					
6X-CC	47.3	F	G	F			R						R	F					
7X-CC	56.2	C	G	F	F		R		R		R	R	R	F					
8X-CC	65.6	R	M	R	R									R					
10X-CC	83.6	R	G	R										R					
11X-CC	92.5	B																	
14X-CC	110.5	C	G	C	R	R							R	F					
15X-CC	119.5	R	G	R															
16X-CC	128.2	B																	
18X-CC	148.7	R	G	R															
19X-CC	154.6	F	G	F	R		R							R					
20X-CC	164.6	R	G													R			
21N-CC	172.2	F	G	F	R								R	F					
22X-CC	177.1	B																	
23X-CC	182.8	F	G	R	R		R						R	F					
25X-CC	199.3	F	G	R										F					
26X-CC	207.6	R	G											R					
27X-CC	216.5	R	G											R					
28X-CC	225.7	R	G											R					
29X-CC	234.5	R	G											R					
30X-CC	239.6	R	G											R					
31X-CC	244.5	R	G	R									R	R					
32X-CC	252.4	C	G	F			R						R	F					
33X-CC	261.0	F	G	R	R		R						R	F					
34X-CC	265.0	F	G	R									R	F					
35X-CC	270.9	F	G										R	F					
37X-CC	279.1	C	G	F	R		R						R	F					
38X-CC	289.9	C	M	F	F					R	F		F	C	R				
39X-CC	297.4	F	G	F	F								R	F					
40X-CC	306.1	C	G	F	F								R	C					
41X-CC	315.6	C	G	F										C					
42X-CC	323.1	R	G											R					
43X-CC	332.8	R	G											R					
44X-CC	339.8	B																	
45X-CC	348.9	F	G	R										F					
47X-CC	368.6	F	G	R	R								R	F					
48X-CC	375.8	C	M	F			R						R	F					
49X-CC	384.3	R	G											R					
50X-CC	393.3	B																	
52X-CC	411.6	R	M	R										R					
55X-CC	440.1	C	G	F	R		R						R	C					
56X-CC	447.9	F	G	R										F					
57X-CC	455.3	A	G	C	F		F						R	A					
58X-CC	465.9	C	G	F	F	R	F						R	F					

Notes: Dextral (d) and sinistral (s) *N. pachyderma* are listed separately. A = abundant, C = common, F = few, R = rare, G = good preservation, M = moderate preservation. See "Explanatory Notes" chapter, this volume, for an explanation of the categories.

solidated sediments is common. Most probably the observed sediments represent Facies F formation (Fig. 5).

The sediments recovered at Site 891 seem to indicate deep-sea fan deposits uplifted and accreted to the lower slope of the Oregon Margin.

Results from Deep Sea Drilling Project (DSDP) Leg 18 indicate that high-accumulation-rate (370–940 m/m.y.), sand-rich sediments (Site 174, Unit 1; Kulm, Von Huene, et al., 1973) were deposited in the abyssal plain following the development of the Astoria Fan during the Pleistocene (1.0–1.2 to 0.8 Ma; Kent et al., 1971). Pliocene to Pleistocene abyssal plain silts, which accumulated at lower rates (140–220 m/m.y.) before the onset of deep sea fan sedimentation, were recovered at Sites 174 and 175. Given the Brunhes Chron age (<0.780 Ma) for all of Hole 891B, the sedimentary section cored at Site 891 can be correlated to the Astoria Fan sedimentary sequence cored at DSDP Site 174.

BIOSTRATIGRAPHY

The sediments recovered at Site 891 afford poor biostratigraphic control throughout most of the sequence. Factors contributing to the uncertainty in age determinations include (1) the occurrence of several intervals barren of microfossils, (2) poor sedimentary recovery, and (3) the absence of zonal markers.

Planktonic and benthic foraminifers are the most persistent of the recovered fossil groups, enabling recognition of the late Pleistocene down to the bottom of Holes 891A and 891B. Radiolarians and diatoms are present in only a few intervals and they are in low abundance.

Planktonic Foraminifers

Moderately to well-preserved upper Quaternary planktonic foraminifers are rare to abundant in Holes 891A and 891B (Table 2). Four out of 50 core-catcher samples examined for planktonic foraminifers are barren. The planktonic foraminiferal assemblages consist mainly of *Globigerina bulloides, Neogloboquadrina pachyderma* (sinistral and dextral), and *Globigerina quinqueloba* with rare to few specimens of the other taxa listed in Table 2. This assemblage suggests cool to cold surface waters.

Age determinations from the planktonic foraminifers are tentatively based on the coiling dominance of *N. pachyderma,* but are not well constrained because no evolutionary marker was found. Rare to common *N. pachyderma* (sinistral) occur throughout Holes 891A and 891B. Mixed populations containing few dextrally and common sinistrally coiled *N. pachyderma* occur in Samples 146-891A-2H-CC (7.3 mbsf), 146-891B-1X-CC (0 mbsf), 146-891B-2X-CC (12.0 mbsf), and 146-891B-38X-CC (289.5 mbsf). The age of this interval is considered to be within the CD1–CD8 coiling zones (see "Explanatory Notes" chapter, this volume, and Lagoe and Thompson, 1988), based on the dominance of sinistrally coiled *N. pachyderma,* the occurrence of mixed coiling intervals, and the normal paleomagnetic signature (see "Paleomagnetism" section, this chapter).

Benthic Foraminifers

Moderately to well-preserved benthic foraminifers are present in 24 of the 50 core-catcher samples from Hole 891B. Two intervals (4.7–56.2 and 440.1–455.3 mbsf) contain abundant to common benthic foraminifers. Samples in the interval from 172.2 to 393.3 mbsf are either barren of benthic foraminifers or contain rare to common specimens. Core-catcher samples in the interval from 65.6 to 164.4 mbsf are barren of benthic foraminifers.

The common to abundant benthic foraminiferal assemblages include *Cibicidoides wuellerstorfi, Melonis pompilioides, Pullenia bulloides, Sphaeroidina bulloides,* and *Uvigerina senticosa,* which are all indicative of deposition in a lower bathyal environment. Rare neritic through middle bathyal taxa occur in several samples throughout Hole 891B and indicate some component of downslope transport from shallower depths. A preliminary list of benthic foraminifers identified from Site 891 is given in Table 3.

Table 3. Preliminary list of benthic foraminifers recovered at Site 891.

Bolivina spp.
Buccella frigida
Bulimina spp.
Bulimina striata
Bulimina subacuminata
Buliminella exilis
Cassidulina californica
Cassidulina spp.
Cassidulinoides bradyi
Cibicides spp.
Cibicides mckannai
Cibicidoides spp.
Cibicidoides wuellerstorfi
Eggerella bradyi
Elphidiella hannai
Elphidium excavatum clavatum
Elphidium spp.
Epistominella pacifica
Eponides healdi
Fissurina lucida
Globobulimina auriculata
Globobulimina pacifica
Globobulimina spp.
Gyroidina multilocula
Gyroidina soldanii
Hoeglundina elegans
Lagena spp.
Martinotiella sp.
Melonis barleeanum
Melonis pompilioides
Nonionellina labradorica
Pullenia bulloides
Pullenia salisburyi
Pyrgo spp.
Quinqueloculina spp.
Reophax sp.
Saccammina sphaerica
Sphaeroidina bulloides
Uvigerina hispida
Uvigerina peregrina
Uvigerina senticosa
Valvulineria araucana

Radiolarians

All core-catcher samples from Holes 891A and 891B were processed and examined for radiolarians. Rare to common and well-preserved radiolarians characteristic of the late Quaternary were found in sediments near the top of the sequence from Hole 891A (Samples 146-891A-1H-CC to -3H-CC [0–9.5 mbsf]). Radiolarian species indicative of upwelling environments (*Lamprocyrtis nigriniae* and *Phormostichoartus crustula*) were found in Sample 146-891A-2H-CC at 7.3 mbsf.

Only rare radiolarian debris was found in the upper part of Hole 891B (Samples 146-891A-1X-CC to -10X-CC [0–83.6 mbsf]), except in Sample 146-891B-7X-CC (56.2 mbsf), where two stratigraphic and/or upwelling markers (*L. nigriniae* and *Pterocanium auritum*) indicate a Pleistocene age. Samples 146-891B-10X-CC to -31X-CC (83.6–244.5 mbsf) are barren of radiolarians.

Radiolarians were very rare to rare in Samples 146-891B-32X-CC to -40X-CC (252.4–306.1 mbsf). No stratigraphic or paleoenvironmental marker was observed. The species composition of these scarce assemblages could be indicative of a Pleistocene age.

Samples 146-891B-42X-CC to -52X-CC (323.1–411.6 mbsf) are barren of radiolarians. Radiolarians occur very rarely to rarely in the interval between Samples 146-891B-55X-CC and -57X-CC (440.1–455.3 mbsf). The occurrence of *Cycladophora davisiana* in Sample 146-891B-57X-CC (455.3 mbsf) indicates a Pliocene-Pleistocene age. Sample 146-891B-58X-CC (465.9 mbsf) is barren of radiolarians.

PALEOMAGNETISM

Paleomagnetic measurements of discrete samples from Holes 891A and 891B were performed to constrain the ages of the sediment at this site. One or two discrete samples were taken from all intact

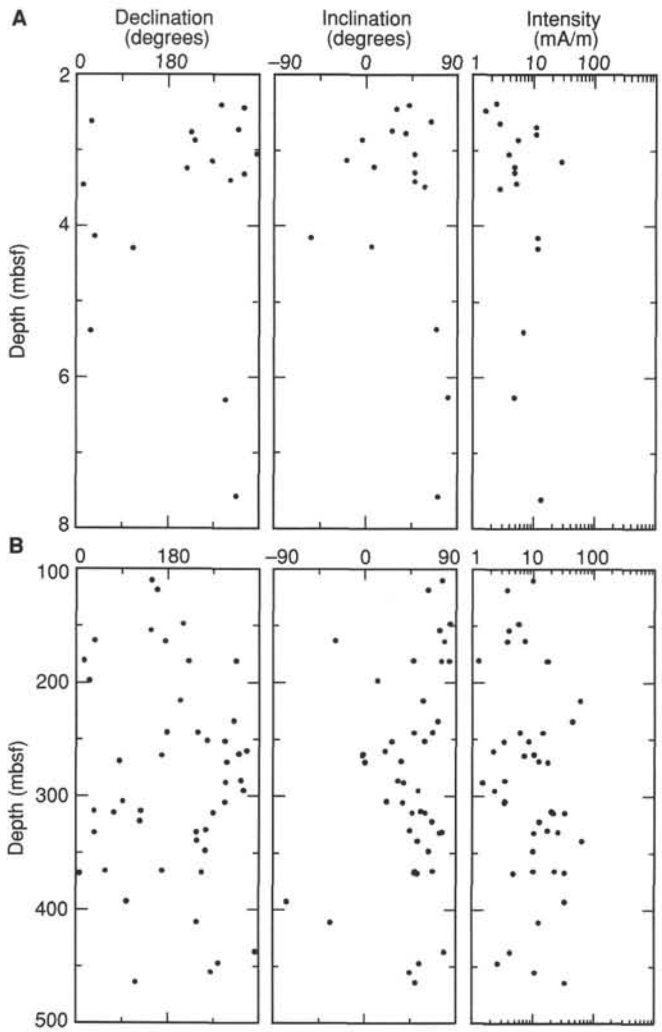

Figure 14. Declination, inclination, and intensity plots for Holes 891A (**A**) and 891B (**B**).

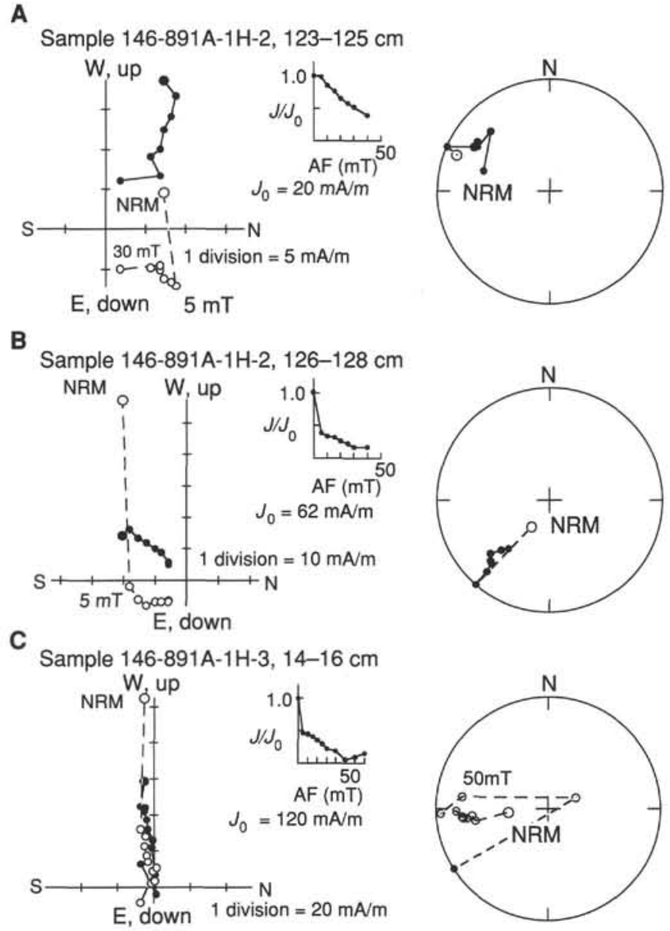

Figure 15. Demagnetization plots of three samples from Hole 891A. Solid symbols on the Zijderveld plots are projections on the horizontal plane, open symbols projections on the vertical plane. Solid symbols on the stereonet plots are lower hemisphere, open symbols upper hemisphere. **A.** Behavior of a sample taken from just above the lower boundary of an 8-cm-wide inclined bed in the interval 146-891A-1H-2, 115–123 cm. **B.** Behavior of a sample from just below the upper boundary of the inclined bed. **C.** An example of demagnetization behavior for reversely magnetized samples observed in Core 146-891A-1H.

sections of both holes. Split-core measurements were also performed for all sections of Hole 891A and Hole 891B. Comparison of demagnetized intensities after alternating-field (AF) demagnetization using the in-line AF coils in the 2G magnetometer, and those demagnetized with the Schonstedt GSD-1, revealed that the maximum demagnetizing peak field produced by the AF coils in the 2G magnetometer was less than 5 mT (as opposed to the nominal value of 24 mT). We therefore have used only the results obtained by AF demagnetization on the GSD-1 in our analysis. An examination of the remanence isolated using higher alternating fields was conducted with one or two discrete samples from each intact core. The samples were demagnetized up to 40–90 mT using steps of 5 or 10 mT. Isothermal remanent magnetization (IRM) acquisition experiments were conducted to examine the relationship between the magnetic coercivity spectrum and the demagnetization behavior of the samples. Automated susceptibility measurements were made at 5-cm intervals on whole cores for all of the cores in conjunction with other measurements made on the multisensor track (MST).

Paleomagnetism

Measurements of the remanence of discrete samples after 30-mT AF demagnetization are shown in Figure 14 for both holes of Site 891. In Hole 891B, remanence with a steeply inclined downward (normal polarity) direction was observed throughout the hole. Three samples in Core 146-891A-1H display directions shallowly inclined upward (reversed polarity). This interval (<4.7 mbsf) in Hole 891A is interpreted as representing slumps and/or debris flows (see "Lithostratigraphy" section, this chapter). Figure 15 shows the results of AF demagnetization for three samples. Figure 15A shows a sample from just above the lower boundary of a steeply inclined layer with a width of 8 cm in Section 146-891A-1H-2, 115–123 cm, and Figure 15B shows a sample from the uppermost part of the inclined layer. Both samples show shallow-down inclinations after removal of a steep-upward drilling overprint. Demagnetization behavior for the three reversed polarity samples from Core 146-891A-1H showed stable decreasing remanence (Fig. 15C). There may be three possible interpretations for the variations in the magnetization of this interval. First, the variation may be a reliable record of the geomagnetic field at the time of sedimentation. We discount this possibility, primarily because depositional remanence would probably have been randomized during soft-sediment slumping and/or drilling disturbance. The second explanation is that the three reversed-polarity samples contain a drilling overprint with a higher coercivity than is observed in other samples from this site. In all three of these samples the observed remanence direction isolated during demagnetization is not significantly different from the overprint direction. The third possibility is that these samples are from rotated blocks within a debris flow.

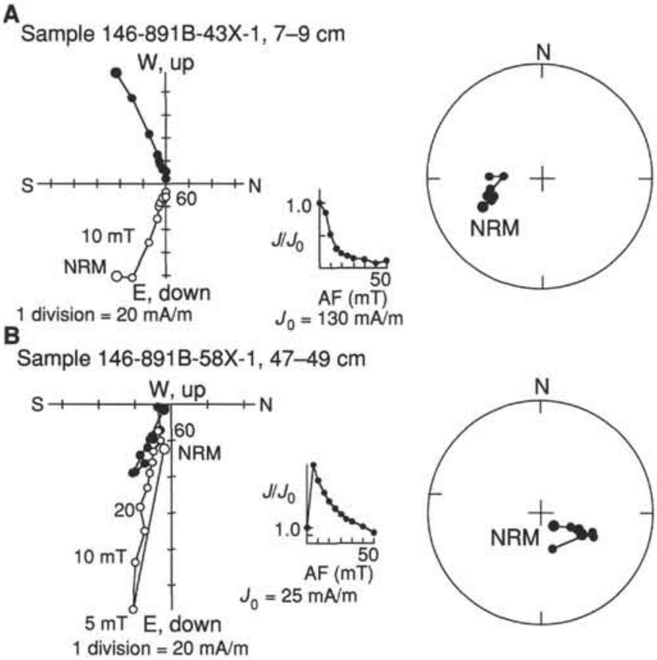

Figure 16. Demagnetization plots of two samples from Hole 891B. Symbols and conventions as in Figure 15. **A.** Behavior of a sample with little overprint. **B.** Behavior of a sample with a larger overprint removed by 5-mT AF demagnetization.

AF demagnetization in Hole 891B showed stable, decreasing remanence intensity, from which well-defined characteristic remanence directions were obtained. The values of the median destructive field (MDF) of most samples from Site 891 were less than 30 mT. In some samples, a reversed drilling-related overprint, which was removed by 5- to 10-mT demagnetization fields, was found. Examples of these sample demagnetizations are shown in Figure 16. In contrast to Site 889, we saw no noticeable high-coercivity component in most samples from Hole 891B. The majority of IRM is acquired between 0.02 and 0.1 T in most samples from Hole 891B (Fig. 17). The characteristics of the demagnetization behavior and the IRM acquisition in the samples from Hole 891B are consistent with those of magnetite, which suggests that the characteristic remanence is probably primary, rather than related to sulfur diagenesis. In conjunction with the findings of the paleontologists (see "Biostratigraphy" section, this chapter), we have placed all of Holes 891A and 891B in the Brunhes (N) Chron, placing a maximum depositional age of the sediments from the bottom of Hole 891B at 0.780 Ma (Cande and Kent, 1992).

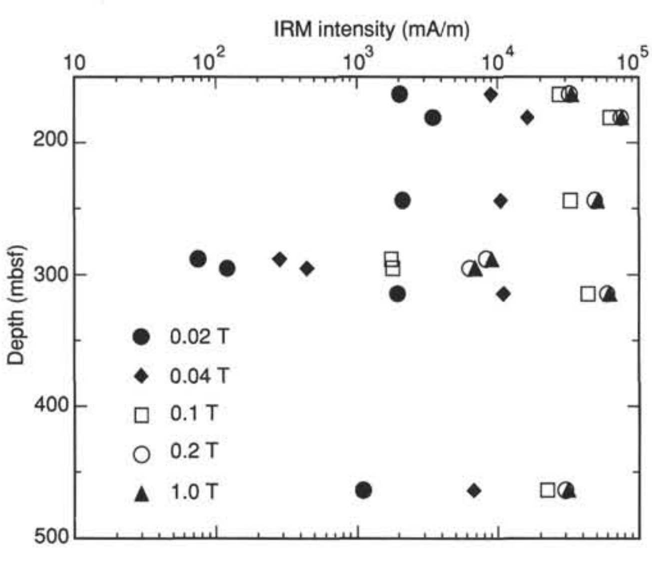

Figure 17. Isothermal remanent magnetization (IRM) acquisition results from Hole 891B. The IRMs were generated with the five applied field steps shown.

Several samples from three intervals in Hole 891B show more erratic demagnetization behavior. These samples were found at 181.4 mbsf, in the interval from 286.6 to 295.4 mbsf, and at 411.3 mbsf (Fig. 18). As shown in Figure 17 the majority of the IRM in samples from the interval from 286.6 to 295.4 mbsf is acquired above 0.1 T. The saturation IRM intensity is also substantially smaller than in other samples. The high coercivity and erratic AF-demagnetization behavior are consistent with the behavior of pyrrhotite and greigite (Dekkers, 1988; Musgrave et al., 1993), so magnetic sulfides are the most likely remanence carriers in these samples.

Rock Magnetism

Demagnetization experiments revealed that there are three components of magnetization in the sediment at this site: the low-coercivity drilling overprint, the primary magnetization, and the high-coercivity component. To examine the drilling overprint, two pairs of samples were taken from neighboring drilling-deformation biscuits of sediment from Hole 891B and their remanent magnetizations were compared. Because each biscuit represents disturbance and probable rotation of the sediment during coring, the horizontal components acquired before coring are expected to differ between neighboring biscuits. The sampled pairs of biscuits are spaced 2 cm apart, so we are confident that the magnetic fields that affected them after drilling are nearly the same. Only the components removed between 0 and 5 mT share similar declinations between the two biscuits (Fig. 19). The lack of similarity of the more stable components may indicate that there is little syn- or post-drilling overprint in these samples.

Magnetic susceptibility from the MST varies between 1 and 600 $\times 10^{-8}$ SI units (Fig. 20). The susceptibility shows decreases at about 296 and 445 mbsf. The higher IRM coercivity marking the likely presence of magnetic sulfides and the reduction in saturation IRM magnitude were also found at about 290 mbsf. The two large decreases in susceptibility coincide with the intervals in which significant biogenic silica was observed in the preliminary core descriptions. The interpretation of the relationship of these magnetic measurements with geochemical indicators awaits shore-based work.

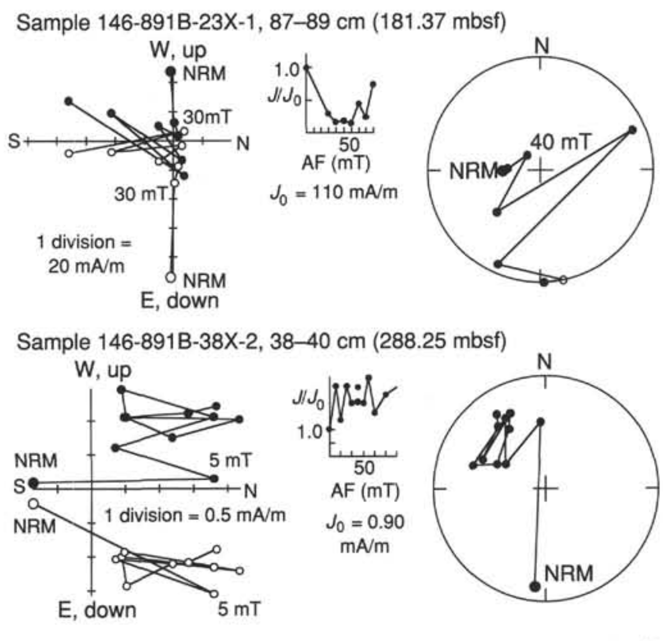

Figure 18. Examples of erratic demagnetization behavior associated with magnetic sulfides. Symbols and conventions as in Figure 15.

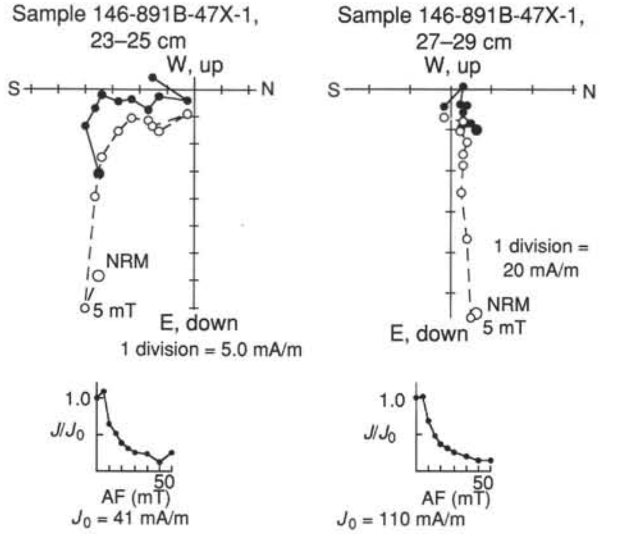

Figure 19. Demagnetization plots comparing the behavior of two adjacent drilling biscuits.

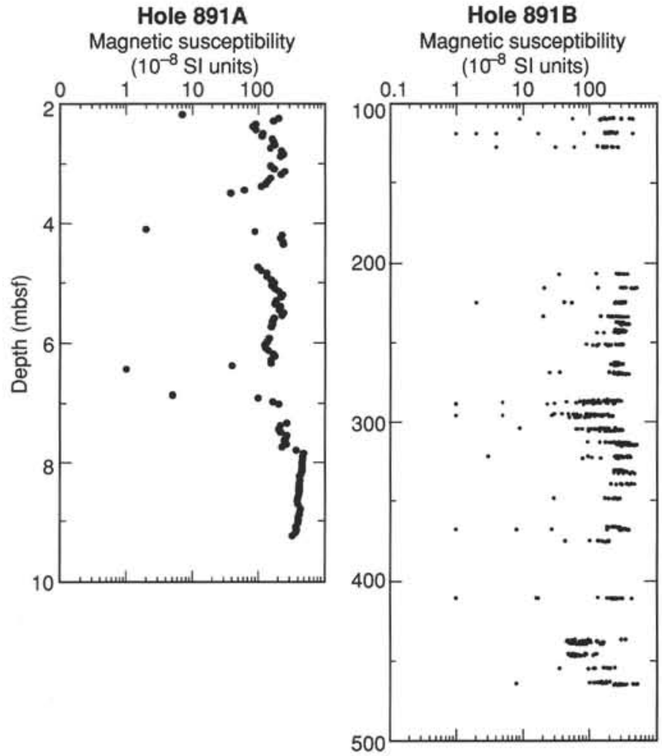

Figure 20. Multisensor (MST) track magnetic susceptibility results from Holes 891A and 891B. Note difference in depth scales.

STRUCTURAL GEOLOGY

Introduction

The 470-m-long cored interval at Site 891 can be divided into five distinct structural domains, based on the development of fracture fabrics and microstructures (Fig. 21). In at least three locations, fabrics indicative of the development of fault zones were recovered; other fault zones may be present in the cored interval but may not have been sampled owing to the low recovery at this site. The site is characterized by a marked downhole repetition of intervals lacking structural fabric, intervals exhibiting distinct distributed fracture fabrics, and localized intervals of fault fabric development. Because lithologic variation at this site is only slight (see "Lithostratigraphy" section, this chapter), we interpret these variations in fabric development as fault controlled. Structural interpretation at this site is unfortunately severely limited by the poor core recovery and lack of recognizable bedding features.

The structural styles developed in each domain are described herein, in downhole order. Note that all sub-bottom depths are approximate and may actually be up to 9 m deeper because of the ODP convention of locating partially recovered cores at the top of the cored interval. Orientation data from Site 891 are presented in Table 4. Structural measurements are expressed in terms of true dips, but azimuthal data are presented only in the core reference frame (see "Explanatory Notes" chapter, this volume). Unfortunately, reorientation of the measurements from Site 891 into true geographic coordinates was not possible during Leg 146. Furthermore, multishot orientations were not obtained for the APC cores from Hole 891A. Paleomagnetic reorientation of selected structural measurements from Site 891 will be made post-cruise.

Domain I (0–198 mbsf)

In Hole 891A, the three APC cores exhibit probable debris-flow deposits interbedded with fine to medium sand, dipping at about 38°. An apparently highly strained and steeply dipping interval in Core 146-891A-2H probably represents flow-in drilling disturbance, but could be a tectonically formed, near-surface shear zone. In Hole 891B, there is a complete lack of data from the seafloor to 84 mbsf owing to the lack of recovery. The poorly recovered interval from 84 to 198 mbsf is marked by the occurrence of sparsely developed deformation bands (for definition, see "Structural Geology" section, "Site 889" chapter, this volume) in Cores 146-891B-20X, -23X, and possibly in -14X. Defor-

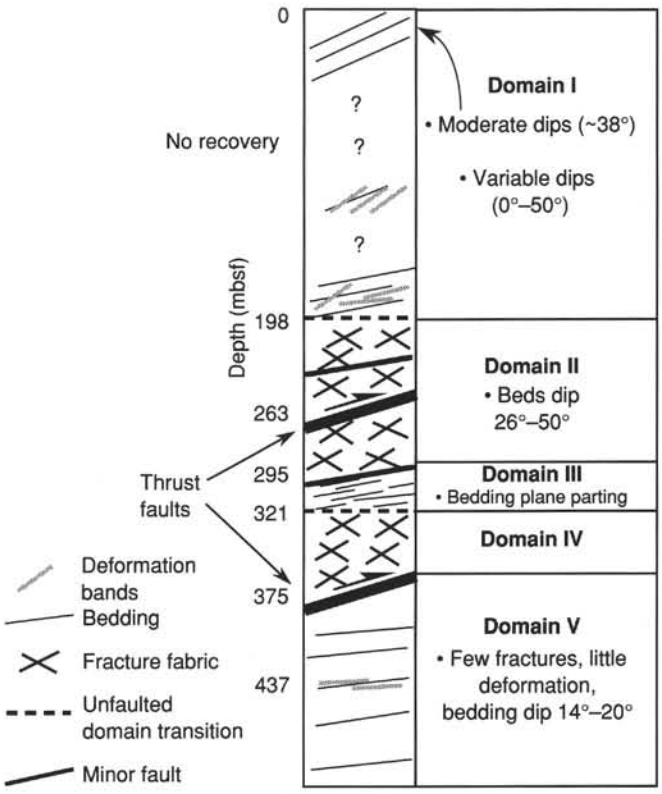

Figure 21. Diagrammatic illustration of structural style in the five domains identified at Site 891, including location of major faults identified in recovered material. Note that this figure assumes that recovered material is representative of the cored interval as a whole.

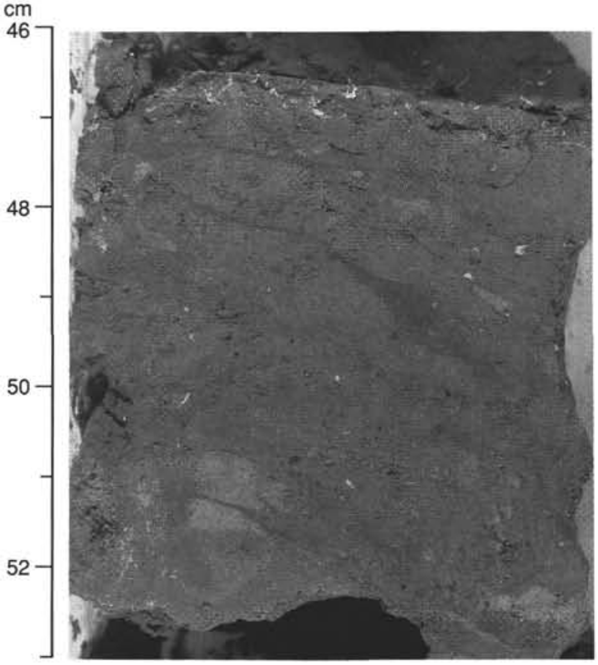

Figure 22. Broken formation in Section 146-891B-33X-1, 46–53 cm (263 mbsf). Disrupted silt beds are bounded by anastomosing dark shear zones. Dip of the fabric is about 27°, down from left to right. Stratal disruption can be seen from 50 to 53 cm.

mation bands in the clayey silts in this interval dip variably (16° to 78°), forming conjugate sets in some places. They are 0.5 to 1 mm wide and occur individually or in small groups, but are not pervasive. Deformation bands are evidence for contractile strain, and may or may not be associated with a discrete fault zone (Karig and Lundberg, 1990).

Core 146-891B-16X, at 127 mbsf, contains recumbently folded laminae with a subhorizontal axial plane. It is not clear whether this fold represents drilling deformation or a natural structure; its shape and axial inclination is consistent with slump folding.

Domain II (198–298 mbsf)

Core 146-891B-25X marks the onset of the first fractured domain at 198 mbsf. This domain persists to 278 mbsf and is characterized by pervasive, spaced fracture development in the recovered cores. The fractures are open, some are slightly polished, and they do not generally exhibit slickenlines. The fractures typically exhibit a dominant direction, dipping 35° to 60°, and a spacing consistently less than 1 cm. We interpret this fabric as a weak incipient scaly foliation, indicative of distributed shortening, and refer to it as "fracture fabric" henceforth.

Within this fractured interval, there are two zones exhibiting evidence for local concentration of shear. The first is in Section 146-891B-28X-CC (225 mbsf), where 12 cm of incipient scaly fabric was recovered. The second, and much better developed, shear zone is in Cores 146-891B-33X and -34X, which both exhibit the development of a scaly foliation. Core 146-891B-33X, at approximately 263 mbsf, contains a 13-cm-thick interval of broken formation (Fig. 22). In this interval, disrupted beds of sandy silt are bounded completely by anastomosing, millimeter-scale, dark, muddy shear zones. The broken formation has a well-developed semiplanar fabric, dipping 27°. The fracture surfaces on the ends of coherent pieces from this interval exhibit downdip slickenlines. Below this relatively thin interval of broken formation, the scaly foliation is present through Core 146-891B-38X (down to 295 mbsf), but with decreasing intensity downward.

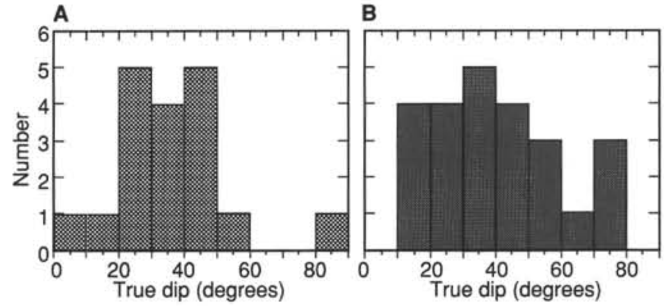

Figure 23. Dip histograms for structural Domains III and IV. **A.** Dip of bedding-plane parting (fissility) in Domain III (295–321 mbsf). Note the strongly preferred moderate dip. **B.** Dip of fractures in Domain IV (321–395 mbsf). Note the wider variability in dips and the addition of a component of steeper fractures, probably superimposed on fractures controlled by the moderately dipping fissility of Domain III.

Core 146-891B-38X (295 mbsf) contains another concentration of shear zone deformation bands surrounding a disrupted sandy bed. The system of bands dips 35°. The sand appears to be part of a debris-flow deposit, so it is difficult to determine whether it is also an example of tectonic stratal disruption or whether the deformation bands are simply coincident with chaotic deposits of nontectonic origin. If they are tectonic, then another, probably minor, fault zone is indicated at 295 mbsf.

The 90-m interval of Domain II is thus an interval of pervasive fracture fabric, containing two probable shallowly dipping fault zones at 263 and 295 mbsf, and containing one other probable minor fault at 225 mbsf. The fabric, dip, and tectonic setting (see "Seismic Stratigraphy" section, this chapter) suggest that all three are thrust faults. Broken formation is typical of thrust faults in accretionary prisms, and, as at Site 889, we interpret the fracture fabric as indicative of bulk distributed strain in the hanging wall over the thrust faults at 263 and 295 mbsf.

Domain III (295–321 mbsf)

From Cores 146-891B-39X to -41X, the sediments do not exhibit fracture fabric. These cores consist of interbedded silt and fine to medium sand. The only fabric is a hackly parting in the silty intervals, interpreted as fissility. This fabric is bedding-parallel in several locations with identifiable bedding traces. Open fractures that are not parallel to the fissility are rare and are interpreted as drilling-induced. Fissile parting surfaces are spaced less than 5 mm apart, and dip dominantly from 24° to 47° (Fig. 23A). Fissility is interpreted as the result of the depositional alignment of platy minerals enhanced by compaction (Lundberg and Moore, 1986) and does not indicate shear deformation.

Domain IV (321–383 mbsf)

There is no evidence for a fault zone at the Domain III/IV boundary at about 321 mbsf. Core 146-891B-42X marks the resumption of fracture fabric development, which persists to the depth of Core 146-891B-48X. This interval of about 62 m is characterized by pervasive fracturing of the silty sediments, similar to Domain II above. The sandy sediments are more disturbed by drilling, and generally do not show the closely spaced fractures. Fracture surfaces are curviplanar, somewhat polished, and locally show slickenlines of variable orientation. The fracture planes occur in anastomosing sets of highly variable dip (Fig. 23B). Shallowly dipping fractures appear to parallel the fissility, but a significant proportion of the fractures dip steeply, up to 78°.

Table 4. Structural data from Holes 891A and 891B.

Core, section, interval (cm)	Identifier	Core face orientation (degrees) Apparent dip	Core face orientation (degrees) Direction	Second orientation (degrees) Apparent dip	Second orientation (degrees) Direction	Corrected core reference frame (degrees) Strike	Corrected core reference frame (degrees) Dip	Corrected core reference frame (degrees) Direction	Comments
146-891A-									
2H-1, 33–48	Color change	68	90	15	180	6	68	E	Maybe flow-in, not real?
2H-1, 76–92	Color change	70	90	18	180	7	70	E	Maybe flow-in, not real?
2H-CC, 10–15	Color change	42	270	62	0	244	64	N	Maybe flow-in, not real?
3H-1, 30–36	Color change	56	270	33	0	204	58	W	
3H-1, 46–50	Bedding	30	270	27	180	138	38	W	Good measurement.
146-891B-									
10X-1, 20	Bedding								Subhorizontal.
14X-1, 35	Deformation bands	58	270	0	199	199	59	W	Parallel sets of faint bands. Perhaps vein structures or deformation bands. Some faint conjugate sets at same location.
16X-1, 20–42	Fold								Fold: subhorizontal axial plane of folded laminae.
20X-1, 56–64	Deformation bands	40	270	78	0	260	78	N	Sets of dark seams in clayey silt.
20X-1, 56–64	Deformation bands	80	270						
20X-1, 66–74	Deformation bands	30	270						
20X-1, 66–74	Deformation bands	65	270						
23X-2, 26–38	Deformation bands	32	270	23	0	214	37	W	Silty sand with dark seams-not lithified.
23X-2, 26–38	Deformation bands	24	270	10	0	202	26	W	
23X-2, 15–17	Deformation bands	22	90	31	0	304	36	N	Conjugate to above two?
23X-CC, 4–14	Deformation bands	20	270						
23X-CC, 3–5	Deformation bands	12	270	11	0	222	16	W	
23X-CC, 6–9	Deformation bands	27	270	25	0	222	35	W	
25X-1, 30–50	Fractures	45-55	270						
27X-1, 10–16	Bedding	50	90	28	0	336	53	E	
28X-1, 50–65	Scaly fractures								Pieces in lower part of core.
29X-1, 12–15	Fractures	33	90	23	0	327	38	E	Dominant fabric direction.
30X-2, 59–66	Fracture	51	270	13	180	169	51	W	Dominant fracture in scaly fabric.
30X-2, 63–64	Fracture	11	270	5	0	204	12	W	Second fracture intersecting above fracture.
31X-1, 23–25	Fracture	24	90	40	0	298	44	N	Fracture fabric.
31X-1, 1–12	Fracture	10	90	25	180	69	26	S	
31X-1, 37–39	Fracture	20	270	21	180	133	28	S	
31X-1, 45–51	Fracture	49	270	25	180	158	51	N	
31X-1, 67–71	Fracture	40	90	21	0	335	43	E	
31X-1, 94–98	Fracture	32	90	13	0	340	33	E	
31X-1, 128–130	Fracture	15	90	15	0	315	21	N	
31X-1, 127–130	Fracture	73	90	58	0	334	75	N	
31X-2, 4–5	Fracture	13	270	5	0	201	14	W	
31X-CC, 12–16	Fracture	41	90	10	0	349	42	E	
31X-CC, 28–32	Fracture	43	90	9	0	350	43	E	
32X-1, 45–49	Fracture	52	90	20	180	16	53	E	Fracture fabric.
32X-1, 28–30	Fracture	32	270	16	180	155	35	W	
32X-CC, 36–37	Fracture	12	270	7	0	210	14	W	
33X-1, 20–23	Fracture	27	270	7	180	166	28	W	
33X-1, 31–34	Fracture	38	270	20	0	205	41	W	
33X-1, 46–47	Broken formation fabric	4	90	27	180	82	27		Approximate because core has been handled; downdip slickenlines are present.
34X-1, 12–15	Fracture	26	270	11	180	158	28	W	Pervasively fractured pebbly siltstone.
34X-1, 45–48	Fracture	32	270	36	180	131	44	S	Fracture spacing of 2–5 mm.
35X-1, 67–71	Fracture	35	90	50	0	300	54	N	Fractured siltstone.
35X-1, 130–132	Fracture	18	90	19	180	47	25	S	
38X-1, 109–111	Disrupted bed plane	27	270	26	0	224	35	W	Sand layer bounded by dark shear zones.
39X-1, 78–80	Parting	28	270	6	180	169	28	W	Bedding-plane fissility?
39X-1, 132–136	Parting	39	90	34	0	320	47	E	
39X-1, 16–19	Fracture	39	90	20	180	24	42	E	
40X-1, 39–62	Fracture	84	90	20	180	2	84	E	
40X-1, 50–54	Fracture	36	90	55	0	297	58	N	
40X-1, 56–58	Parting	25	90	5	0	349	25	E	
40X-1, 63–66	Parting	30	90	3	0	355	30	E	
40X-1, 67–69	Parting	12	270	41	0	256	42	N	
40X-1, 73–78	Parting	40	270	15	180	162	41	W	
40X-1, 82–84	Parting	31	270	11	180	162	32	W	
40X-1, 92–94	Parting	21	90	13	0	329	24	E	
41X-1, 12	Bedding	7	270	25	0	255	26	N	Sand/silt layering.
41X-1, 42–46	Parting	25	90	17	0	327	29	E	Dominant parting.
41X-1, 42	Fracture	14	270	10	0	215	17	W	Single fracture crosscuts dominant parting.
41X-1, 56–58	Fracture	34	270	5	0	187	34	N	
41X-2, 41–43	Bedding	44	270	20	180	159	46	W	Layer of wood fragments.
41X-2, 98–99	Bedding	5	270	5	0	225	7	W	Clayey silt and sand.
41X-2, 108–112	Fracture	30	90	17	180	28	33	E	
42X-1, 30–35	Fracture	42	270	2	0	182	42	N	Light gray silt.
42X-1, 47–50	Fracture	26	270	10	0	200	27	W	
42X-1, 106–107	Fracture	31	90	10	0	344	32	E	
42X-1, 106–107	Fracture	14	270	5	180	161	15	W	
43X-1, 0–5	Fracture	51	90	6	0	355	51	E	This core more fractured and lithified than Core 146-891B-42X.
43X-2, 20–29	Fracture	71	90	19	180	7	71	E	
43X-2, 30–34	Fracture	71	90	40	0	344	72	E	
43X-2, 54–57	Fracture	3	90	36	0	274	36	N	
43X-2, 68–70	Fracture	25	270	33	0	234	39	N	
43X-2, 81–87	Fracture	61	270	39	180	156	63	W	
43X-2, 113–116	Fracture	78	90	36	0	351	78	E	

Table 4 (continued).

Core, section, interval (cm)	Identifier	Core face orientation (degrees) Apparent dip	Direction	Second orientation (degrees) Apparent dip	Direction	Corrected core reference frame (degrees) Strike	Dip	Direction	Comments
43X-2, 113–116	Fracture	29	90	19	0	328	33	E	
43X-2, 113–116	Fracture	7	90	11	180	58	13	S	
43X-2, 113–116	Fracture	53	270	24	0	199	54	W	
43X-2, 126–127	Fracture	8	270	20	180	111	21	S	
43X-2, 141–143	Fracture	19	270	17	180	138	25	W	
44X-2, 15–20	Fracture	12	270	23	0	243	25	N	Fracture fabric in clayey silt.
44X-2, 15–20	Fracture	31	270	33	0	227	42	N	
44X-2, 15–20	Fracture	48	90	21	0	341	51	E	
44X-2, 25–30	Fracture	37	90	40	0	312	48	N	
47X-1, 48–53	Fracture	42	270	10	180	169	43	N	
47X-1, 63	Fracture	5	90	9	0	299	10	N	
48X-CC, 6–11	Fracture	38	90	3	0	356	38	E	Pervasive well-developed scaly fractures.
48X-CC, 8–10	Fracture	16	270	0	0	180	16	W	
52X-1, 36–39	Fissility	23	270	20	0	221	29	W	Fabric looks more like fissility than scaly fabric.
55X-1, 11–13	Bedding	13	270	5	0	201	14	W	Good bed: sand/clay contact.
55X-1, 10–13	Deformation bands	4	90						Many anastomosing bands of variable orientation.
58X-CC, 37	Bedding	9	90	20	180	66	22	S	Sand/clay contact.

This incipient scaly fracturing begins in Core 146-891B-42X and progressively increases in intensity through Cores 146-891B-43X and -44X. Fractures are pervasive on a scale of millimeters. As a result of the especially poor recovery between 332 and 366 mbsf, it is unknown whether fracturing persists throughout this interval. Core 146-891B-48X, at a depth of 375 mbsf, recovered about 50 cm of the most highly developed scaly fracturing at Site 891. The scaly chips and intact fragments are more indurated than the softer sediments above and below, suggesting strain hardening (see also "Downhole Logging" and "Physical Properties" sections, this chapter). Accordingly, we infer a fault zone in Core 146-891B-48X. This interpretation is supported by the abrupt transition to sediment lacking fracture fabric in Core 146-891B-49X, marking the beginning of structural Domain V (described in the following). Core 146-891B-48X marks the deepest occurrence of fracture fabric recovered in this hole.

Domain IV is thus a fractured interval about 62 m thick, with a fault zone at the base, overlain by pervasively fractured sediment above the fault. It is similar to Domain II in the presence of a concentrated shear zone with a broad zone of fracture fabric developed in the hanging wall.

Domain V (383–472 mbsf)

From 383 mbsf to the total depth of Hole 891B (472 mbsf), there is evidence that a reduced amount of strain is recorded in the recovered cores compared to the domain above. Cores 146-891B-49X through -58X contain no fracture fabric, and are less indurated than those above. Fissility, interpreted as a bedding plane parting, is locally present in Cores 146-891B-52X and -56X. Section 146-891B-55X-1, 10–13 cm (437 mbsf), contains a 3-cm-thick zone of generally subhorizontal, anastomosing deformation bands. This zone occurs in one of the few intervals of relatively good recovery, so the bands may not be restricted to this interval; nevertheless, it is the only location where they were recovered below Core 146-891B-23X. The presence of deformation bands may record an interval of concentrated shear, but is not unequivocal evidence of proximity to a fault. The index properties and inorganic geochemistry both show significant discontinuities at the same depth (see "Physical Properties" and "Inorganic Geochemistry" sections, this chapter), suggesting that there is a fault zone somewhere between Cores 146-891B-52X and -55X (410–446 mbsf). This interpretation is not inconsistent with the observed structures, but no fault fabric was recovered.

Although the cores in Domain V are mostly badly disturbed, some evidence of bedding attitude was preserved (Fig. 24). In Core 146-891B-52X, a dip of 29° was measured on a bedding-plane parting surface. In Cores 146-891B-55X and -58X, attitudes of 14° and 22°, respectively, were measured. These values indicate that the bedding in Domain V dips at a shallower angle than in the more-deformed domains above.

Magnetic Anisotropy

Anisotropy of magnetic susceptibility (AMS) results for Hole 891B (Fig. 25) can be used to evaluate the rock fabrics associated with the observed structures, the occurrence of physical properties discontinu-

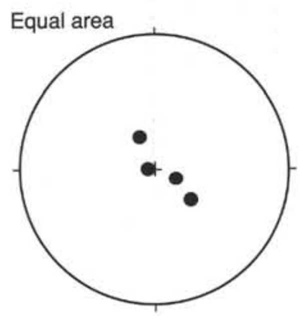

Figure 24. Dip of bedding in the core reference frame in Domain V. Bedding dip is shallower than in Domains III and IV above.

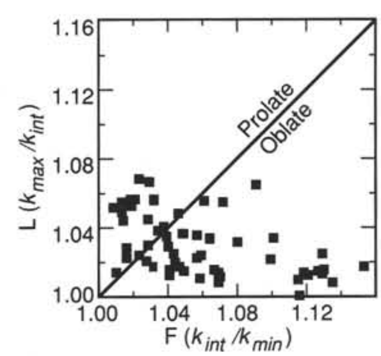

Figure 25. Flinn-type diagram of the AMS results from Hole 891B showing the AMS ellipsoid shape. The vertical axis is magnetic lineation (k_{max}/k_{int}), the horizontal axis is magnetic foliation (k_{int}/k_{min}). Results plotting in the upper left area have prolate ellipsoid shapes, results plotting in the lower right have oblate ellipsoid shapes. See text for discussion.

ities (see "Physical Properties" section, this chapter), and geochemical anomalies in fluid and gas geochemistry (see "Organic Geochemistry" and "Inorganic Geochemistry" sections, this chapter). Like the results from Site 889, the magnetic anisotropy agrees well with the observed structures, with lineated magnetic fabrics observed from intervals with faults and/or deformation bands. A typical example is in Section 146-891B-14X-1. Where weakly developed deformation bands occur, a weak magnetic lineation was observed; elsewhere in Section 146-891B-14X-1, a foliated magnetic fabric consistent with sediment compaction was observed (Fig. 26A). Results for the interval from 127 to 128 mbsf, in which a geochemical anomaly occurs (see "Inorganic Geochemistry" section, this chapter), but where no structures were observed, show an oblate magnetic ellipsoid shape (Fig. 26B), which is most likely a sediment-compaction fabric. Other samples from the interval from 110 to 155 mbsf, in which few structures indicative of deformation occur, have AMS fabrics that are oblate, with $F > 1.07$ and $L < 1.03$, and are most consistent with sediment-compaction fabrics (Fig. 26A). In contrast, AMS results from intervals in Hole 891B (Fig. 27) with faults or deformation bands, physical properties discontinuities, or inorganic and organic geochemical anomalies have ellipsoid shapes that are either lineated ($L > F$) or else shifted from the oblate sediment-compaction fabrics toward prolate ellipsoid shapes. These fabrics indicate that modification of the sediment fabric has occurred, most likely via development of a preferred orientation during deformation. This is again consistent with the core-scale structural observations of faults in the majority of the intervals with either physical properties or geochemical anomalies.

Structural evidence for faulting is not found, however, where the major geochemical anomalies and physical properties discontinuities are observed in Domain V (440–447 mbsf). Magnetic fabric results from the intervals between 410 and 465 mbsf in which structures, physical properties discontinuities, and chemical anomalies occur (Fig. 28) indicate that weak lineations/foliations are associated with the deformation bands and geochemical anomalies in Cores 146-891B-55X and -56X, with a more strongly developed foliation associated with the discontinuity/anomaly occurring at 440 mbsf. Results from Core 146-891B-52X (410.5–419.3 mbsf) show fabrics shifted toward prolate (linear) shapes and an anomaly in organic geochemistry (Fig. 28D). This observed lineation, as well as the deformation bands found in Core 146-891B-55X, lend support to the existence of a fault suggested by physical properties data.

Summary and Conclusions

Structural evidence from Site 891 indicates that the site is dominated by deformation associated with the development of several thrust faults, the most well developed of which are at 263 and 375 mbsf. The

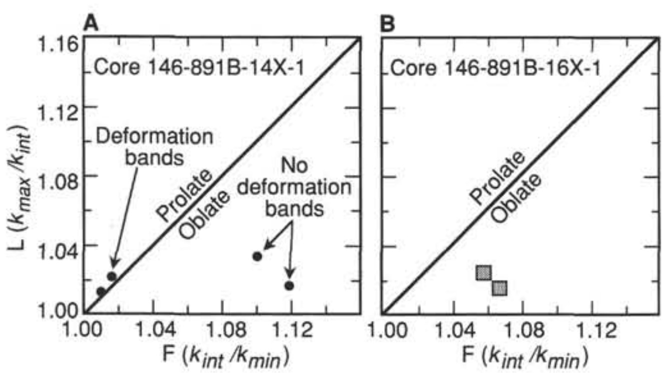

Figure 26. Flinn-type diagrams of AMS fabrics. **A.** Results from 110 to 111 mbsf show a weakly lineated magnetic fabric associated with weak deformation bands and a well-developed sediment foliation elsewhere. **B.** Results from 127 to 128 mbsf, which is within an interval with an inorganic geochemistry anomaly, show foliations consistent with unsheared sediment fabrics.

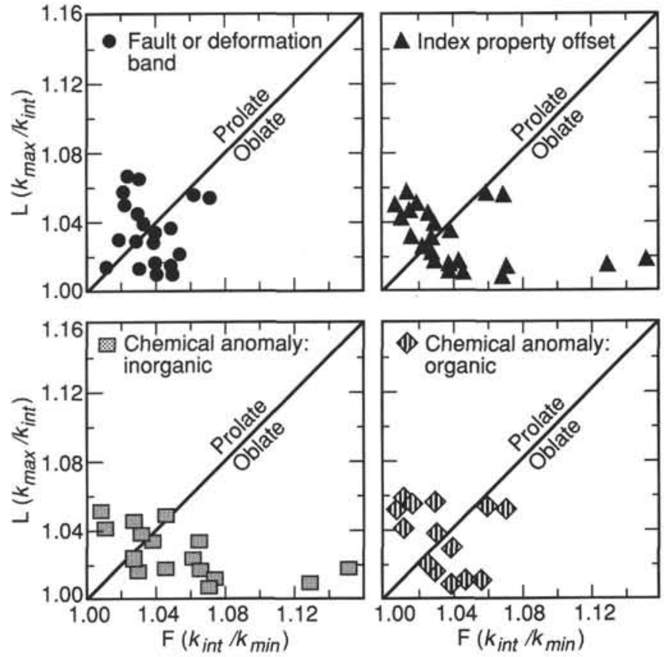

Figure 27. Flinn-type diagrams of AMS fabrics from intervals in Hole 891B with faults or deformation bands, physical properties discontinuities, and inorganic and organic geochemistry anomalies.

recovered cores exhibit contrasting intervals of greater and lesser intensity of fracture-fabric formation and localized deformation bands, separated by discrete shear zones, which are interpreted as fault zones (Fig. 21). The spatial distribution of these intervals suggests a pattern to the development of the faults and the fracture fabrics. The two faults for which we have the strongest structural evidence (263 and 375 mbsf)

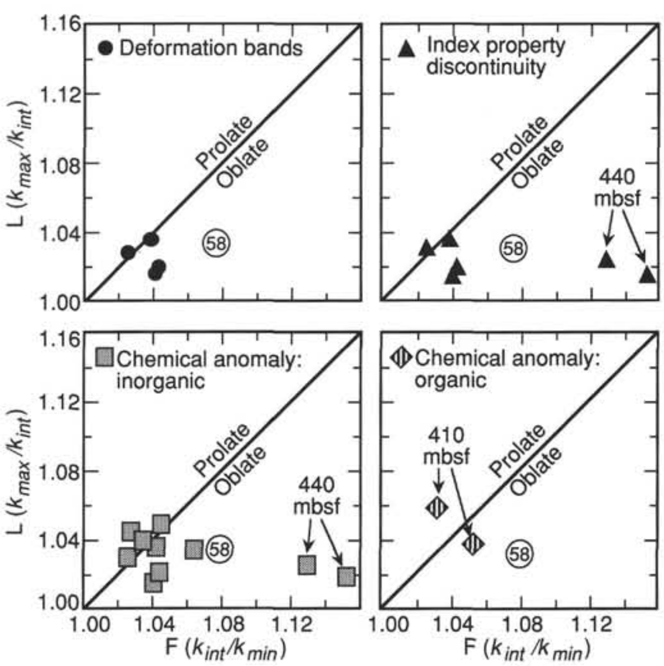

Figure 28. Flinn-type diagrams of AMS fabrics from the intervals between 410 and 465 mbsf in Cores 146-891B-52X to -58X in which deformation bands, physical properties discontinuities, and inorganic and organic geochemistry anomalies occur. Plotted for reference (circled 58) is the relatively undeformed compaction fabric from Core 146-891B-58X. See text for discussion.

each lie near or at the base of the fractured domains (Domains II and IV, respectively). Each of the fractured domains terminates upward into an unfractured, fissile interval, without evidence for a faulted contact. Below the faults, the transition back into unfractured material is relatively abrupt. Taken together, this pattern suggests that there is a deformation gradient in the hanging wall of each of these faults, with about 60 m each of fracture fabric above, dying out upward into relatively undeformed intervals (Domains I and III). Below 375 mbsf, the sediments have significantly fewer strain indicators, and there is no visible structural fabric. The presence of deformation bands at 437 mbsf suggests some localization of shear at this interval, so a possible fault zone suggested by the physical properties cannot be ruled out. Magnetic fabric indicating lineation in this interval lends support to the hypothesized fault at about 440 mbsf.

ORGANIC GEOCHEMISTRY

Overview

The sedimentary sequences cored at Site 891 have interbeds of sand and clay that are relatively low in organic carbon (0.2%–0.8%) and in extractable bitumen or pyrolyzable kerogen. Still, dissolved sulfate is exhausted by 200 mbsf. The hydrocarbon gas contents are predominantly methane and typically less than 10 ppmv in the sulfate-reduction zone, but rise sharply to moderate levels in the lower half of the hole, once sulfate is depleted. The primary source of the methane is bacterial methanogenesis.

Higher hydrocarbon gases (ethane through hexane) are present in anomalous amounts at certain intervals below 200 mbsf, corresponding to cores with a marked petroliferous odor. The higher hydrocarbons indicate the incursion of thermogenic gas into the sediments. Based on kerogen and bitumen analyses (e.g., pyrolysis, extracts, carbon preference index), the sediments are too immature to have generated these thermogenic gases locally. It is probable that the thermogenic hydrocarbons are migrating along faults, fractures, or permeable beds associated with the accretionary setting. The presence of ethene, which is geologically unstable, supports the possibility that the hydrocarbons are actively moving to the shallower sediments at Site 891.

Organic Carbon

Organic carbon contents (C_{org}) are relatively low at Site 891, varying, in general, between 0.2 and 0.8 wt% (Table 5). Near the surface (i.e., at 4.08 and 5.84 mbsf), C_{org} is higher (0.79 and 0.75 wt%) than in the sediments over the remainder of the upper 100 mbsf (0.00–0.21 wt%). Below 100 mbsf, there is no consistent distribution of organic matter (Fig. 29). There are prominent populations at about 0.2 and 0.8 wt% and a lesser population at about 0.5 wt% (Fig. 30). In Figure 29, 0.2 wt% appears to be the background C_{org} level with sporadic excursions to 0.8 wt%. The C_{org} values are typical of those for the surface sediments of the Oregon margin and are consistent with rapid turbidite-hemipelagite deposition. Wood fragments (see "Lithostratigraphy" section, this chapter) were reported in several cores.

Table 5. Carbon, nitrogen, and sulfur sediment data (based on total dry sediment), Site 891.

Core, section, interval (cm)	Depth (mbsf)	Inorganic carbon (wt%)	$CaCO_3$ (wt%)	Total carbon (wt%)	Organic carbon (wt%)	Total nitrogen (wt%)	Total sulfur (wt%)
146-891A-							
1H-2, 140–150	2.95	0.45	3.75	0.88	0.43	0.034	0.226
1H-3, 103–113	4.08	0.25	2.08	1.04	0.79	0.073	0.078
2H-1, 109–119	5.84	0.26	2.17	1.01	0.75	0.069	0.199
3H-2, 53–68	9.41	0.38	3.17	0.52	0.14	0.009	0.005
146-891B-							
8X-1, 15–20	65.40	0.65	5.41	0.86	0.21	0.017	0.008
11X-2, 16–21	102.59	0.68	5.66	0.68	0.00	0.004	0.003
14X-1, 54–64	110.09	1.17	9.75	1.58	0.41	0.023	0.001
15X-1, 82–90	119.26	0.94	7.83	1.15	0.21	0.013	0.008
16X-1, 57–67	127.92	1.04	8.66	1.17	0.13	0.014	0.146
18X-CC, 26–37	143.92	1.06	8.83	1.27	0.21	0.000	0.043
19X-1, 0–10	153.95	1.00	8.33	1.21	0.21	0.024	1.236
20X-1, 28–38	163.03	1.08	9.00	1.31	0.23	0.028	1.976
21N-CC, 0–5	170.13	0.13	1.08	0.93	0.80	0.046	0.312
22X-1, 55–67	176.71	0.67	5.58	1.26	0.59	0.029	0.000
23X-1, 50–60	181.05	0.59	4.91	1.09	0.50	0.025	0.205
25X-CC, 13–20	196.87	0.64	5.33	0.87	0.23	0.016	0.462
26X-1, 42–46	207.54	0.66	5.50	0.88	0.22	0.023	0.000
27X-1, 15–25	216.10	0.56	4.66	1.01	0.45	0.028	0.255
28X-1, 32–50	225.11	0.70	5.83	0.90	0.20	0.022	0.000
29X-1, 22–29	233.86	0.80	6.66	0.99	0.19	0.024	0.004
30X-1, 75–83	238.39	0.72	6.00	0.92	0.20	0.026	0.000
31X-1, 135–150	243.83	0.72	6.00	0.93	0.21	0.032	0.034
32X-1, 11–17	251.54	0.64	5.33	1.02	0.38	0.032	0.000
33X-1, 0–17	260.29	0.22	1.83	1.03	0.81	0.078	0.195
34X-1, 100–115	264.18	0.41	3.42	0.70	0.29	0.035	0.014
35X-1, 16–28	269.22	0.50	4.17	0.98	0.48	0.051	0.155
36P-1, 0–6	277.80	0.39	3.25	0.87	0.48	0.060	2.311
38X-2, 0–18	287.99	0.73	6.08	0.93	0.20	0.028	0.000
39X-1, 101–118	296.20	0.35	2.92	1.09	0.74	0.089	0.127
40X-1, 0–11	304.06	0.31	2.58	0.99	0.68	0.076	0.104
41X-1, 135–150	314.23	0.60	5.00	0.82	0.22	0.020	0.017
42X-1, 0–18	321.69	0.67	5.58	1.10	0.43	0.031	0.053
43X-1, 10–27	330.59	0.61	5.08	0.83	0.22	0.032	0.013
45X-1, 6–14	348.30	0.54	4.50	0.85	0.31	0.026	0.234
47X-1, 95–110	367.13	0.82	6.83	1.03	0.21	0.023	0.008
48X-1, 0–15	375.08	0.15	1.25	0.93	0.78	0.076	0.130
49X-1, 23–29	384.16	1.07	8.91	1.25	0.18	0.019	0.000
50X-1, 17–20	392.99	1.04	8.66	1.36	0.32	0.017	0.000
52X-1, 7–21	410.64	0.89	7.41	1.04	0.15	0.020	0.000
55X-2, 130–150	439.90	0.45	3.75	1.11	0.66	0.076	0.000
56X-1, 72–89	446.61	0.53	4.41	1.17	0.64	0.077	0.000
58X-2, 15–27	465.21	0.88	7.33	1.06	0.18	0.025	0.000

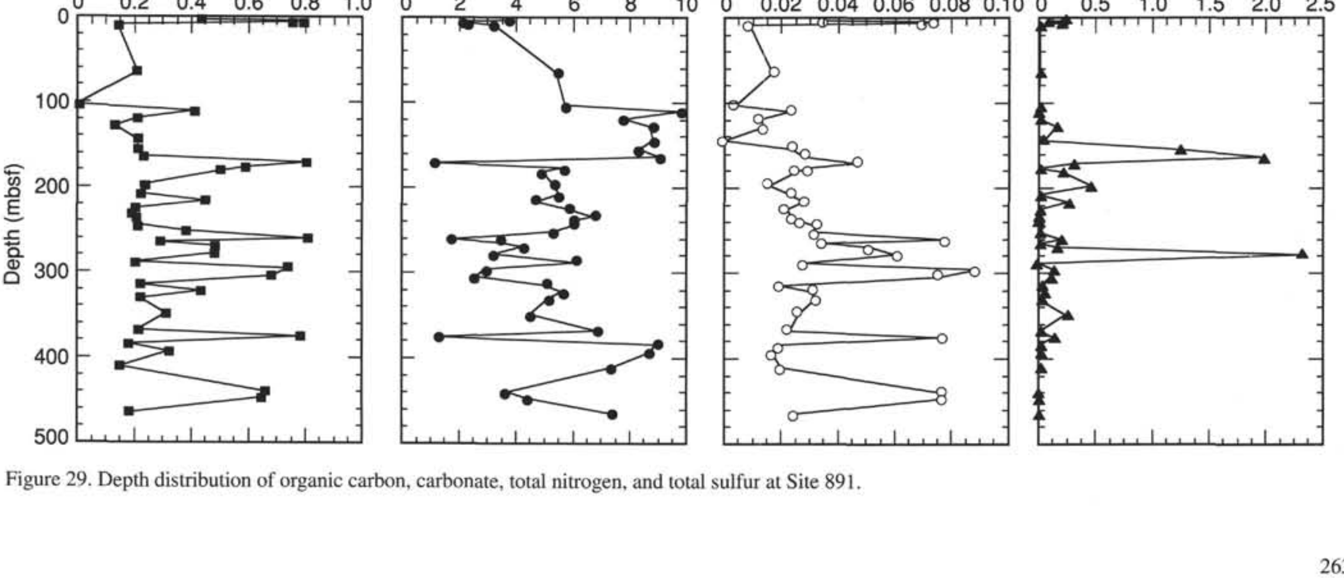

Figure 29. Depth distribution of organic carbon, carbonate, total nitrogen, and total sulfur at Site 891.

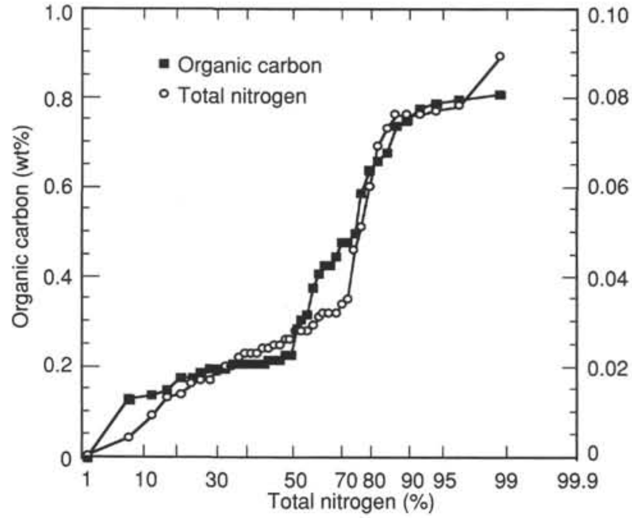

Figure 30. Statistical plot (cumulative proportions, log scale) showing the predominant organic carbon and total nitrogen populations at Site 891.

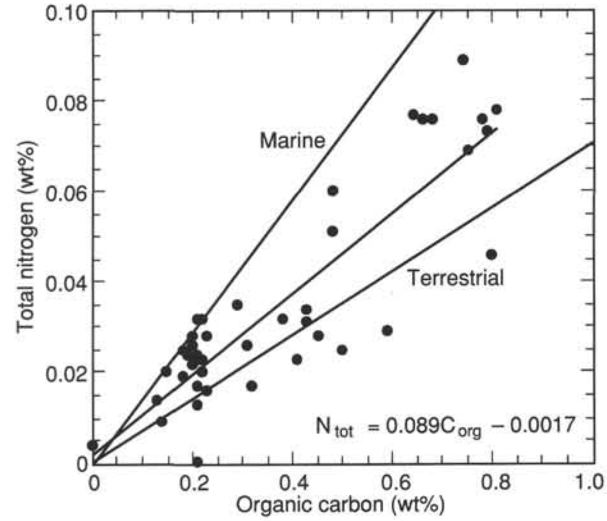

Figure 31. Cross plot of organic carbon and total nitrogen showing a strong terrestrial-hemipelagic influence at Site 891. Typical marine and terrestrial C:N relationships are drawn for reference.

The carbonate contents at Site 891 vary, in general, from 3 to 7 wt% (Fig. 29 and Table 5). Two distinctive low values (1.08 and 1.25 wt%) were recorded at 170.13 and 375.08 mbsf, respectively. Carbonate contents are elevated to between 8 and 10 wt% in two zones: 110.09–163.03 and 384.16–392.99 mbsf, with no apparent correlation between the organic and inorganic carbon contents.

Total Nitrogen

The total nitrogen (N_{tot}) varies broadly with the organic carbon contents in Holes 891A and 891B (Table 5). Higher values of N_{tot} (0.073 and 0.069 wt%) are recorded near the surface (i.e., 4.08 and 5.84 mbsf) than in the sediments over the remainder of the upper 100 mbsf (<0.02 wt%; Fig. 29). Similar to C_{org}, higher N_{tot} contents (0.08 wt%) are sporadic downhole, against a background population of 0.02 wt% (Fig. 30).

The correspondence of N_{tot} with C_{org} contents is illustrated in Figure 31. The regression gives a C:N ratio of about 11.2:1, which indicates a mixed marine/terrestrial organic source, with the former richer in nitrogen. The considerable degree of scatter observed in the C/N ratio in Figure 31 is because of the variations in the lithologies drilled.

In comparison to the Vancouver Island margin, the organic matter at Site 891 is similar in composition, but slightly higher in content than at Sites 888, 889, and 890.

Total Sulfur

Total sulfur (S_{tot}) at Site 891 is consistently less than 0.5 wt% (Table 5), except for the two prominent intervals shown in Figure 29. The first S_{tot} excursion at 153.96–163.03 mbsf (1.24–1.98 wt%) is just above a C_{org} maximum and corresponds roughly to the top of the zone of intense sulfate reduction (see "Inorganic Geochemistry" section, this chapter). The second, at 277.8 mbsf (2.31 wt%), is also coincident with a C_{org} maximum. Local intensification of sulfate reduction could account for the buildup of monosulfides and pyrite (see "Lithostratigraphy" and "Paleomagnetism" sections, this chapter).

Headspace Hydrocarbon Gases

Poor sample recovery throughout Hole 891B may have significantly influenced the quality of the headspace measurements, but general trends can be recognized. Concentrations of hydrocarbon gases in the headspace at Site 891 show four distinctive types, corresponding to depth zones:

1. sulfate zone with low methane (0–200 mbsf)
2. zone of bacterial methanogenesis (200–410 mbsf)
3. thermogenic hydrocarbon incursions (250–450 mbsf)
4. bacterial methane zone (440–460 mbsf).

The methane contents in the uppermost 200 m at Site 891 are background levels (i.e., <10 ppmv), except for a single value of 16 ppmv at 164.1 mbsf (Table 6). Below 200 mbsf the methane content increases sharply down to approximately 300 mbsf (Fig. 32). The maximum headspace methane content is 57,000 ppmv, which is similar to values at Site 888 at the Vancouver Island margin. Below 300 mbsf the methane decreases irregularly to a minimum of 6400 ppmv at 410.7 mbsf. At 437.4 mbsf, in the lower section of Hole 891B, the methane levels rise abruptly to about 40,000 ppmv, in what appears to be a geochemical break from the overlying sediments (Fig. 32).

Higher hydrocarbon gases are absent or present in only trace amounts down to 250 mbsf in Hole 891B (i.e., <0.2 ppmv; Table 6). Below 250 mbsf, minor amounts of higher hydrocarbons appear in restricted zones, as seen in Figure 32. At four depths (314.3, 339.4, 366.8, and 410.7 mbsf), C_4 through C_6 alkane homologs are present, with the highest $\sum C_{2+}$ value (= $C_2 + C_{2=} + C_3 + \ldots + C_6$) of 21 ppmv occurring at 314.3 mbsf (Table 6). The methane/ethane (C_1/C_2) ratios calculated for the samples above 250 mbsf are $>10^6$ (Fig. 32) but drop to a minimum value of 3500 at 410.7 mbsf (Sample 146-891B-52X-1).

Most unusual for this study area is the presence of the olefin ethene (C_2H_4) in several samples between 375.5 and 410.7 mbsf. In addition, the cores in which the higher hydrocarbons were found possessed a marked petroliferous/sulfidic odor. This was noticed as the cores were sectioned and during processing in the shipboard laboratory.

Carbon dioxide is also anomalously high in the headspace samples of Hole 891B below 240 mbsf (Table 6). Several samples have CO_2 levels above 10,000 ppmv, and at 314.3 mbsf a maximum of 95,000 ppmv was recorded (Fig. 32). The occurrences of the elevated CO_2 levels correspond to the sample depths with higher hydrocarbons.

Vacutainer Gas

The recovery of cores from Site 891 was poor. The cores were not "gassy" and expansion voids were rare. The four vacutainer samples that could be taken at Site 891 (Table 6) show a trend similar to that seen in the headspace gas analyses. Higher hydrocarbons, ethene, and carbon dioxide are all present in the vacutainers from 315.29, 368.09, and 368.68 mbsf. The fourth vacutainer, at 323.60 mbsf, has signifi-

Table 6. Molecular composition of headspace and vacutainer gases at Site 891.

Core, section, interval (cm)	Depth (mbsf)	O_2	N_2	C_1	CO_2	$C_{2=}$	C_2	C_3	iC_4	nC_4	iC_5	nC_5	iC_6	nC_6	ΣC_{2+}	C_1/C_2
Headspace:																
146-891A-																
1H-3, 0–5	3.03	155935	937857	3	464		0								0	U/D
2H-2, 0–5	6.23	171141	928039	3	3492		0								0	U/D
3H-2, 0–5	8.83	208204	787818	3	3263		0								0	U/D
146-891B-																
3X-CC, 0–2	20.81	142183	963534	4	1501		0								0	U/D
4X-CC, 0–2	29.61	164223	910127	2	963		0								0	U/D
10X-1, 0–5	85.13	184210	736677	5	2932		0								0	U/D
11X-2, 0–5	102.43	205006	807826	8	2067		0								0	U/D
14X-1, 59–64	110.12	196472	838754	7	1157		0	2							2	U/D
15X-1, 16	118.44	105703	1067457	3	275		0	0							0	U/D
16X-1, 49–54	127.82	193098	752829	5	574		0	0							0	U/D
18X-CC, 7–9	145.18	170089	910598	2	2320		0	0							0	U/D
19X-1, 8–10	153.99	184488	715319	2	1158		0	0							0	U/D
20X-1, 142–147	164.15	193889	750667	16	3767		Tr								0	U/D
21N-1, 47–52	172.10	178763	727660	2	1877		Tr								0	U/D
22X-1, 62–67	176.75	188927	742200	2	1318										0	U/D
23X-1, 145–150	181.98	182443	787209	3	1328										0	U/D
25X-1, 56–61	198.79	171084	731476	2	2550										0	U/D
26X-1, 10–15	207.23	146819	1059769	4658	4133										0	U/D
27X-1, 10–15	216.03	205096	806067	944	5463										0	U/D
28X-1, 45–50	225.18	198732	843058	9135	3570										0	U/D
29X-1, 0–4	233.62	182955	743219	21420	5661										0	U/D
30X-2, 85–89	239.97	191709	827795	10065	629			2							2	U/D
31X-2, 0–5	243.93	102125	469106	9924	23399			0							0	U/D
32X-1, 20–25	251.63	164332	772866	40864	13805		1	0							1	4.4×10^4
33X-1, 20–25	260.43	171706	713942	31428	6102			0							0	U/D
34X-2, 50–53	265.12	147363	775640	49033	16379		1	0							2	3.9×10^4
35X-1, 145–150	270.48	171123	717895	20321	7018		Tr	0							0	U/D
37X-1, 0–4	278.82	190979	906506	34758	8407		0	0							0	U/D
38X-2, 0–5	287.93	155194	979326	50886	13315		1	0							1	5.7×10^4
39X-2, 0–5	296.63	208975	908710	56915	23235		1	0							1	4.6×10^4
40X-1, 0–5	304.03	201758	795865	9383	9230		0	0							0	U/D
41X-2, 0–5	314.33	116760	507611	25447	94796		4	3	5	6.7		2			21	5.7×10^3
42X-1, 147–150	323.09	163534	717869	37572	8466		Tr								0	U/D
43X-3, 0–5	333.43	150716	749949	16873	3878										0	U/D
44X-1, 9–14	339.42	175525	918771	18593	5739				1			1	1		4	U/D
45X-1, 0–5	348.23	20489	853129	41835	5529										0	U/D
47X-1, 65–75	366.80	123153	615195	10034	27688	0.3	1	Tr	Tr	Tr	Tr	Tr	Tr	Tr	1	1.0×10^4
48X-1, 47–49	375.48	173957	699399	25524	4346	Tr	Tr								0	U/D
49X-1, 0–5	383.93	176610	749105	17756	3875	Tr	Tr								0	U/D
50X-1, 0–5	392.83	140605	649341	17240	1070	Tr	Tr								0	U/D
52X-1, 21–26	410.74	161044	958588	6357	39090	Tr	2	2	1	3.7	2		1	2	13	3.5×10^3
55X-1, 35–40	437.38	173406	805778	40129	15686		1		1						2	3.9×10^4
56X-2, 0–5	447.33	171160	921846	36946	7946			2							2	U/D
57X-1, 48–53	455.21	203585	860335	33387	13596										0	U/D
58X-2, 27–32	465.30			32258	3403	Tr									0	U/D
Vacutainer:																
146-891B-																
41X-2, 98–99	315.29	109703	442017	58430	468343		150	61	3	28.0		5	1	1	249	389.5
42X-2, 50–50	323.60	198221	812857	6597	1312		1								1	6597
47X-2, 49–49	368.09	181257	691711	34502	87728	3.5	5	3							11	7325
55X-2, 107–108	368.68	209046	792808	197281	2579	3.5	2	3							9	82200

Note: C_X = *n*-alkanes, iC_X = iso-alkanes, nC_X = normal alkanes, $C_{X=}$ = unsaturated alkanes, $C_{2+} = (C_2 + C_3 + ... + C_6)$, U/D = $C_1/C_2 > 10^6$. Hydrocarbon gases given as ppmv; other gases are uncorrected for sample volumes. Tr = trace.

cantly less CH_4 and CO_2, and only ethane was registered. This, too, corresponds with the findings for the headspace sample at 323.09 mbsf.

Kerogen Analysis

The Geofina hydrocarbon meter pyrolysis returned low S_1 and S_2 counts (Table 7). This is consistent with the low organic carbon contents and indicates that the organic matter is refractory and reflects the terrigenous input. Examples of pyrolysis runs (Fig. 33) show the low hydrocarbon recovery and the impossibility of accurately estimating the T_{max} value.

Bitumen Analysis

Ten samples were extracted as described in the "Explanatory Notes" chapter (this volume). In no samples was there visible fluorescence, which indicates that the samples are of low rank and dominated by more refractory material. This conclusion agrees with the kerogen analyses.

High-resolution C_{11}–C_{40} gas chromatography of the hexane-soluble fraction revealed that a significant portion of the original labile hydrocarbons in the organic matter, such as the *n*-alkanes and isoprenes, had been lost, probably through biodegradation. Common normal- and cyclo-alkanes are the predominant compounds present.

The residual bitumen present is an unresolved complex mixture (UCM) of extractable material. Maturation of the organic matter has been insufficient to generate significant amounts of thermogenic products. Examples of typical C_{11}–C_{40} gas chromatograms in Figure 34 illustrate the highly degraded nature of the hydrocarbons in the extracts. The prominence of the UCM between the C_{17} and C_{23} compounds is typical for alteration products of marine microbial lipids (Simoneit, 1977, 1978). Some of the higher molecular weight com-

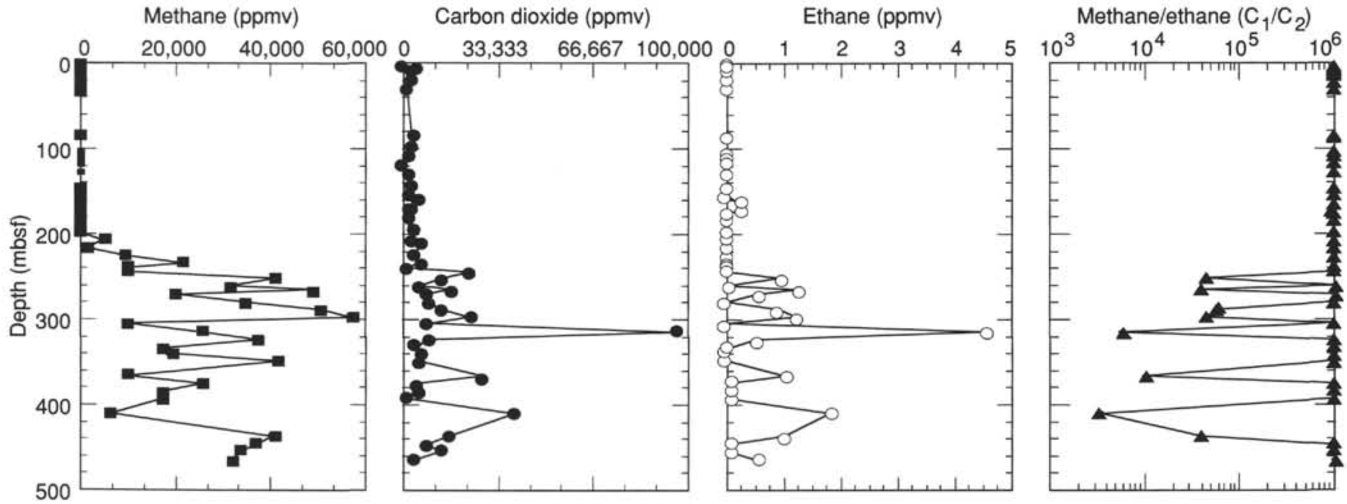

Figure 32. Depth distribution of total headspace methane, carbon dioxide, ethane, and methane/ethane at Site 891.

pounds ($>C_{24}$) could reflect the waxy, terrigenous input. The C_{37}–C_{39} alkenones (Fig. 35) were poorly resolved and determination of U^k37 (e.g., Volkman et al., 1980; Marlowe et al., 1984) was not made.

There is a pronounced odd-carbon predominance for the higher (C_{25+}) alkanes (Fig. 34), again showing the terrestrial and immature source influence.

Preliminary Interpretation

Bacterial Gases

Analogous to the Vancouver Island margin (Sites 888, 889, and 890), there are low hydrocarbon (methane) contents in the sulfate-reduction zone. Once the sulfate is exhausted at about 200 mbsf, the methanogens become more active and methane rises sharply with greater depth (see discussion in "Organic Geochemistry" sections of the "Site 888" and "Sites 889 and 890" chapters, this volume). This sulfate-methane segregation, illustrated in Figure 36, is typical of marine sediments (Claypool and Kaplan, 1974; Whiticar, in press). The primary pathway of methanogenesis in marine sediments is by means of CO_2 reduction as reported by Suess and Whiticar (1989). Good correlation also exists between the amount of headspace methane and the amount of organic carbon, as shown in Figure 37.

Methane transported upward by advection or diffusion into the sulfate-reduction zone (i.e., above 200 mbsf) is anaerobically consumed there, maintaining the low methane levels above 200 mbsf. Some minor methanogenesis can occur in the sulfate-reduction zone by noncompetitive substrates (Oremland et al., 1988; Zehnder, 1988), but this is quickly recycled by bacterial consumption.

Although confirmation by stable carbon isotope analysis is needed, bacterial methane is probably present down to the base of the hole at Site 891. It is uncertain if methanogenesis remains active down to the base of the hole, but microbial investigations should be able to resolve this.

Thermogenic Gases

The occurrence of autochthonous bacterial gases was expected at Site 891 based on typical diagenetic considerations, but the recovery of allochthonous thermogenic hydrocarbons could be anticipated only on the basis of the structural setting and possible communication with deeper seated units. Only trace amounts of higher hydrocarbon gases (e.g., C_2–C_6 homologs) can be formed diagenetically. The levels observed here are clearly the result of thermally stressed organic matter and not autochthonous generation. Further support for a thermogenic hydrocarbon contribution comes from the negative correlation between methane and the higher hydrocarbons as seen in Figure 36. The i-C_4/n-C_4 ratio of 0.75 at 314.33 mbsf supports a mature source for the gas. The minor amounts of ethene suggest that this thermal gas has been generated recently in geologic terms because olefins are not stable with time. Based on the kerogen and bitumen analyses (e.g., low pyrolysis yields and high carbon preference indices), the sediments cored at Site 891 are immature. The thermogenic hydrocarbons found at Site 891 cannot be indigenous and must have migrated into these shallower sediments. Figure 36 shows the restricted vertical extent of the thermogenic gas (ΣC_{2+}) in Hole 891B. The three most prominent incursions of thermogenic gas are at 314, 339, and 411 mbsf. These intervals also correspond to those where the petroliferous odor was most intense and where anomalous levels of CO_2 were recorded (Fig. 32). These gases are most likely brought up from greater depth, probably along faults (see "Structural Geology" section, this chapter). An analogous situation in the Bransfield Strait was reported by Whiticar and Suess (1987, 1989), where hydrothermally generated hydrocarbons were being transported by fluid flow into shallower sediments (that were similarly odorous).

The inverse correlation between methane and ΣC_{2+} seen in Figure 36 means that the invading gas is leaner in methane than the adjacent bacterial-methane dominated lithologies. Some limited vertical redistribution or a more pervasive gas incursion can account for the lower ΣC_{2+} levels observed between the major incursion zones. The maturity of the organic matter that has generated these gases, and a possible depth of maturation, can be ascertained by shore-based stable isotope measurements.

Table 7. Results of Geofina hydrocarbon meter pyrolysis at Site 891.

Sample	S_1 (mg C/g)	S_2 (mg C/g)	Calculated T_{max} (°C)	Measured T_{max} (°C)
146-891A-				
1H-2	0.08	0.10	344	411
146-891B-				
14X-1	0.02	0.03	429	512
21N-CC	0.12	0.13	396	472
25X-1	0.04	0.06	427	510
26X-1	0.03	0.06	419	500
29X-1	0.05	0.04	418	499
33X-1	0.18	0.24	404	482
38X-2	0.04	0.04	423	505
41X-1	0.07	0.05	417	498
47X-1	0.03	0.04	430	513
52X-1	0.02	0.02	430	513

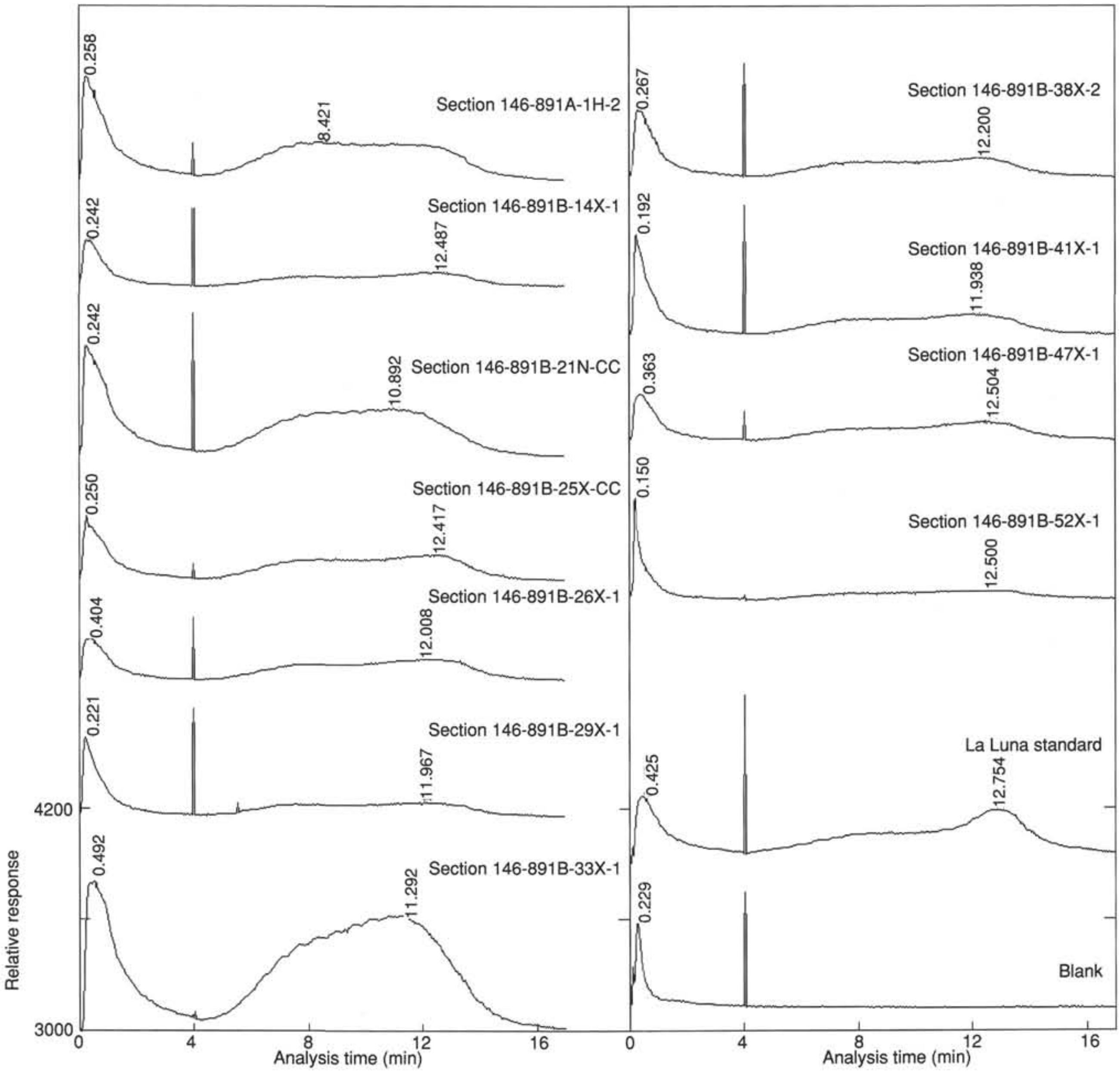

Figure 33. Examples of Geofina hydrocarbon meter pyrograms at Site 891.

INORGANIC GEOCHEMISTRY

Introduction

The purpose of interstitial-water analyses at Site 891 was to examine changes in fluid chemistry that may be associated with the frontal thrust and associated faults as well as other potentially permeable stratigraphic layers. Also of importance was finding evidence of carbonate cementation that may be reflected in changes in fluid composition and the determination of how this cementation may be related to fluid flow. The poor recovery made it difficult to relate the fluid profiles to representative stratigraphy or structure, but recovery was sufficient to delineate several anomalous geochemical intervals. Overall, the profiles appear somewhat "noisier" than the profiles from Sites 888, 889, and 890 (see "Site 888" and "Sites 889 and 890" chapters, this volume), which may reflect more active fluid flow or greater lithologic variability in the Oregon margin.

The most important results of the interstitial-water analyses are (1) the striking difference between the chemical profiles of Hole 891A and the top of Hole 891B, and the lack of steady-state profiles between the pore fluids recovered from Hole 891A and the presumed values for bottom seawater at this site; (2) the occurrence of major breaks in the chemical profiles at about 200, 300–320, and 440 mbsf, which may correlate with advecting fluids or boundaries between fluid regimes; and (3) the indication of two types of fluids infiltrating the section: type I pore fluid, which has moderately high chlorinity (relative to bottom seawater at Site 891) and low calcium concentrations, and type II pore fluid, which is characterized by low chlorinity and possibly low sodium concentrations and high calcium and lithium concentrations. Type I fluids are found in Hole 891A and at about 200 and 240–265 mbsf in Hole 891, whereas type II fluid infiltrates the section where deep breaks in the profiles occur at 300 and 440 mbsf (Fig. 38). Both types of fluids appear to have high silica concentrations.

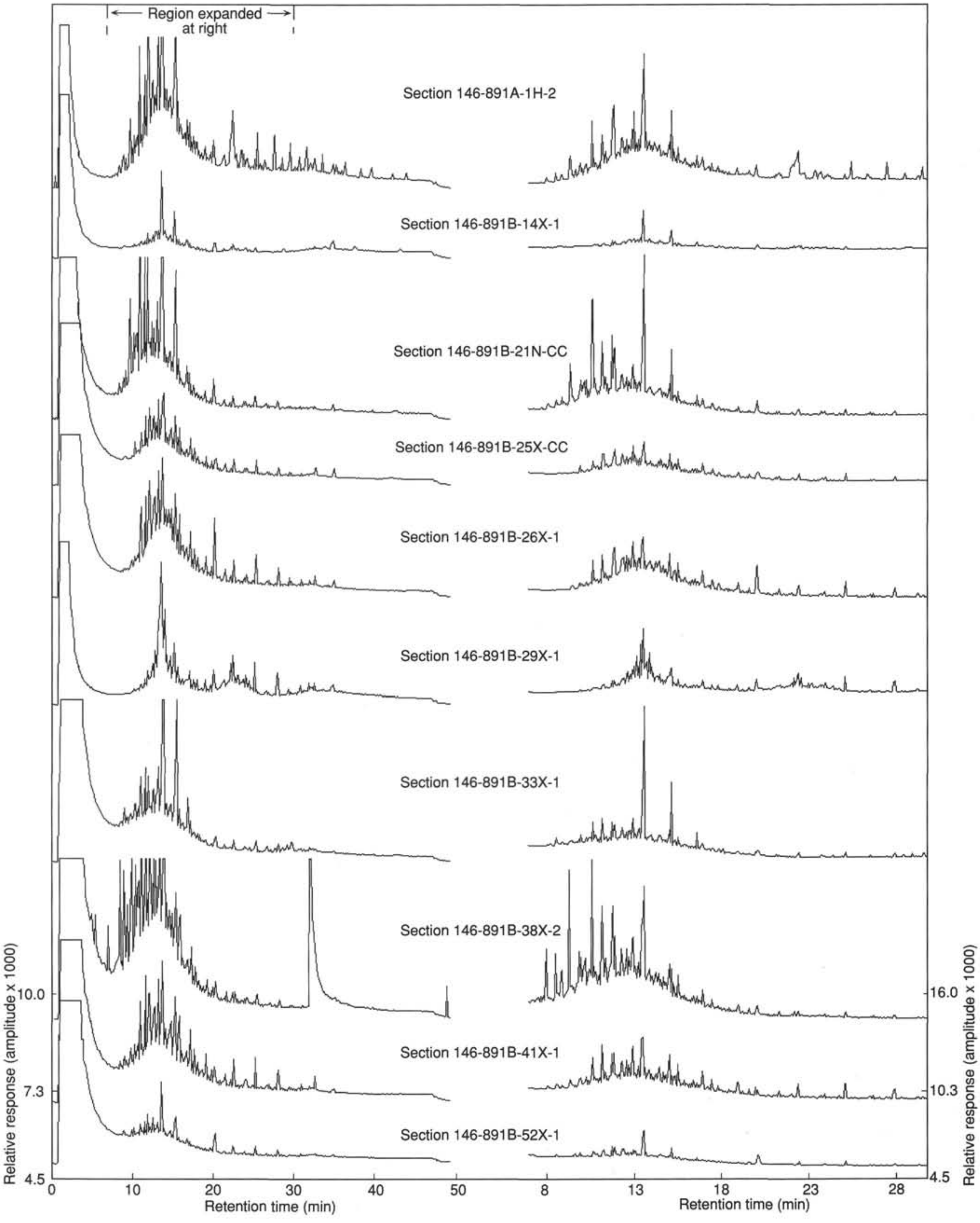

Figure 34. Examples of typical C_{11}–C_{40} gas chromatograms at Site 891. The set of chromatograms to the right are an enlargement of the 1- to 35-min interval (relative retention time).

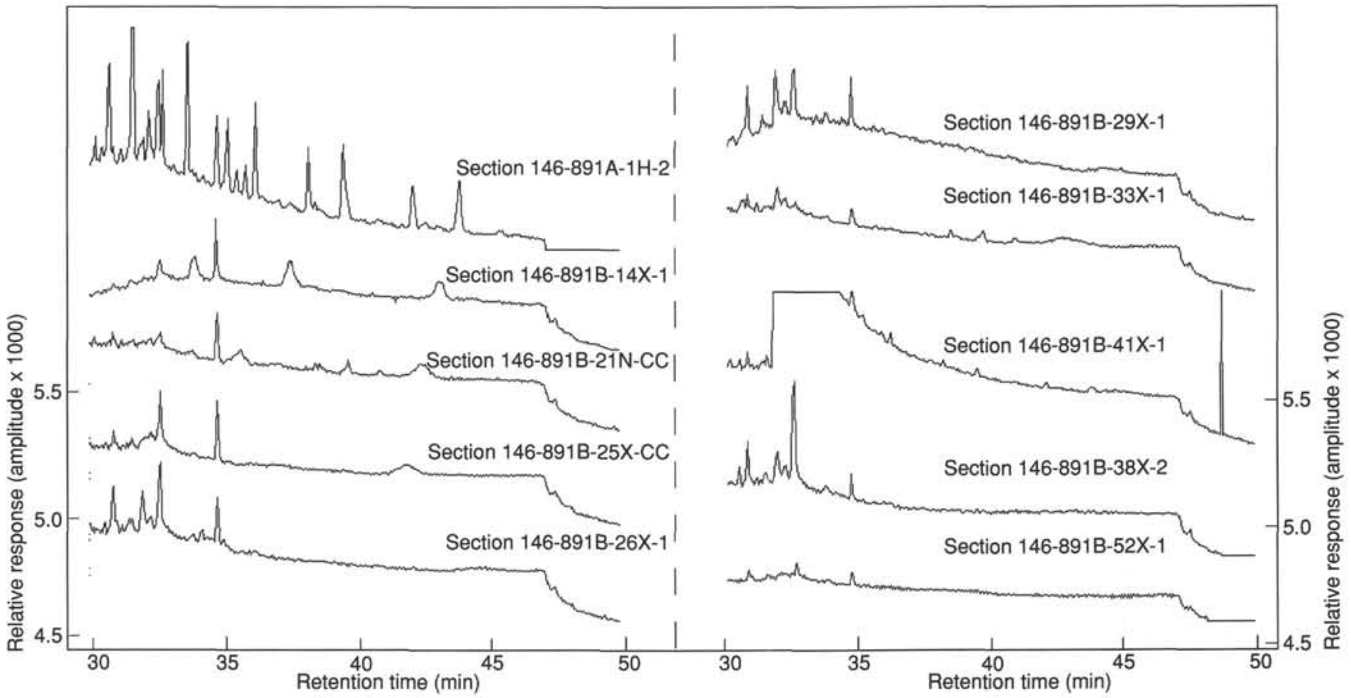

Figure 35. Examples of typical C_{23}–C_{40} gas chromatograms ("alkenone fraction") at Site 891. The full chromatograms are given in Figure 34.

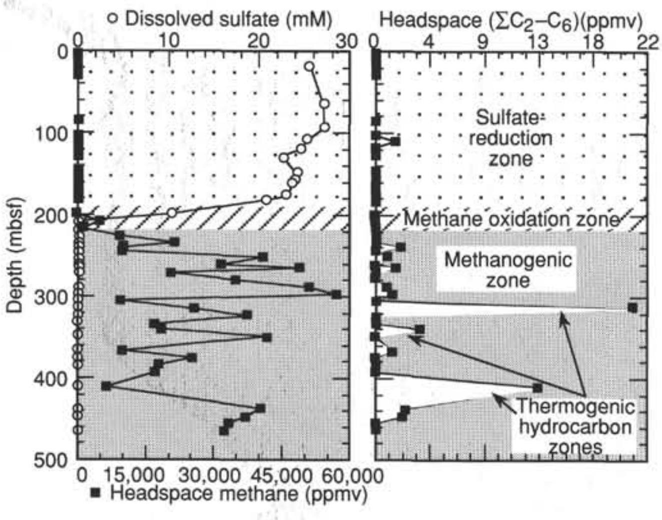

Figure 36. Interpretative diagram of sulfate, headspace methane, and total higher hydrocarbons (ΣC_{2+}) at Site 891. The zones of sulfate reduction, anaerobic methane oxidation, methanogenesis, and thermogenic hydrocarbon incursions are shown.

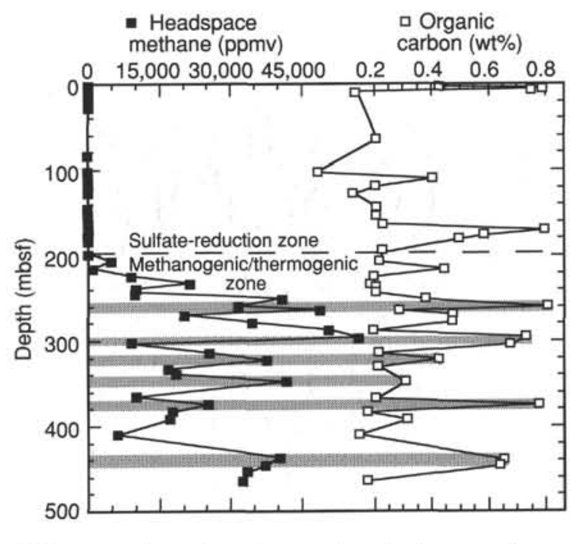

Figure 37. Correspondence of headspace methane (methanogenesis) to organic carbon at Site 891.

Most of the chemical profiles can be divided into one of two categories based on gross changes in downhole concentrations (Fig. 38). Chloride, sodium, ammonia, lithium, and silica concentrations, alkalinity, and Mg/Ca ratios *generally* have higher values deeper in the section, whereas sulfate, magnesium, calcium, and potassium concentrations *generally* show lower values in deeper portions of the section. Nearly all profiles show variations from these trends, and the abrupt changes in concentrations may be related to diagenetic processes, fluid advection, or both. For example, the sharp decrease in calcium concentrations at about 200 mbsf corresponds to an abrupt increase in alkalinity and may reflect increased carbonate precipitation (Fig. 38).

Sediment samples generally were processed in the manner described in the "Explanatory Notes" chapter (this volume). Because recovery in many cores was low, in some cases only small samples could be squeezed or material from the core catcher was used. Because of the smaller sediment samples and the necessity in many cases to discard much of the chosen whole-round sample before squeezing owing to contamination by drilling water, fluid recovery was low in some cores and a full suite of analyses could not be performed. Chloride, magnesium, calcium, potassium, lithium, silica, ammonium, and sulfate were given higher priority, whereas phosphate and alkalinity were analyzed only when sufficient pore water was available. Corrections for drilling-water contamination were made below 199 mbsf by using sulfate concentrations as a gauge of

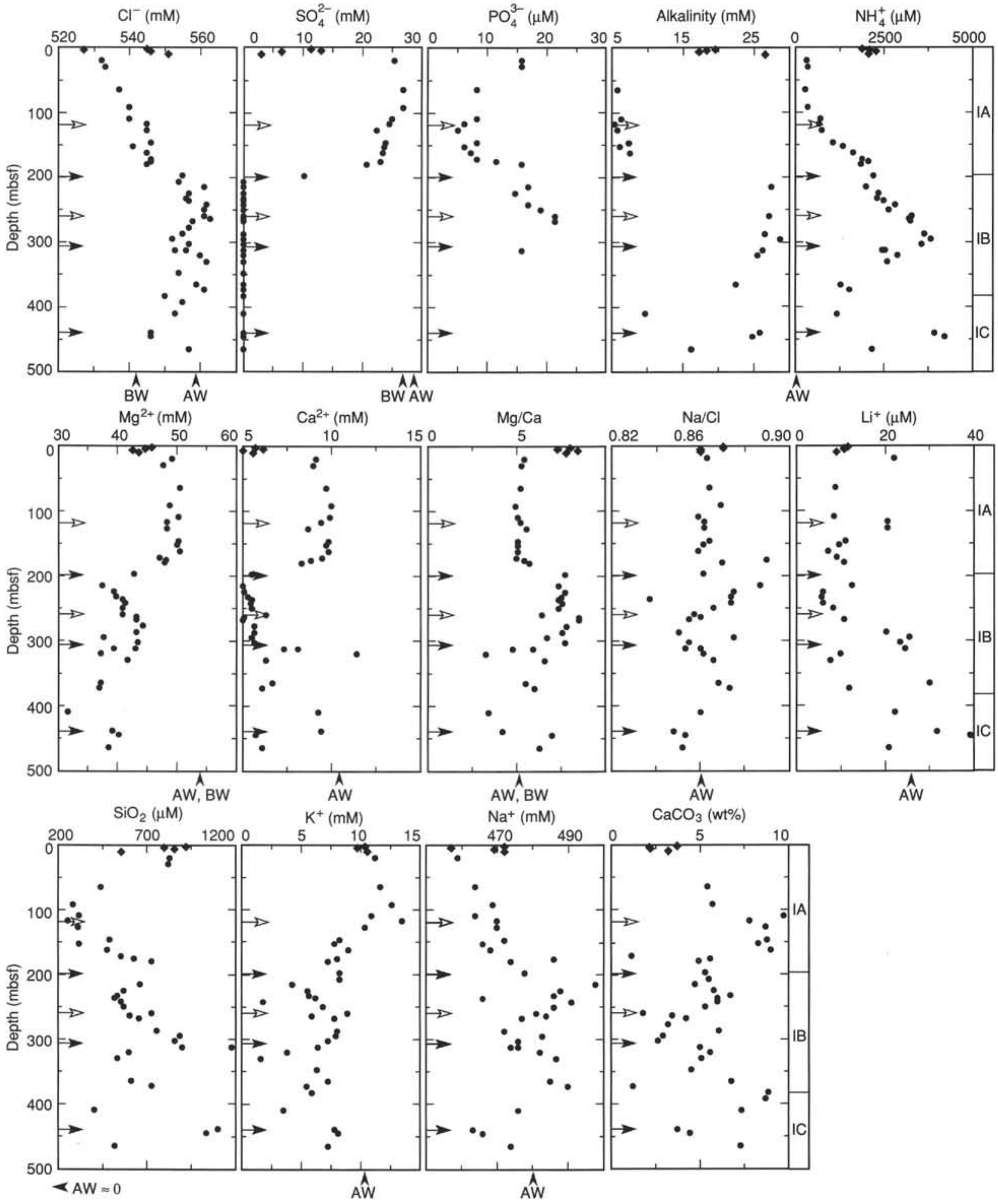

Figure 38. Concentration profiles of inorganic species analyzed vs. depth at Site 891. Lithostratigraphic unit designations shown on right. Solid arrows are zones of major chemical anomalies (chemical horizons); open arrows are zones of minor anomalies. Diamonds are data from Hole 891A, filled circles from Hole 891B. Bottom seawater (BW) and average seawater (AW) according to IAPSO standard are shown. Sulfate profile below 199 mbsf was corrected to zero to remove drilling-water contamination, because the presence of methane below this depth is incompatible with sulfate (see "Organic Geochemistry" section, this chapter). A corresponding correction was applied to the other chemical profiles below 199 mbsf (Table 7). Carbonate content of the sediments has been plotted for comparison.

Table 8. Interstitial-water chemical data, Holes 891A and 891B.

Core, section, interval (cm)	Depth (mbsf)	Water (mL)	pH	Alkalinity (mM)	Salinity (g/kg)	Cl^- (mM)	Mg^{2+} (mM)	Ca^{2+} (mM)	Mg/Ca	SO_4^{2-} (mM)	Corrected SO_4^{2-} (mM)[a]	PO_4^{3-} (µM)	NH_4^+ (µM)	SiO_2 (µM)	K^+ (mM)	Na^+ (mM)	Na/Cl	Li^+ (µM)
146-891A-																		
1H-2, 140–150	2.90	40	7.9	19.58	33.0	545	45.72	5.70	8.00	11.16	11.16	97.4	1870	917	10.38	472.0	0.87	11.6
1H -3, 103–113	4.03	32	7.8	18.34	34.0	527	44.77	6.17	7.30	13.00	13.00	86.6	2087	795	9.67	457.0	0.87	10.6
2H-1, 109–119	5.79	30	7.9	17.16	33.0	546	42.55	5.04	8.40	6.22	6.22	89.8	2260	857		469.0[b]	0.86	10.7
3H-2, 53–68	9.27	30	8.0	26.63	34.0	551	43.59	5.59	7.80	2.76	2.76	90.9	2071	554	10.59	472.0	0.86	9.1
146-891B-																		
3X-CC	20.80	5.0			34.5	532	49.40	9.14	5.40	25.62	25.62	15.9	297	828	11.25	459.0[b]	0.86	22.0
4X-CC, 0–5	29.60	5.0			34.0	533	47.85	9.02	5.30			15.9	333	823				
8X-1, 15–20	65.35	8.5	8.3	5.77	34.5	537	50.60	9.71	5.20	27.04	27.04	8.3	282	444	11.71	464.0	0.86	8.7
11X-2, 16–21	92.30	7.5			35.0	540	48.90	9.97	4.90	27.12	27.12		360	284	12.63	469.0	0.87	
14X-1, 54–64	110.04	15.0	8.3	6.32	35.0	540	50.50	9.90	5.10	25.16	25.16	8.3	690	320	11.00	464.0	0.86	8.4
15X-1, 82–90	119.22	9.0	8.3	5.50	34.5	545	48.55	9.39	5.20	24.70	24.70	6.2	677	253	13.56	470.0	0.86	20.5
16X-1, 57–67	127.87	10.0	8.3	5.79	34.5	545	48.47	8.73	5.60	22.47	22.47	5.1	744	310	10.44	470.0	0.86	20.7
18X-CC, 26–37	148.36	15.0	8.2	7.39	34.5	546	50.50	9.83	5.10	24.04	24.04	8.3	1077	494	8.24	472.0	0.86	11.1
19X-1, 0–10	153.90	12.0	8.1	6.20	34.5	541	50.10	9.74	5.10	23.94	23.94	6.2	1362	317	7.78	466.0	0.86	9.6
20X-1, 28–38	162.98	11.0	8.0	7.57	35.2	545	50.71	9.85	5.10	23.54	23.54	7.2	1628	478	9.00	468.0	0.86	7.2
21N-CC, 0–5	172.12	5.0			34.2	546	47.19	9.52	5.00			8.3	1895	554				9.0
22X-1, 55–67	176.65	4.0			34.5	546	48.21	8.86	5.40	23.14	23.14	11.6	2086	629	8.03	486.0[b]	0.89	
23X-1, 50–60	181.10	3.5			34.5	545	48.01	8.38	5.70	20.88	20.88	15.9	1853	732	7.32	474.0[b]	0.87	10.8
25X-CC, 13–20	198.94	4.0			35.0	555	42.88	5.58	7.70	10.20	10.20		2224		8.24	478.0[b]	0.86	
26X-1, 42–46	207.52	2.5				554				0.04	0.00				8.29			
27X-1, 15–25	216.05	8.0	8.0	27.54	34.0	561	37.37	5.05	7.40	1.92	0.00	18.3	1988	661	4.25	498.0	0.89	11.6
28X-1, 32–50	225.02	6.0			32.5	557	39.40	5.12	7.70	1.62	0.00	15.7	2372	567	5.52	488.0[b]	0.88	4.8
29X-1, 22–29	233.82	32.5				556	39.86	5.32	7.50	0.89	0.00		2314	535	5.63	486.0[b]	0.87	4.9
30X-1, 75–83	238.35				32.5	557	40.85	5.53	7.40	0.42	0.00		2516	523	6.24	466.0[b]	0.84	
31X-1, 135–150	243.75	3.5			32.5	562	41.34	5.46	7.60	2.88	0.00	19.0	2818	555	1.84	491.0[b]	0.87	3.4
32X-1, 11–17	251.51	3.0			32.5	561	40.82	5.54	7.40	0.87	0.00	19.8	2657	569	6.91	486.0[b]	0.87	7.5
33X-1, 0–17	260.20	8.0	8.0	27.23	33.0	561	41.02	6.37	6.40	0.04	0.00	21.4	3300	728	8.90	481.0	0.86	
34X-1, 100–115	264.10	3.5			34.0	563	43.25	5.09	8.50	1.53	0.00		3218	608	5.88	484.0[b]	0.86	
35X-1, 16–28	269.16	5.0			33.5	558	43.38	5.08	8.50	1.21	0.00	22.4	3239	659	7.88	477.0[b]	0.86	10.0
36P-1, 0–6	277.80	2.0				557	44.38	5.68	7.80									
38X-2, 0–18	287.87	13.0	8.0	26.73	33.5	555	43.25	5.70	7.60	0.13	0.00		3654	759	8.08	472.0	0.85	20.4
39X-1, 101–118	296.11	16.0	7.8	28.85	33.5	552	37.60	5.58	6.70	0.15	0.00		3838	885	7.93	48.0	0.87	25.5
40X-1, 0–11	304.00	9.0			33.5	557	43.46	5.66	7.70	0.68	0.00		3578	860	7.32	476.0[b]	0.85	23.3
41X-1, 110–135	314.10		7.7	26.29	34.0	556	43.04	7.34	5.90				2452	904		474.0[b]	0.85	
41X-1, 135–150	314.15	9.0				553	39.33	8.14	4.80	1.05	0.00	16.5	2551	1180	6.45	476.0[b]	0.86	24.5
42X-1, 0–18	321.60		8.0	25.49	33.5	560	37.33	11.41	3.30	1.70	0.00		2897	596	3.89	482.0	0.86	8.8
43X-1, 10–27	330.50	6.0			33.0	562	41.77	6.31	6.60	3.12	0.00		2613	533	1.56	487.0[b]	0.87	5.3
45X-1, 6–14	348.26	1.5			32.5	554			0.18	0.00					6.29			
47X-1, 95–110	367.05		7.9	22.58	33.5	559	37.29	6.72	5.50	0.00	0.00		1277	613	7.26	485.0	0.87	30.2
48X-1, 0–15	375.00	5.0			34.5	561	36.98	6.13	6.00	0.80	0.00		1515	730	5.42	490.0[b]	0.87	11.5
49X-1, 23–29	384.13				32.0	550			0.00	0.00					5.93			
50X-1, 17–20	392.97	2.5			32.5	555												
52X-1, 7–21	410.57	9.0	8.0	9.79	31.5	553	31.72	9.27	3.40	1.68	0.00		1186	404	3.48	476.0	0.86	22.2
55X-2, 130–150	438.97	20.0	7.7	25.92	33.0	546	39.28	9.41	4.20	0.00	0.00		3944	1099	7.78	463.0	0.85	31.9
56X-1, 72–89	446.52	28.0	7.7	24.92	34.5	546	40.35	5.78	7.00	0.23	0.00		4223	1035	8.18	466.0	0.85	39.3
58X-2, 15–27	464.60	17.0	8.1	16.30	32.5	557	38.64	6.14	6.30	0.44	0.00		2179	521	7.32	474.0	0.85	20.8

[a] Corrected for contamination by drilling water; the percent sulfate contamination used for the correction of other species.
[b] Concentration of one major ion was estimated by extrapolation before calculation of the Na concentration.

contamination and known concentrations of the various species in seawater. Below this depth the presence of abundant methane (see "Organic Geochemistry" section, this chapter) implies that any sulfate present must be from contamination, because methane is consumed by the sulfate-reducing bacteria in the sulfate-reduction zone (Claypool and Kaplan, 1974). Above 199 mbsf, however, sulfate could not be used as a gauge of drilling-water contamination, and none of the other constituents analyzed on board uniquely define drilling-water contamination, so these values could not be corrected. Sodium concentrations were calculated based on charge balance with the major species measured (Table 8).

The water sampling temperature probe (WSTP) was not deployed for the recovery of pore fluids, and the pressure core sampler was deployed once at 277.8 mbsf. The PCS sample arrived on deck at only 50% of the calculated hydrostatic pressure at depth, and the pressure chamber contained mostly water. The 6 cm of sediment recovered was squeezed and the fluids analyzed (Table 8).

Depth Profiles of Chemical Data

The three main chemical intervals are discussed individually in the following, and then the character of the profiles between the intervals is discussed briefly.

Chemical Horizon I (200 mbsf)

Most of the chemical profiles indicate that significant changes occur at 200 mbsf (Fig. 38). Sulfate decreases to zero concentration, which correlates well with the onset of methane accumulation (see "Organic Geochemistry" section, this chapter). A break in slope in the ammonium profile spans this depth and suggests a small repetition of the profile with increasing depth, perhaps related to fracturing.

The largest break in the chloride profile occurs at 200 mbsf. The increase is approximately 10 mM over a maximum vertical distance of 18 m. The average value of chlorinity in the high-chloride zone (200–300 mbsf) is 557 mM, which is higher than that of local bottom water (541 mM), but lower than average seawater (IAPSO = 559 mM). The chlorinity profile above and below 200 mbsf is relatively smooth, but the sharp step at 200 mbsf suggests that the profile has been disrupted recently. The style of the break in chlorinity is not that of a maximum; rather the concentrations remain at relatively high values below 200 mbsf. This pattern suggests that the fluid regime below 200 mbsf is relatively similar over a broad range in terms of chlorinity, although significant variations are present in the relatively higher concentrations.

The silica profile appears to trend toward a sharp maximum in concentration at 200 mbsf, which is not well defined because of locally poor fluid recovery. Nevertheless, at this depth the sharp increase in silica does appear to correlate with the increase in chlorinity, making the pore fluid at this horizon a type I fluid.

Magnesium and calcium show dramatic decreases at 200 mbsf, which suggest active precipitation of diagenetic carbonate. Calcium concentrations remain low down to about 314 mbsf, the same interval over which alkalinity is high, which is consistent with patterns expected for carbonate formation. The large increase in the Mg/Ca ratio at 200 mbsf is attributable to much lower initial concentrations of calcium than magnesium above this depth, so that removal of equal proportions of the two constituents from pore fluids during carbonate formation would result in a much greater proportional decrease in calcium. Although the calcium, magnesium, and alkalinity profiles suggest carbonate precipitation, carbonate contents are not exceedingly high at about 200 mbsf and show no obvious changes spanning this depth. The resistivity and velocity logs have maxima at about 190 mbsf that might indicate carbonate cementation, but the patterns in the logs are also consistent with a compacted clay layer (see "Downhole Logging" section, this chapter). The reduction of calcium and magnesium concentrations in the pore waters at this chemical interval may reflect a depletion related to carbonate precipitation elsewhere as the pore fluids migrated to their current position.

Chemical changes at 200 mbsf also correlate with an increase in porosity and fracturing (see "Physical Properties" and "Structural Geology" sections, this chapter). The pore-water geochemistry is consistent with flow at this depth of high-chloride, high-silica fluid into the system. High-chloride fluids are not typically associated with accretionary wedges in which flow is thought to be active. The chloride signature of deeper fluids is typically thought to be lower than that of seawater owing to dilution by fresh fluids that have been derived from processes such as clay dehydration reactions or clay membrane filtration. One exception to this general pattern is the Peru Margin, where high-chlorinity fluids recognized on the shelf were attributed to the subsurface flow of brines (Suess, von Huene, et al., 1988). The setting at the Oregon Margin, however, precludes this possibility because the region of the frontal thrust is not connected with present or paleodepositional settings where evaporites are most likely to be found. Possible sources of high-chloride fluids at Site 891 are (1) fluids derived laterally or vertically from areas of extensive hydration reactions involving volcanic matter, where temperatures are sufficient for these reactions to proceed (in addition, hydration reactions usually produce higher silica); (2) relic seawater with higher chloride concentrations than today's bottom water, perhaps related to the Pleistocene glacial periods; or (3) a combination of these two sources. Further studies of other constituents, including oxygen and strontium isotopes, may shed more light on whether the disruptions in chlorinity are the result of the influx of fluids or local processes.

Chemical Horizon II (300–320 mbsf)

Many of the chemical profiles show significant changes at about 300–320 mbsf that suggest this is an important horizon in terms of fluid flow (Fig. 38). Most of the fluid profiles are more variable below this interval, which may reflect a greater degree of structural disruption and perhaps fluid flow. Chlorinity shows a minimum centered at about 300 mbsf, which is complicated somewhat by a single relatively higher value, but otherwise is well defined by eight measurements. Silica and calcium both increase significantly at about 300 mbsf. Magnesium does not change significantly, and consequently the Mg/Ca ratio decreases considerably at greater depths. Lithium concentrations show a series of high values that span the 300 mbsf interval from 280 to 320 mbsf, with concentrations more than twice as high as those of samples analyzed from above or below. The pore fluid at this interval is therefore high in lithium, silica, ammonium, and calcium and has relatively lower chloride.

Chemical Horizon III (370–390 mbsf)

The interval 370–390 mbsf is examined because it corresponds to the approximate expected depth of the frontal thrust at Site 891. Few anomalies were observed in the chemical profiles at this depth, with the exception of a small maximum in chlorinity, a high concentration of silica, and perhaps maxima in the sodium and Na/Cl profiles (Fig. 38). The observed chlorinity profile is most consistent with a type I fluid, although the calcium profile does not show any anomaly. The general lack of chemical anomalies suggests that the frontal thrust may be an interval of little or no fluid flow.

Chemical Horizon IV (440–447 mbsf)

Deeper in the section, interpretation of the profiles is more difficult because of fewer data points, but the interval 440–447 mbsf shows significant changes in many of the measured components (Fig. 38). The first observation of change at this interval was that whole-round Sample 146-891B-55X-2, 130–150 cm, yielded 20 mL of fluid, which is more typical of yields acquired at much shallower depths (Table 8). Porosities measured in the cores are much higher below this interval than above (see "Physical Properties" section, this chapter). Alkalinity, magnesium, Mg/Ca ratio, ammonium, silica, potassium, and lithium all show substantial increases over the interval from 440 to 447 mbsf, whereas chloride, calcium, and sodium concentrations decrease significantly. The high-silica, low-chloride pore fluids measured in this horizon have characteristics similar to those of the pore fluid observed at 300–320 mbsf. Furthermore, high C_1 and C_2 hydrocarbon concentrations were observed at both of the intervals that contain type II fluids (see "Organic Geochemistry" section, this chapter). The higher hydrocarbons indicate a deeper, thermogenic source, and because these hydrocarbons are associated with high-calcium, low-chloride fluids, it follows that the deeply derived fluid is also characterized as low in chloride and high in calcium and lithium concentrations. This geochemical signature contrasts with the type I fluids observed at 200 mbsf, which are higher in chloride and lower in calcium concentration.

Based on the observed chemical profiles at the major anomalous intervals, it appears that at least two fluid sources are necessary to explain the pore-water chemistry. Type I fluids could be derived from hydration reactions, which would drive up chloride concentrations by removing pure water from the pore fluids. Type II fluids could be derived from clay transformation and dehydration reactions, which would release fresh water and calcium ions. The onset of hydration reactions typically occurs at lower temperatures, and thus shallower depths, than clay dehydration reactions. This fact suggests that type I fluids are derived from shallower depth intervals than type II fluids and is consistent with the observation that type II fluids are found at the deeper anomalous geochemical intervals. Both inferred reactions would release silica, which would explain the silica maxima associated with both type I and type II fluids.

Other Aspects of the Fluid Profiles

The interval between 0 and 10 mbsf was cored with high recovery in Hole 891A, and nearly every chemical parameter measured had significantly different concentrations than those measured in the shallowest portion of Hole 891B. Furthermore, most species in Hole 891A have concentrations that are different from values for overlying seawater, indicating that diffusive exchange between pore water in the upper 10 m of the sediment and bottom seawater is *not* the dominant process at Hole 891A (local bottom water was collected at the site by the Scripps Institute of Oceanography vessel *New Horizon*). Chloride, phosphate, sodium, and ammonium concentrations, alkalinity, and Mg/Ca ratios are all significantly higher in Hole 891A than in either average seawater or pore waters in the upper portion of Hole 891B, whereas magnesium, calcium, and sulfate are all substantially lower (Fig. 38). The concentrations of these species in Hole 891A are more similar to parts of the chemical profiles from Hole 891B well below the surface and suggest a minimum depth of origin of 200 mbsf. All of the concentrations of measured species from Hole 891A show a range in values that may indicate the mixing of more deeply derived type I fluid with seawater. These unusual chemical profiles imply that Hole 891A may have penetrated a fluid conduit.

The chloride concentration profile above 200 mbsf in Hole 891B superficially resembles a diffusion curve between high-chloride fluids below 200 mbsf and low-chloride fluid near the seafloor, but the top of the profile does not trend toward the present bottom-water value of 541 mM, and the bottom of the profile shows no exponential approach to concentrations in deeper pore fluids. The mismatch is difficult to explain because chloride diffusion should be rapid, and a steady-state profile between bottom-water and shallow pore waters should be quickly established, if diffusion is the dominant process. The near-surface chlorinity profile suggests, however, that advection of a low-chlorinity type II fluid occurs above a depth of 20.8 mbsf at Hole 891B. This observation is in contrast to the type I fluid measured at Hole 891A, only 20 m away, and suggests that a complicated circulation system exists. The exact depth of the shallow aquifer at Hole 891B could not be determined because suitable samples were not obtained above 20.8 mbsf.

Another interesting interval in the fluid profiles occurs between 119 and 128 mbsf, where small changes are observed in nearly all constituents. The most prominent features of this depth are an abrupt 5-mM increase in chlorinity, an increase in the Mg/Ca ratio, a large increase in lithium concentration, and sharp decreases in calcium and sulfate concentrations (Fig. 38). Magnesium shows a minor decreased concentration as well, and the coupled decreases in calcium and magnesium suggest that precipitation of dolomite or magnesian calcite occurs at this level. There is no correlative increase in alkalinity to enhance carbonate precipitation at this depth (Fig. 38), but the highest concentration of carbonate (9%) was measured in this interval (Sample 146-891B-20X-1, 28–38 cm; see "Organic Geochemistry" section, this chapter). The increase in lithium might suggest the dissolution of volcanic glass, but the lack of a silica anomaly and the decrease of the calcium concentration are not consistent with this inference. Fluid flow might account for the small anomalies if the fluid were enriched in chloride and lithium and were depleted in calcium, magnesium, and sulfate. High-chloride concentrations coupled with low-calcium concentrations would be an unusual composition for fluids derived from depth if they were related to clay mineral transformations, however, and no structures or lithologies suggestive of high permeability were recognized at this depth. Because recovery was low, insufficient physical property data were collected to resolve any significant changes in this interval.

The chemical profiles between 200 and 300 mbsf can be interpreted in a number of ways, in part because some of the relative changes are small and the data are variable. Overall, chloride concentrations are significantly higher than those of pore water higher in the hole and of local bottom water, but the average chloride concentration (557 mM) is not high compared with that of average seawater (559 mM). A small chlorinity minimum occurs at 234 mbsf and correlates with broad lows in silica and lithium concentrations. Apparent chloride maxima occur at 250–260 mbsf and possibly at 216 mbsf. Although the gross character of fluid in the entire interval is that of moderately high chlorinity, the local maxima and the single local minimum suggest the input of two fluids, one with chloride concentrations above and one below background levels. The low-chlorinity fluid at 234 mbsf differs from type II fluid, however, in that the silica concentrations are at a minimum at this depth. The high-chlorinity fluid at 250–260 mbsf corresponds to a fault zone recognized in the core, a local maximum in measured headspace C_2 hydrocarbon concentrations, and significant changes in physical properties (see "Structural Geology," "Organic Geochemistry," and "Physical Properties" sections, this chapter). Calcium and magnesium concentrations show small increases and silica shows a prominent spike at 250–260 mbsf; the chemical information coupled with structural observations suggest the flow of type I fluid along a fault zone at this interval.

Below 322 mbsf, the geochemical data are sparser, in large part because of the poor recovery of suitable samples for squeezing. A maximum in carbonate concentration and a high value of silica concentration occur at about 380 mbsf, but no other clear chemical anomalies occur at the presumed depth of the frontal thrust (see "Seismic Stratigraphy" section, this chapter).

Conclusions

Chloride concentrations increase with depth to values below 200 mbsf that are slightly higher than that of average seawater. Fluid anomalies in Hole 891A and at 200 and 260 mbsf in Hole 891B tend to be relatively higher in chlorinity than background pore fluids. High-chlorinity fluids could develop from hydration reactions or from relict seawater that was trapped in pore spaces from a time when seawater had a higher chlorinity than the current bottom water. The major deep-fluid anomalies at 300 and 440 mbsf and a possible anomaly at the top of Hole 891B suggest that fluids injected at these levels are consistently low in chlorinity, high in silica concentrations, and perhaps high in calcium concentrations. The two deepest anomalies also correspond with major changes in physical properties and maxima in hydrocarbon concentrations. Fluids low in chloride and high in silica and calcium are consistent with derivation from clay dehydration reactions.

The fluid profiles in Hole 891A and the shallow portion of Hole 891B are radically different, even though the holes are separated by 20 m. The chemical characteristics of Hole 891A are consistent with the derivation of fluids from about 200 mbsf.

PHYSICAL PROPERTIES

Introduction

Sediment physical properties were measured on cores recovered from Holes 891A and 891B. Sample recovery was low and is reflected in the sparse data sets. Measurements for Site 891 include index properties, electrical resistivity, acoustic velocity, shear strength, and thermal conductivity. The methods used for these measurements are described in the "Explanatory Notes" chapter (this volume). The MST was run on all cores for magnetic susceptibility (see "Paleomagnetism" section, this chapter). The gamma-ray attenuation porosity evaluator (GRAPE) and acoustic velocity on the MST were turned off during the MST runs because of the poor sample quality.

Physical properties show distinct offsets at discrete depth intervals that may indicate the positions of faults or compositional changes. Five major discontinuities are described in this section. The physical property data are internally consistent and suggest an overconsolidated sediment column in the upper 260 mbsf, a normal to slightly underconsolidated interval from 260 to 439 mbsf, and a significantly underconsolidated section below 439 mbsf.

Index Properties

In lithostratigraphic Subunit IA (0–198.2 mbsf), the bulk density increases and the porosity and water content decrease with depth (Fig. 39 and Table 9), suggesting that the dominant process in this interval is gravitational compaction. Below 200 mbsf, the index properties do not vary consistently with depth. Instead, the index properties show several large offsets spaced approximately 50–70 m apart in depth.

Five discontinuities in the index-properties distribution with depth occur between 200 mbsf and the bottom of the hole (Fig. 40). These discontinuities could be the result of faulting and/or compositional changes in the sediment column. The shallowest offset in index properties, below 200 mbsf, occurs close to the Subunit IA/IB bound-

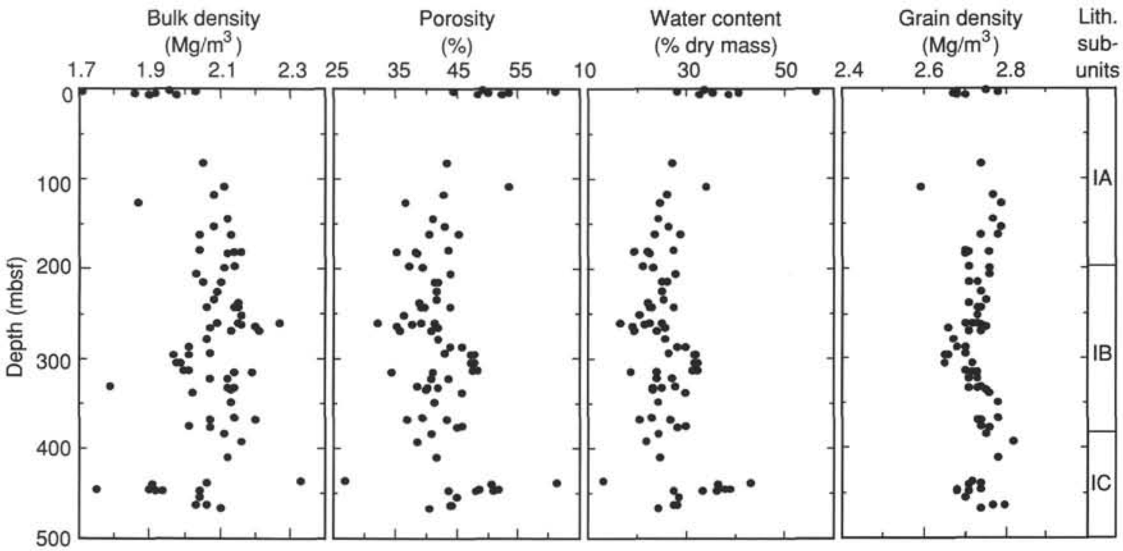

Figure 39. Index properties (bulk density, porosity, water content, and grain density) vs. depth for lithostratigraphic Subunits IA, IB, and IC at Site 891.

ary and is defined by an increase in porosity from 37% to 44% corresponding to a decrease in bulk density from 2.14 to 2.03 Mg/m^3. The second offset occurs approximately 60 m below the Subunit IA/IB boundary at 261 mbsf, where porosity increases from 32% to 38%. Between the first and second index-properties offsets, porosity decreases steeply with depth (44% at 207 mbsf, 32% at 261 mbsf). Below the second offset, porosity anomalously increases with depth (32% at 261 mbsf, 48% at 315 mbsf).

The third and fourth discontinuities are not as pronounced as the others. The third offset (315 mbsf) occurs 54 m below the second and is seen as a drop in porosity (increase in bulk density) from about 48% to 41%. The fourth discontinuity occurs at 368 mbsf (53 m below the third offset), where the porosity increases from 37% to 45%. There are no consistent trends in index properties with depth within these intervals.

The largest offset was observed at 439 mbsf, where the porosity increases to 61%. The precise position of this offset is not well defined because no samples were recovered between 412 and 437 mbsf. Below 439 mbsf, porosity decreases steeply with depth (61% at 439 mbsf, 41% at 467 mbsf).

These index property discontinuities can be grouped into two types, drained and sealed. Sealed boundaries are characterized by offsets from low to high porosity passing downhole (e.g., the fifth offset, at 439 mbsf), whereas drained boundaries are characterized by increasing porosity with distance away from the offset (e.g., the second offset, at 261 mbsf).

In comparison with normally consolidated porosity-depth functions for clayey silt and silty clay (Brückmann, 1989), the porosity-depth distribution from Site 891 shows three general regions of stress history. In the upper 280 mbsf, porosity generally lies below the normally consolidated functions (Fig. 40), suggesting overconsolidation. Between 280 and 370 mbsf, porosity is generally close to or slightly below the predicted values for normally consolidated clayey silt and silty clay, suggesting normal to slight underconsolidation. Below 439 mbsf, the porosity is higher than both of the normally consolidated prediction curves, suggesting a significantly underconsolidated section.

Electrical Resistivity

Resistivity was measured in selected samples that were relatively undisturbed in Holes 891A and 891B. Electrical resistivity is reported here in its nondimensional form as the ratio of saturated sediment resistivity to pore-fluid resistivity (taken as that of seawater), or the formation factor. A log-linear function of sediment porosity and formation factor, as proposed by Archie (1942) and Lovell (1985), was fitted to the data. To estimate the Archie coefficients (see "Explanatory Notes" chapter, this volume), formation factor values versus sediment porosity data were plotted (Fig. 41 and the best exponential fit was calculated using a fixed value (−1.76) of m (cementation coefficient). Porosity calculated from formation factor is correlated to the measured porosity with a correlation factor (r) equal to 0.49.

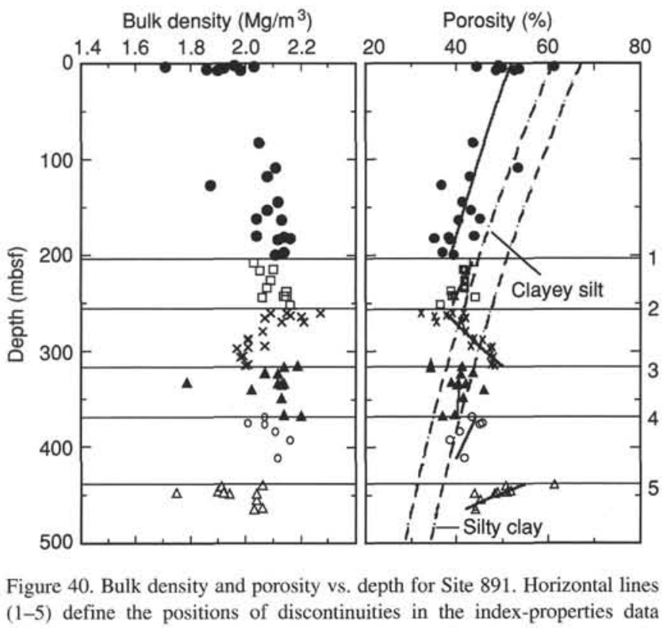

Figure 40. Bulk density and porosity vs. depth for Site 891. Horizontal lines (1–5) define the positions of discontinuities in the index-properties data described in the text. The dashed lines on the porosity plot are the normally consolidated porosity-depth functions for clayey silt and silty clay (Brückmann, 1989). Exponential fits to the porosity data between the defined discontinuities are shown. The exponential fitted equations are porosity = $51.8 \times 10^{(-0.00063 \times \text{depth})}$ for the filled circles ($R = 0.8$); porosity = $71.2 \times 10^{(-0.00104 \times \text{depth})}$ for the squares ($R = 0.6$); porosity = $9.8 \times 10^{(0.00224 \times \text{depth})}$ for the crosses ($R = 0.9$); porosity = $44.3 \times 10^{(-0.00012 \times \text{depth})}$ for the filled triangles ($R = 0.1$); porosity = $105.1 \times 10^{(-0.00102 \times \text{depth})}$ for the open circles ($R = 0.1$); and porosity = $5082 \times 10^{(-0.00449 \times \text{depth})}$ for the open triangles ($R = 0.8$).

Table 9. Summary of index property data, Holes 891A and 891B.

Core, section, interval (cm)	Depth (mbsf)	Bulk density (Mg/m^3)	Porosity (%)	Water content (%) dry mass	total mass	Grain density (Mg/m^3)	Dry-bulk density (Mg/m^3)
146-891A-							
1H-2, 120	2.70	1.96	49.2	33.7	25.2	2.75	1.47
1H-3, 45	3.45	1.71	61.2	56.5	36.0	2.68	1.09
1H-3, 110	4.10	2.03	44.4	28.1	21.9	2.78	1.59
2H-1, 25	4.95	1.92	50.0	35.5	26.2	2.68	1.42
2H-2, 10	6.30	1.86	53.6	40.8	28.9	2.67	1.32
3H-1, 15	7.45	1.90	52.5	38.6	27.8	2.70	1.37
2H-CC, 5	7.75	1.98	48.5	32.7	24.6	2.68	1.49
146-891B-							
10X-1, 28	83.38	2.05	43.5	27.1	21.3	2.74	1.61
14X-1, 35	109.90	2.11	53.4	34.2	25.4	2.59	1.57
15X-1, 26	118.70	2.08	42.8	26.1	20.7	2.77	1.65
16X-1, 44	127.70	1.87	36.8	24.6	19.7	2.79	1.50
18X-1, 40	145.50	2.12	41.1	24.2	19.5	2.77	1.71
19X-1, 42	154.30	2.08	43.0	26.2	20.7	2.79	1.65
20X-1, 20	162.90	2.04	45.3	28.7	22.3	2.78	1.59
20X-1, 70	163.40	2.13	40.5	23.6	19.1	2.74	1.73
23X-1, 15	180.70	2.04	43.8	27.5	21.5	2.70	1.60
23X-1, 85	181.40	2.14	38.4	22.0	18.0	2.76	1.75
23X-2, 20	182.20	2.16	35.2	19.5	16.3	2.71	1.81
23X-CC, 15	183.70	2.12	38.5	22.4	18.3	2.70	1.73
25X-1, 21	198.40	2.14	37.1	21.1	17.4	2.71	1.76
25X-CC, 38	200.10	2.11	39.4	23.1	18.7	2.76	1.71
26X-1, 21	207.30	2.03	43.9	27.8	21.7	2.76	1.59
27X-1, 12	216.00	2.10	41.5	24.8	19.8	2.71	1.68
27X-1, 26	216.20	2.05	41.9	25.9	20.5	2.73	1.62
28X-CC, 12	226.30	2.09	41.6	25.0	20.0	2.74	1.67
29X-1, 75	234.40	2.08	41.8	25.2	20.1	2.75	1.66
30X-1, 7	237.70	2.15	38.9	22.2	18.1	2.71	1.76
31X-1, 30	242.70	2.14	39.7	22.8	18.6	2.74	1.74
31X-1, 70	243.10	2.15	39.2	22.4	18.3	2.74	1.76
31X-CC, 10	244.00	2.06	44.0	27.3	21.4	2.73	1.62
32X-1, 18	251.60	2.16	36.5	20.5	17.0	2.73	1.79
33X-1, 15	260.40	2.15	39.1	22.4	18.3	2.73	1.76
33X-1, 50	260.70	2.09	41.5	25.0	20.0	2.70	1.67
33X-1, 60	260.80	2.27	32.1	16.5	14.1	2.72	1.95
34X-1, 40	263.50	2.16	37.7	21.3	17.5	2.74	1.78
34X-2, 20	264.80	2.20	35.2	19.1	16.0	2.75	1.85
34X-3, 4	266.10	2.07	41.9	25.5	20.3	2.66	1.65
35X-1, 40	269.40	2.21	35.7	19.4	16.2	2.74	1.85
35X-1, 105	270.10	2.13	40.8	23.8	19.2	2.71	1.72
37X-1, 22	279.00	2.06	42.0	25.8	20.5	2.67	1.64
38X-1, 110	287.50	2.01	43.9	28.1	21.9	2.68	1.57
38X-2, 40	288.30	2.01	45.8	29.8	22.9	2.70	1.55
39X-1, 22	295.30	2.07	43.0	26.4	20.9	2.70	1.64
39X-1, 72	295.80	2.01	47.9	31.5	23.9	2.65	1.53
39X-2, 34	296.90	1.97	47.4	31.8	24.1	2.66	1.50
40X-1, 75	304.80	1.99	47.4	31.5	23.9	2.72	1.51
40X-2, 28	305.80	1.98	48.0	32.2	24.3	2.65	1.50
41X-1, 45	313.30	2.01	47.5	31.1	23.7	2.70	1.54
41X-2, 40	314.70	2.00	48.4	32.2	24.3	2.70	1.51
41X-2, 90	315.20	2.19	34.4	18.7	15.7	2.72	1.84
41X-3, 5	315.90	2.14	41.1	24.0	19.3	2.73	1.72
42X-1, 55	322.20	2.07	43.7	26.9	21.2	2.71	1.63
42X-1, 135	323.00	2.12	40.9	24.0	19.4	2.73	1.71
43X-2, 2	331.90	1.79	38.7	27.7	21.7	2.74	1.40
43X-2, 120	333.10	2.14	40.3	23.3	18.9	2.73	1.74
43X-3, 10	333.50	2.12	41.9	24.8	19.9	2.71	1.70
43X-4, 25	335.2	2.13	40.1	23.3	18.9	2.75	1.73
44X-1, 20	339.5	2.02	46.0	29.7	22.9	2.76	1.56
45X-1, 20	348.4	2.13	41.4	24.2	19.5	2.78	1.72
47X-1, 15	366.3	2.14	39.6	22.8	18.5	2.78	1.75
47X-2, 15	367.8	2.20	37.0	20.3	16.9	2.74	1.83
47X-2, 85	368.5	2.07	43.3	26.6	21.0	2.73	1.64
48X-1, 55	375.6	2.01	45.8	29.7	22.9	2.74	1.55
48X-CC, 20	376.7	2.07	45.2	28.1	21.9	2.76	1.62
49X-1, 20	384.1	2.11	40.8	24.1	19.4	2.75	1.70
50X-1, 34	393.1	2.16	38.6	21.9	17.9	2.82	1.77
52X-1, 85	411.4	2.12	41.8	24.7	19.8	2.78	1.70
55X-1, 6	437.1	2.33	26.8	13.0	11.5	2.72	2.06
55X-2, 38	438.9	2.06	61.4	43.0	30.0	2.74	1.44
55X-3, 40	440.4	1.91	50.8	36.6	26.8	2.71	1.40
56X-1, 45	446.3	1.90	51.8	37.8	27.4	2.68	1.38
56X-1, 62	446.4	1.75	48.8	39.0	28.0	2.74	1.26
56X-2, 20	447.5	1.92	50.9	36.2	26.6	2.71	1.41
56X-2, 74	448.0	1.94	48.3	33.4	25.0	2.68	1.46
56X-CC, 30	448.5	2.04	43.8	27.5	21.6	2.71	1.60
57X-1, 35	455.1	2.04	45.2	28.6	22.2	2.70	1.59
58X-1, 20	463.7	2.06	44.0	27.4	21.5	2.80	1.62
58X-1, 70	464.2	2.03	44.2	28.0	21.9	2.77	1.58
58X-CC, 20	467.4	2.10	40.7	24.1	19.4	2.74	1.70

In general, formation factor increases and calculated porosity decreases with depth (Fig. 42 and Table 10). The lack of data between 8 and 83 mbsf was the result of low core recovery and poor sample quality. Formation factor below 100 mbsf decreases overall with depth to reach a minimum at 200 mbsf. Below 200 mbsf, formation factor increases with depth, reaching a maximum at 260 mbsf. Several other discontinuities occur below 260 mbsf. Both formation factor and the calculated porosity indicate inverse trends between 260 and 300 mbsf and scatter below 300 mbsf. These discontinuities may correspond to fault zones as suggested by structural observations (see "Structural Geology" section, this chapter). Low values of formation factor at about 450 mbsf may be attributed to underconsolidation below an impermeable layer, as indicated by the index-properties measurements.

Acoustic Velocity

Discrete measurements of acoustic compressional-wave velocity were completed for a limited number of intervals at Site 891 because

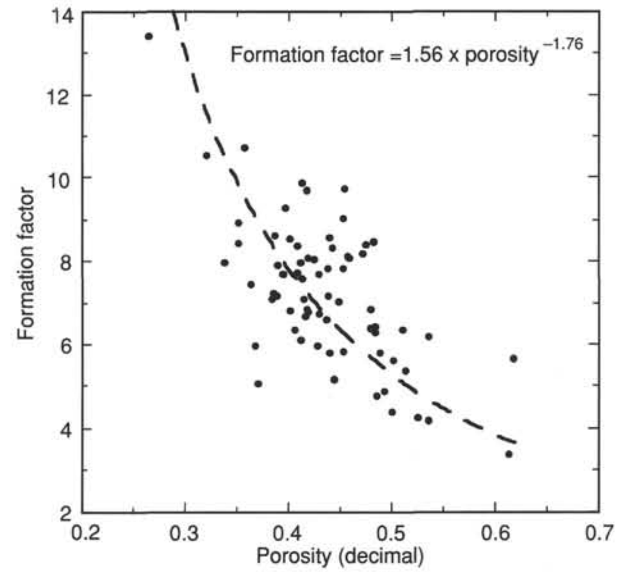

Figure 41. Formation factor vs. measured porosity for Site 891. The curve fit shown is of the form proposed by Archie (1942).

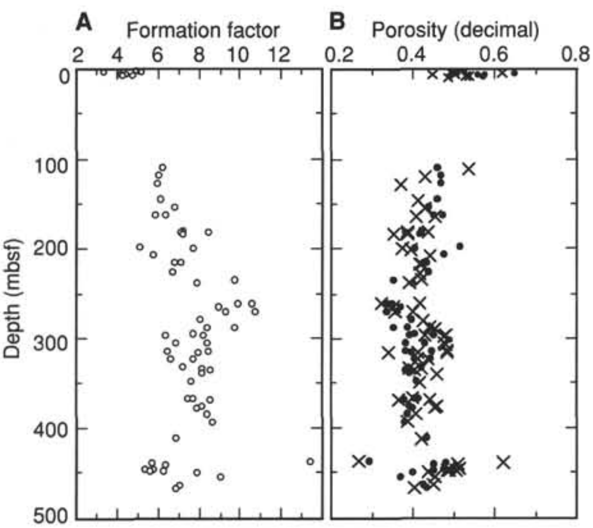

Figure 42. **A.** Formation factor vs. depth for Site 891. **B.** Measured porosity (crosses) and porosity calculated from formation factor (filled circles) vs. depth for Site 891.

Table 10. Resistivity, formation factor, and calculated porosity, Holes 891A and 891B.

Core, section, interval (cm)	Depth (mbsf)	Voltage (mV)	Sample resistivity (Ωm)	Formation factor	Calculated porosity (%)
146-891A-					
1H-2, 120	2.70	22.70	1.008	4.876	49.21
1H-3, 45	3.45	15.60	0.693	3.351	61.23
1H-3, 110	4.10	24.10	1.070	5.167	44.41
2H-1, 25	4.95	21.10	0.937	4.397	49.95
2H-2, 10	6.30	19.97	0.887	4.162	53.56
3H-1, 15	7.45	19.90	0.884	4.227	52.46
146-891B-					
14X-1, 35	109.85	29.80	1.323	6.187	53.44
15X-1, 26	118.66	28.80	1.279	5.979	42.84
16X-1, 44	127.74	29.00	1.288	5.951	36.83
18X-1, 40	145.50	29.00	1.288	6.102	41.13
19X-1, 42	154.32	32.60	1.447	6.729	42.96
20X-1, 20	162.90	28.30	1.256	5.841	45.34
20X-1, 70	163.40	30.70	1.363	6.349	40.53
23X-1, 15	180.65	34.70	1.541	7.176	43.79
23X-1, 85	181.35	34.30	1.523	7.093	38.38
23X-2, 20	182.20	40.90	1.816	8.442	35.19
23X-CC, 15	183.65	35.00	1.554	7.224	38.48
25X-1, 21	198.41	23.70	1.052	5.043	37.12
25X-CC, 38	200.08	36.76	1.632	7.690	39.35
26X-1, 20	207.30	27.60	1.225	5.785	43.91
27X-1, 12	216.02	34.10	1.514	7.079	41.51
27X-1, 26	216.16	32.70	1.452	6.789	41.85
28X-CC, 12	226.32	32.00	1.421	6.656	41.63
29X-1, 75	234.35	46.40	2.060	9.688	41.75
30X-1, 7	237.67	38.30	1.700	7.890	38.91
33X-1, 50	260.70	47.00	2.087	9.889	41.38
33X-1, 60	260.80	50.20	2.229	10.562	32.06
34X-2, 20	264.80	43.20	1.918	8.934	35.15
35X-1, 40	269.40	52.00	2.309	10.733	35.68
35X-1, 105	270.05	45.00	1.998	9.288	39.74
37X-1, 22	279.02	39.00	1.731	8.050	42.49
38X-1, 110	287.50	41.00	1.820	8.332	44.18
38X-2, 40	288.30	47.60	2.113	9.749	45.46
39X-1, 22	295.32	36.70	1.629	7.678	42.97
39X-1, 72	295.82	30.50	1.354	6.381	47.85
39X-CC, 34	296.94	39.10	1.736	8.180	47.25
40X-1, 75	304.75	40.20	1.785	8.410	47.47
40X-2, 28	305.78	32.80	1.456	6.862	47.95
41X-1, 45	313.25	41.30	1.834	8.459	48.20
41X-2, 40	314.70	31.40	1.394	6.431	48.35
41X-2, 90	315.20	39.00	1.731	7.988	33.80
41X-CC, 5	315.85	39.00	1.731	7.988	41.14
42X-1, 55	322.15	32.30	1.434	6.590	43.69
42X-1, 135	322.95	37.80	1.678	7.712	40.93
43X-2, 3	331.93	34.70	1.541	7.162	38.80
43X-3, 10	333.50	39.20	1.740	8.091	41.87
43X-CC, 25	335.15	41.30	1.834	8.525	40.10
44X-1, 20	339.50	39.20	1.740	8.091	45.91
45X-1, 20	348.40	36.70	1.629	7.575	41.38
47X-2, 85	368.45	41.50	1.842	8.566	43.90
47X-2, 15	367.75	36.10	1.603	7.451	36.39
48X-1, 55	375.55	39.30	1.745	8.112	45.76
48X-CC, 20	376.70	38.00	1.687	7.843	45.24
49X-1, 20	384.10	40.50	1.798	8.360	40.81
50X-1, 34	393.14	40.70	1.807	8.612	38.62
52X-1, 85	411.35	33.20	1.474	6.840	41.82
55X-1, 6	437.06	65.00	2.886	13.416	26.55
55X-2, 38	438.88	27.30	1.212	5.635	61.77
55X-3, 40	440.4	30.80	1.367	6.357	50.96
56X-1, 45	446.25	26.00	1.154	5.367	51.31
56X-1, 62	446.42	28.00	1.243	5.779	48.79
56X-2, 20	447.5	27.20	1.208	5.614	50.19
56X-2, 74	448.04	30.50	1.354	6.295	48.34
56X-CC, 30	449.1	38.00	1.687	7.843	43.75
57X-1, 35	455.05	43.70	1.940	9.020	45.21
58X-1, 20	463.7	34.00	1.510	7.018	44.91
58X-1, 70	464.2	34.00	1.510	7.018	44.91
58X-CC, 20	466.7	33.00	1.465	6.811	40.10

of low core recovery and poor sample quality. In general, acoustic velocity increases with depth over the interval 0 to 220 mbsf from 1538 m/s to approximately 1800 m/s. (Fig. 43). Throughout the hole, acoustic velocity is variable, reflecting the variations observed in the index-properties data. A large change in velocity occurs at 305 mbsf, where velocity decreases downhole from approximately 1800 m/s to less than 1600 m/s over an interval of about 2 m. Below 439 mbsf,

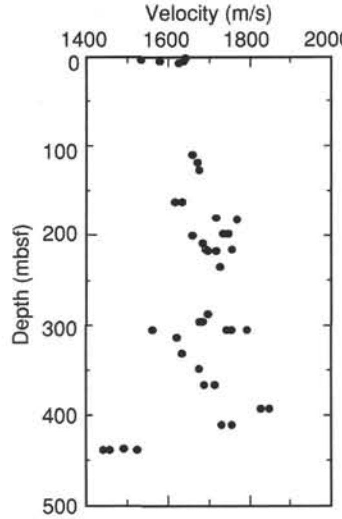

Figure 43. Acoustic compressional-wave velocity measured on discrete samples vs. depth, Site 891.

velocity decreases to the lowest values at this site (1441–1526 m/s). These low values of acoustic velocity are typical for surficial fine-grained sediment. This decrease corresponds with the density and porosity discontinuities in the index-properties data at 439 mbsf.

Undrained Shear Strength

Undrained shear strength (S_u) measurements were made using a motorized miniature vane-shear device and a pocket penetrometer (see "Explanatory Notes" chapter, this volume). Measurements made using the miniature vane-shear device are not reported here because the sediment cracked before failure for each of these tests. All data reported here are from the pocket penetrometer (Table 11).

In Hole 891A, shear-strength values ranged from 98 to 221 kPa. These measurements were made in sediments interpreted as debris-flow deposits (see "Lithostratigraphy" section, this chapter). The lower shear-strength values (98–110 kPa) represent the shear strength of the (debris-flow) matrix and the higher values (172–221 kPa) were measured in the mud clasts. The strength values of the matrix are high for sediment this shallow in the section, and indicate overconsolidation. Estimates of the amount of overburden that may have been removed at this hole range from 57 to 128 m (Table 11).

Four measurements were made on sediments between 110 and 216 mbsf in Hole 891B. These measurements suggest a normal to slightly underconsolidated state with S_u/P_o' values less than 0.25 (Table 11). Measurements made on samples from the bottom of Hole 891B show considerable underconsolidation with low S_u/P_o' values. Estimated original burial depths for the interval from 440 mbsf to the bottom of the hole result in large negative values of eroded sediment thickness, which suggests that this interval was rapidly buried by the overlying sediment column.

Thermal Conductivity

Thermal conductivity was measured on sediment samples using the needle-probe method in the full-space mode (see "Explanatory Notes" chapter, this volume). Measurements were usually taken at four points per core in cores with good recovery. The measured values are given in Table 12 and plotted as a function of depth in Figure 44. Values range from 1.18 to 1.82 W/(m · K), with a mean of 1.44 W/(m · K) and a standard deviation of 0.16 W/(m · K). No apparent trend occurs with depth. Higher values were measured in quartz-rich sands near 180–200, 310–325, and 465 mbsf.

Table 11. Undrained shear strength, Holes 891A and 891B (lithostratigraphic Unit I).

Core, section, interval (cm)	Depth (mbsf)	Bulk density (Mg/m^3)	Undrained shear strength (S_u) (kPa)	Overburden pressure (P_o') (kPa)	S_u/P_o'	Normally consolidated S_u (kPa)	Estimated burial depth (mbsf)
146-891A-							
1H-2, 120	2.70	1.96	172	25	6.91	6	91
1H-3, 42	3.45	1.71	98	30	3.28	7	69
2H-1, 25	4.95	1.92	191	43	4.44	11	104
2H-2, 10	6.10	1.86	221	52	4.20	13	128
3H-1, 15	7.45	1.90	110	64	1.72	16	57
146-891B-							
14X-1, 25	109.75	2.11	196	1153	0.17	288	-18
16X-1, 44	127.74	1.87	196	1302	0.15	325	-9
25X-CC, 38	199.19	2.14	>250	2083			
27X-1, 12	216.02	2.05	>250	2253			
55X-3, 4	440.04	2.14	216	4703	0.05	1176	-341
55X-1, 22	437.22	2.33	>250	4667			
56X-2, 20	447.50	1.92	140	4757	0.03	1189	-368
56X-CC, 30	447.87	1.94	159	4760	0.03	1190	-359
57X-1, 35	455.05	2.04	127	4832	0.03	1208	-391
58X-1, 70	464.20	2.03	110	4922	0.02	1230	-408

Table 12. Thermal conductivity data, Site 891.

Depth (mbsf)	Thermal conductivity (W/[m · K])	Depth (mbsf)	Thermal conductivity (W/[m · K])	Depth (mbsf)	Thermal conductivity (W/[m · K])
146-891A-		181.36	1.54	322.26	1.41
2.50	1.32	182.40	1.74	322.75	1.59
3.30	1.31	198.35	1.74	331.77	1.46
3.30	1.31	199.03	1.50	331.97	1.20
4.25	1.33	199.03	1.35	339.50	1.31
5.00	1.30	207.30	1.52	348.40	1.49
5.25	1.32	207.48	1.60	348.65	1.25
5.50	1.47	216.27	1.32	366.18	1.47
6.19	1.38	224.92	1.37	366.60	1.42
7.60	1.82	242.86	1.26	367.74	1.46
7.90	1.48	243.21	1.33	368.45	1.35
		243.53	1.32	411.48	1.76
146-891B-		269.56	1.18	439.43	1.50
65.25	1.43	269.71	1.25	446.86	1.32
65.30	1.70	270.19	1.21	447.18	1.26
109.92	1.65	270.32	1.28	447.44	1.27
110.34	1.59	289.41	1.45	454.78	1.45
118.82	1.65	295.34	1.23	454.94	1.30
127.75	1.54	296.44	1.22	463.71	1.29
127.75	1.56	305.02	1.35	464.16	1.26
162.92	1.31	305.88	1.40	464.85	1.28
163.45	1.45	313.05	1.54	465.03	1.76
164.51	1.55	313.68	1.62	465.20	1.59
176.83	1.53	315.08	1.51	465.44	1.59
176.47	1.52	322.00	1.36	465.79	1.60
181.26	1.69				

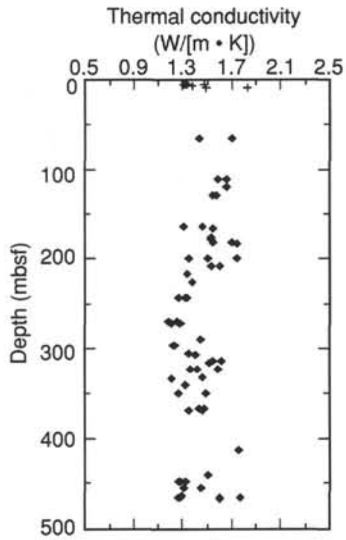

Figure 44. Thermal conductivity vs. depth, Site 891.

WSTP AND ADARA TEMPERATURE MEASUREMENTS

Five WSTP temperature measurements (see "Explanatory Notes" chapter, this volume) were attempted in Hole 891B from 29.6 to 162.7 mbsf (Table 13). None were clearly successful. Data recorded during the deployment at 136.2 mbsf were lost during downloading of the tool memory after deployment. The four other measurements show highly disturbed decay curves with pronounced secondary heat pulses that appear to reflect vertical movements of the probe in sediment (Figs. 45–47). The generally disturbed nature of the temperature records in addition to the lack of heat pulses on extraction suggest poor penetration at 29.6, 56.2, and 162.7 mbsf, with vertical movements of the probe producing partial, if not complete, withdrawals. The disturbances at 29.6, 56.2, and 162.7 mbsf are sufficiently severe to prevent meaningful estimates of the equilibrium temperatures. The temperature record at 92.0 mbsf is the least disturbed. A tentative calculation of the equilibrium temperature from a fairly undisturbed, intermediate part of the decay curve (between 4180 and 4820 s; Fig. 46B) indicates an equilibrium temperature of 4.16° ± 0.05°C. An attempt was also made to estimate the highest temperature equilibrium that could be derived from the disturbed decay curve at 162.7 mbsf. From a less disturbed, intermediate part of the decay curve between 3040 s and 3260 s (Fig. 47B), an equilibrium temperature of 7.09° ± 0.05°C was calculated.

The temperature difference of 1.6°C measured between the seafloor and 92 mbsf corresponds to a mean temperature gradient of 17°C/km. This low gradient is doubtful. The measurement at 92 mbsf was taken in sands (coarse sands were recovered from inside the lower housing of the WSTP tool). It is suspected that invasion of the sand layer by the cool drilling fluid disturbed the in-situ temperature field. The measured temperature and the determined gradient are lower bounds to in-situ conditions that could be substantially different. Similarly, the temperature difference of 4.09°C measured between the seafloor and 162.7 mbsf, which corresponds to a mean gradient of 25°C/km, is seen as a lower bound to in-situ conditions.

Table 13. Summary of WSTP temperature measurements, Hole 891B.

Core	Depth (mbsf)	Temperature above mud line (°C)	Temperature in sediment (°C)	Comments	Status
146-891B-					
4X	29.6	2.9		Doubtful penetration.	Rejected
7X	56.2	2.9		Doubtful penetration.	Rejected
11X	92.0	2.6	4.2?	Suspected invasion of formation by drilling fluid.	Doubtful
17X	136.2			Data lost during downloading of the tool memory.	No data
20X	162.7	3.0		Disturbed decay curve.	Rejected

Note: All measurements were taken with Probe 108.

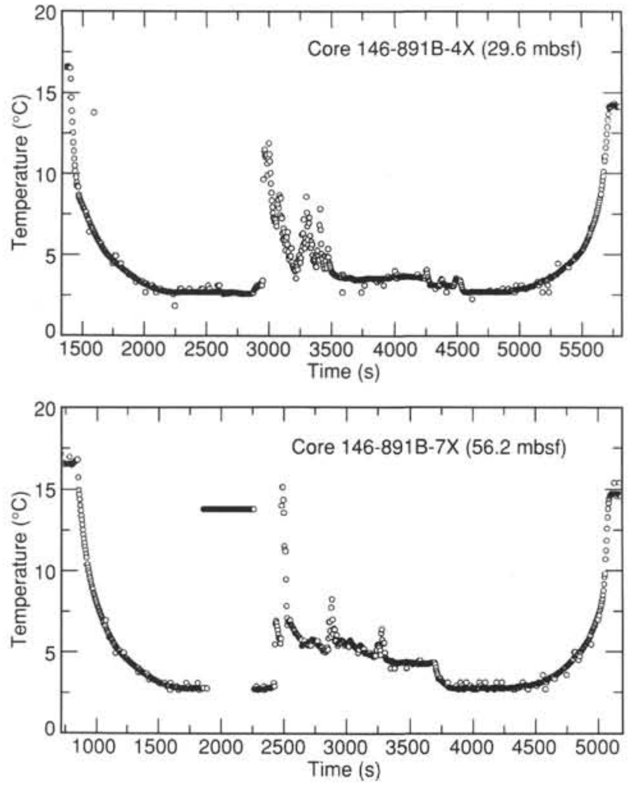

Figure 45. Temperature record from two WSTP deployments in Hole 891B.

DOWNHOLE LOGGING

Log Reliability

At Hole 891C, filling of the basal portion of the hole limited logging results to the upper 430 mbsf, with the exception of the VSP run, which reached 453 mbsf. Hole bridging prevented any logging of the interval from 287 to 304 mbsf and necessitated two runs of the geophysical tool string (from the surface to 287 mbsf and from 304 to 420 mbsf). In addition, only the lower portion of the hole (309 to 436 mbsf) was logged with the FMS. The geochemical tool string was run from 312 to 428 mbsf in the open hole and from the surface to 312 mbsf in-pipe. The VSP was run from 288 to 453 mbsf.

Hole instability also created many enlarged-diameter intervals (Fig. 48), which affected log quality. Density tool measurements in Hole 891C showed many low-value spikes because of the inability of the tool's caliper to remain in contact with the borehole wall (Fig. 48). We have deleted the obviously erroneous density values, but many of the lowest density measurements in the interval from 380 to 430 mbsf may be underestimates of the true bulk density (Fig. 48). The large and rapidly varying hole diameter may also have affected the quality of the neutron porosity measurements, which will be corrected post-cruise. Similarly, gamma-ray counts and resistivity may be slightly underestimated because of the large hole diameter. The absence of firm pressure on all four pads of the FMS tool is probably responsible for local degradation of the FMS data. In addition, data from one of the four FMS pads were noisy.

Reprocessing of the sonic velocity data from Hole 891C (see "Explanatory Notes" chapter, this volume) appears to have removed all unreliable data caused by cycle skipping or noise, and we consider the reprocessed velocity log (Fig. 49) to be of good quality. The resistivity measurements are expressed as formation resistivities rather

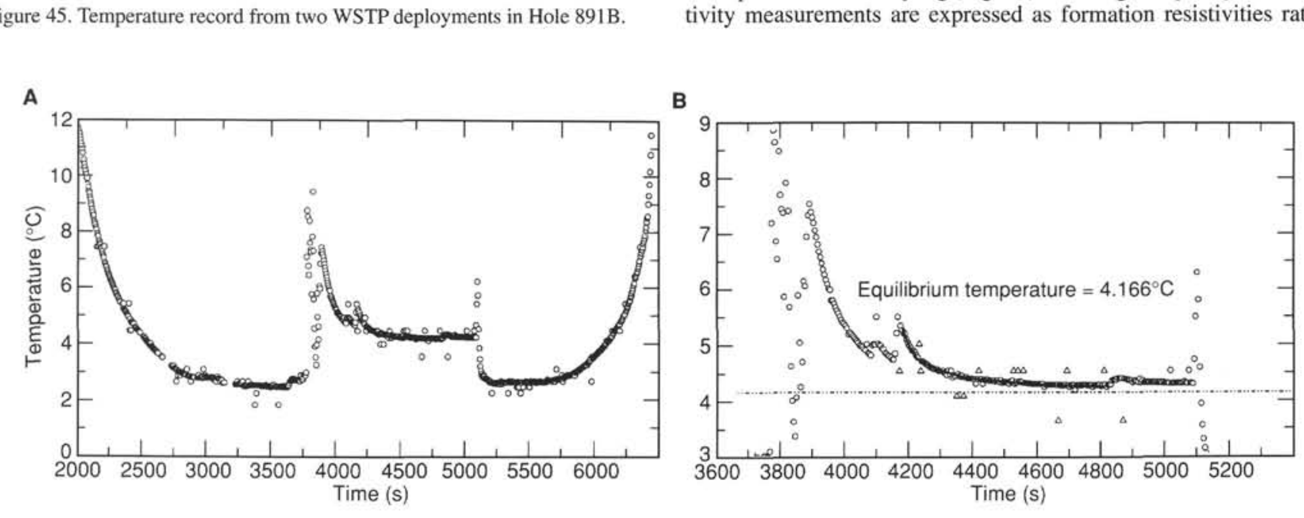

Figure 46. Record from WSTP deployment in Hole 891B at 92 mbsf (Core 146-891B-11X). **A.** Temperature record for entire run. **B.** Close-up of temperature record in sediment. The solid line (4180–4820 s) is the regression line used to estimate the equilibrium temperature shown by the dashed line. Triangles are points not used for the fit calculation.

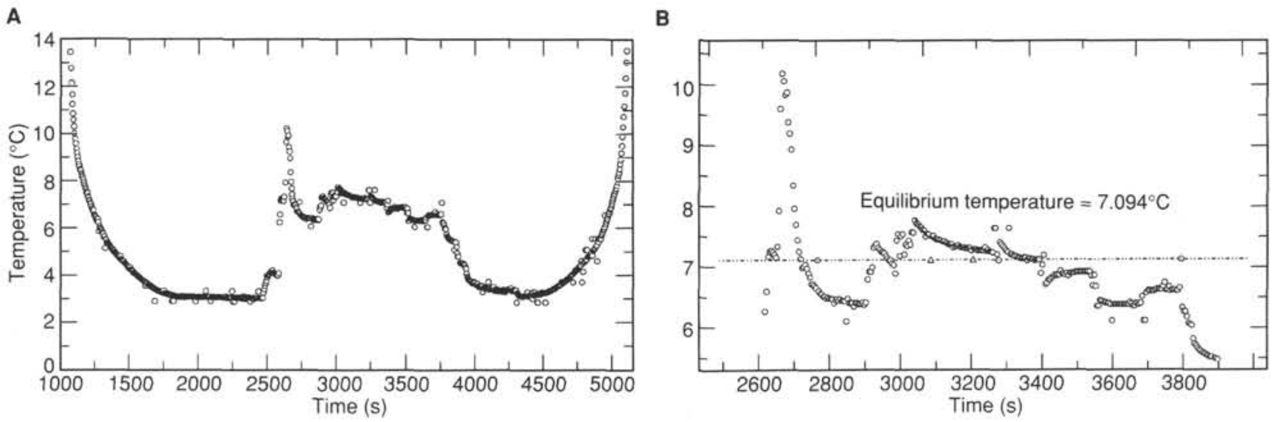

Figure 47. Record from WSTP deployment in Hole 891B at 162.7 mbsf (Core 146-891B-20X). **A.** Temperature record for entire run. **B.** Close-up of temperature record in sediment. Symbols and conventions as in Figure 46. The regression line extends from 3040 to 3260 s.

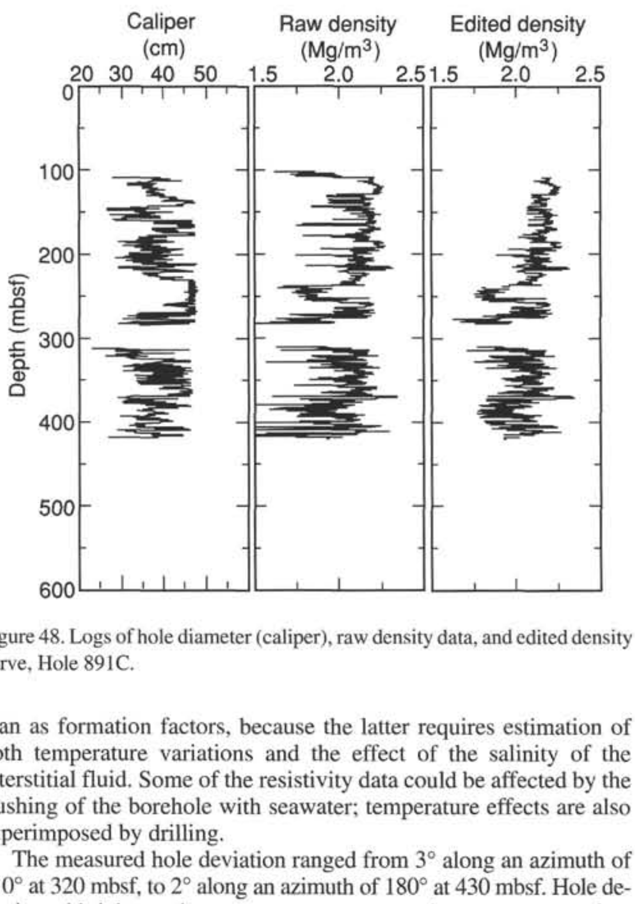

Figure 48. Logs of hole diameter (caliper), raw density data, and edited density curve, Hole 891C.

than as formation factors, because the latter requires estimation of both temperature variations and the effect of the salinity of the interstitial fluid. Some of the resistivity data could be affected by the flushing of the borehole with seawater; temperature effects are also superimposed by drilling.

The measured hole deviation ranged from 3° along an azimuth of 110° at 320 mbsf, to 2° along an azimuth of 180° at 430 mbsf. Hole deviation adds inherent inaccuracy to any structural measurements taken on the cores or from FMS data, and may be a cause of hole ellipticity.

Measurements from the geochemical run were corrected for pipe effects and converted to oxides post-cruise (see "Onshore Geochemical Processing" section, this chapter).

Porosities

Porosities for Site 891 can be estimated from three logs: resistivity, density, and neutron. Porosity determination from resistivity logs requires the estimation of both near-borehole formation temperatures and salinities, as well as calibration of the Archie (1942) coefficients *a* and *m*; this has not been attempted yet.

The density log (ρ_b) was converted to porosity (ϕ) using the relationship $\phi = (\rho_m - \rho_b)/(\rho_m - \rho_w)$, where water density ($\rho_m$) and grain density ($\rho_m$) were assumed to be 1.05 and 2.80 Mg/m^3, respectively; this estimate of grain density is based on index-properties measurements of the core (see "Physical Properties" section, this chapter). As discussed previously, the density data are noisy owing to borehole-size effects; consequently, we consider neutron porosities to be our most accurate shipboard estimation of in-situ porosities (Fig. 50). These neutron porosities may be too high by as much as several percent, because of both the presence of bound water in clay minerals and the deployment of the tool without eccentralization (see "Explanatory Notes" chapter, this volume).

Correlation of Logs to Lithostratigraphic Units

Logging results provide information to supplement lithologic data from the cores. Recovery at Hole 891B was poor and may be biased toward finer grained sediments. Examination of the spectral gamma log permits an estimate of the lithologic variation at Site 891. Gamma-ray values are rarely less than 50 API units (Fig. 49); in contrast, the sands observed at Site 888 showed a baseline of 30 API units (see "Downhole Logging" section, "Site 888" chapter, this volume). This suggests that the sands at Hole 891C are not clean, but contain clay or other potassium-, thorium-, or uranium-bearing minerals.

Gamma-ray values from Hole 891C decrease from below the base of pipe (104 mbsf) to about 200 to 220 mbsf (Fig. 49); a small (5 API units) shift is observed at about 170 mbsf. At about 220 mbsf, a spike in the gamma-ray values is associated with a 2- to 3-m-thick high-velocity, high-resistivity, and low-porosity layer. From 221 to 266 mbsf (the deepest gamma-ray log data in the upper run), gamma-ray values steadily increase. Porosities increase downhole to about 220 mbsf, decrease from 220 to 250 mbsf and then increase (Fig. 49); resistivity and density data show an inflection point at approximately 260 to 280 mbsf, whereas the velocity data are inconclusive. Except for the density log, which was unreliable, all logs show decreased fluctuations within the interval from 221 to 266 mbsf compared to the section above 220 mbsf. High porosity and low resistivity values observed below 280 mbsf are consistent with the occurrence of a bridge below this depth, because swelled clays would be expected to exhibit high neutron porosity and low resistivity.

In the lower logged interval, gamma-ray values decrease, exhibit a prominent spike at about 370 mbsf, and then increase (Fig. 51). The gamma-ray spike is associated with a layer of high density, high velocity, and high resistivity and a slight porosity decrease. Below this spike a shift to higher velocities and resistivities was observed, whereas densities show a shift to lower values and porosities appear

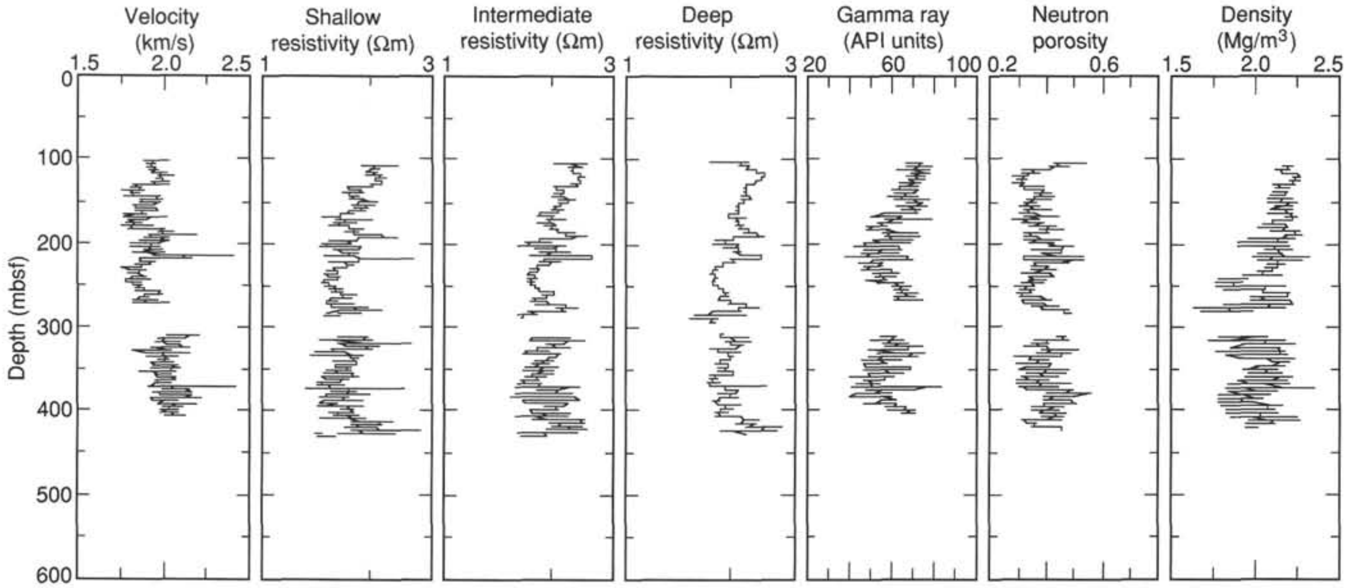

Figure 49. Logs of velocities from sonic traveltimes, shallow resistivity, intermediate resistivity, deep resistivity, gamma ray, neutron porosity, and density, Hole 891C.

to shift to higher values. If this inverse relationship between velocity and density is real, its cause is unknown.

The recovered sediments (see "Lithostratigraphy" section, this chapter) show no major lithologic changes, although three subunits (IA, 0–198.2 mbsf; IB, 198.2–383.9 mbsf; and IC, 383.9–472.3 mbsf) were defined. The depths of the Subunit IA/IB boundary roughly coincide with the observed changes at 200 to 220 mbsf in the logs. The Subunit IB/IC boundary is about 14 m below the shift observed in the logs at 370 mbsf.

For most of Hole 891C, variations in gamma-ray values are negatively correlated with variations in neutron porosity (Fig. 49). This pattern, which was also observed at Site 889, suggests either a wide distribution of grain sizes or compaction of the clays (see "Downhole Logging" section, "Site 889" chapter, this volume). Trends in the gamma-ray values appear to vary positively with trends in velocity

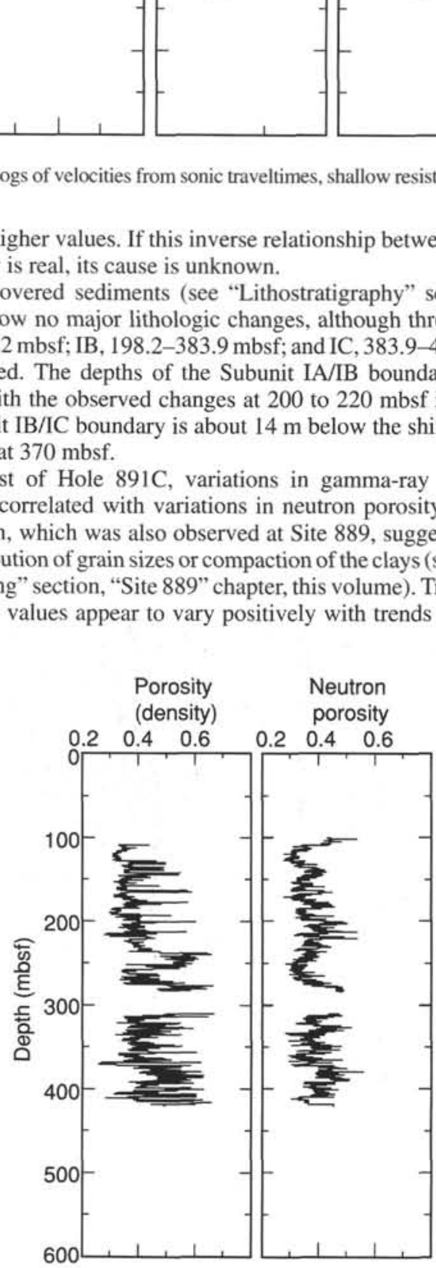

Figure 50. Porosities from edited density log shown in Figure 48 and neutron log, Hole 891C.

and resistivity and negatively with caliper values. An apparent positive correlation with the bulk-density log is obscured by data noise resulting from borehole size effects.

Vertical Seismic Profile

Acquisition

The zero-offset VSP at Site 891 was shot using a 300-in.^{3} air gun and a 400-in.^{3} water gun fired alternately. Gun and receiver geometries are shown in the "Explanatory Notes" chapter (this volume). Both guns were fired at 2000 psi. Signals were received by a three-component geophone (rather than the Schlumberger well seismic tool) and recorded at a 2-ms sample interval on a Sun workstation. In addition to the geophone signal, far-field source signatures were recorded for both guns throughout the experiment at a depth of about 150 m below the guns. Receiver stations (total = 24) were run beginning at the bottom of the logged hole (453 mbsf) and stepping uphole to 325 mbsf at 5-m intervals where hole conditions permitted; an additional station was obtained at 288 mbsf during the oblique seismic experiment. Each station consists of at least six shots each of air gun and water gun. The VSP data presented here (Fig. 52) are based on air-gun data only.

Time-Depth Relationship

The VSP provides an unambiguous time-depth relationship from the first-break time of the direct compressional-wave arrival at each receiver depth. Integration of the sonic log yields a time-depth curve with respect to the shallowest log value, but the sonic log provides no information on the traveltimes between the seafloor and the first sonic log measurement at 102 mbsf. Therefore, the lower portion of the sonic time-depth curve was shifted to sub-bottom time by using the VSP data to constrain the traveltimes in the interval above 325 mbsf (Fig. 52). No sonic log data are available for the interval from 273 to 310 mbsf; linear interpolation was used to fill this missing section. The anomalous traveltime given by the VSP station at 288 mbsf was not used.

The slope of the time-depth curve provides an average velocity over the specified interval. Above about 360–370 mbsf, sonic velocities are similar to the VSP velocities (Fig. 52). In contrast, sonic velocities are substantially slower than VSP velocities for the logged interval below 380 mbsf. Borehole damage can lower sonic velocities with respect to the velocities of undisturbed formation. For example, microfractured rock can undergo an increase in fracture aperture in the

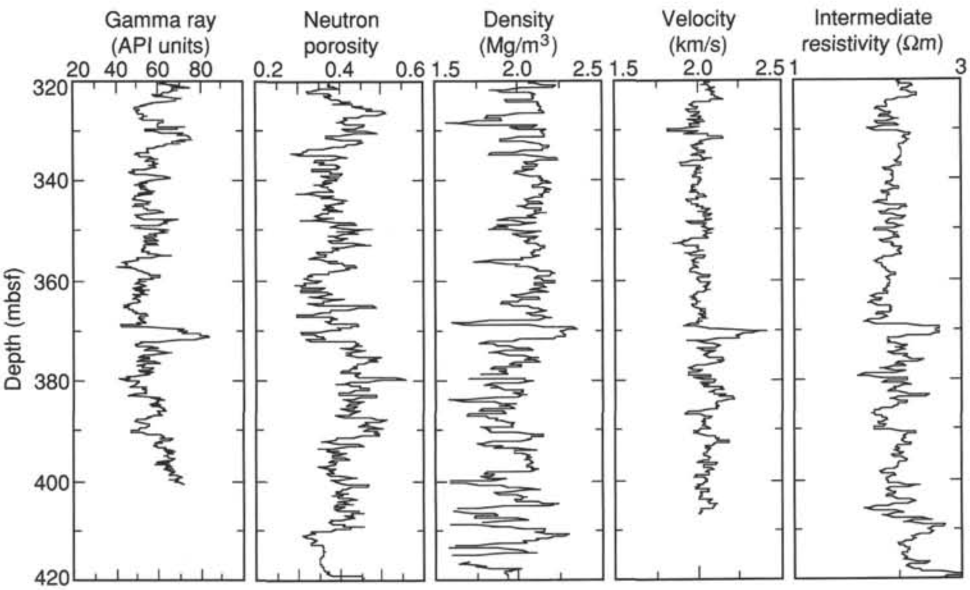

Figure 51. Logs from the interval 320–420 mbsf of gamma ray, neutron porosity, density, sonic velocity, and resistivity, Hole 891C.

immediate vicinity of the borehole. Borehole damage can be detected directly in the sonic log, because the long-spaced sonic log sees deeper into the formation than does the short-spaced log. Indeed, long-spaced sonic traveltime values are generally faster by 5–10 μs/ft (15–30 μs/m) than short-spaced values throughout much of the logged interval at this site; values shown in Figure 49 are the means of short- and long-spaced measurements. The difference is not, however, confined to the interval in which VSP velocities are faster than sonic velocities; nor is that interval recognized as a microfractured interval in the cores.

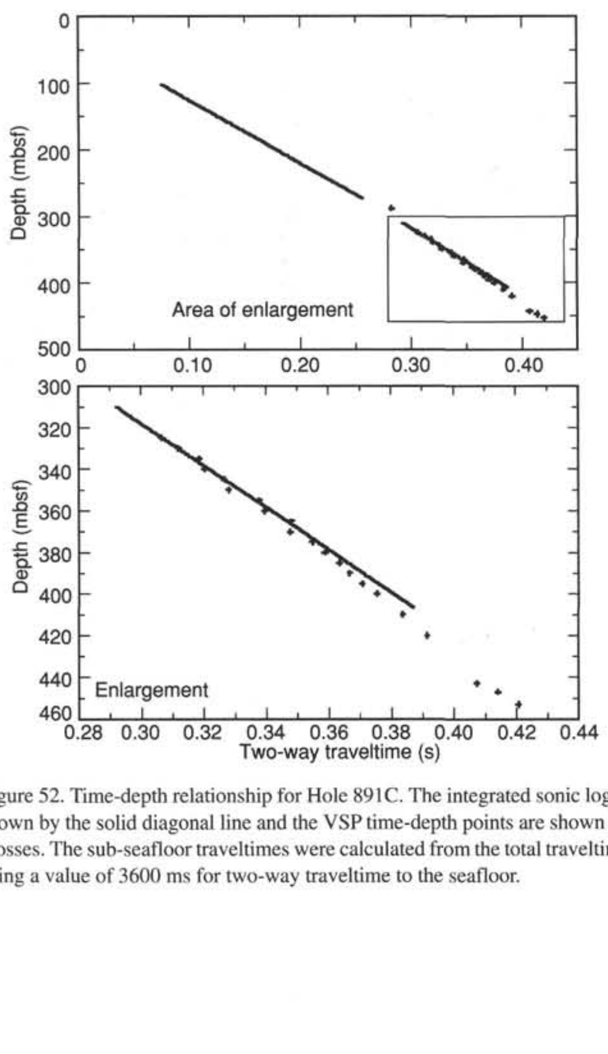

Figure 52. Time-depth relationship for Hole 891C. The integrated sonic log is shown by the solid diagonal line and the VSP time-depth points are shown by crosses. The sub-seafloor traveltimes were calculated from the total traveltime using a value of 3600 ms for two-way traveltime to the seafloor.

The VSP data provide the only in-situ velocity measurements in the region from 410 to 453 mbsf. The three deepest stations (443, 447, and 453 mbsf) appear to indicate a decrease in velocity from approximately 2.22 km/s (325–420 mbsf) to approximately 1.5 km/s (443–453 mbsf), consistent with a local increase in porosity at about 440 mbsf (see "Physical Properties" section, this chapter). If, however, the errors in these three values are as large as those in the interval from 330 to 370 mbsf (Fig. 52), the velocity in the interval from 443 to 453 may not be significantly lower than that above. Because the VSP at Site 891 was run with the three-component geophone in conjunction with the oblique seismic experiment, we could not use the Schlumberger software to pick the first-break time for direct arrivals. Instead, the traveltimes were hand-picked to the nearest 2-ms sample on the Sun workstation, resulting in a significant loss of accuracy in interval velocities. The traveltimes will be chosen again with greater accuracy post-cruise.

Synthetic Seismogram

A synthetic seismogram (Fig. 53) was created using a wavelet from the seismic-reflection data from the abyssal plain seaward of Site 891 and compared with seismic section OR89-41, which runs northward through Site 891. We calculated the synthetic seismogram for Hole 891C between 240 and 420 mbsf from the sonic-log velocities assuming constant density. The resulting synthetic seismogram fits the seismic trace directly beneath Hole 891C, but is dissimilar to nearby traces on the section. The poor match between the synthetic seismogram and the seismic section is a probable consequence of small scale lateral heterogeneity, but is also produced by the lack of effective migration of reflectors, which dip across the plane of the section. Improved correlation between the borehole-derived impedance data and the seismic reflection section waits upon more careful migration and analysis of the dip section from seismic line OR89-05.

Integration of Logging, Core, and Seismic-reflection Data

The availability of a time-depth curve from the VSP provides a powerful tool for locating features of the cores and logs on a seismic time section. As noted previously, a major structural boundary at 375 mbsf correlates with a high-velocity, high-resistivity, high-density, low-

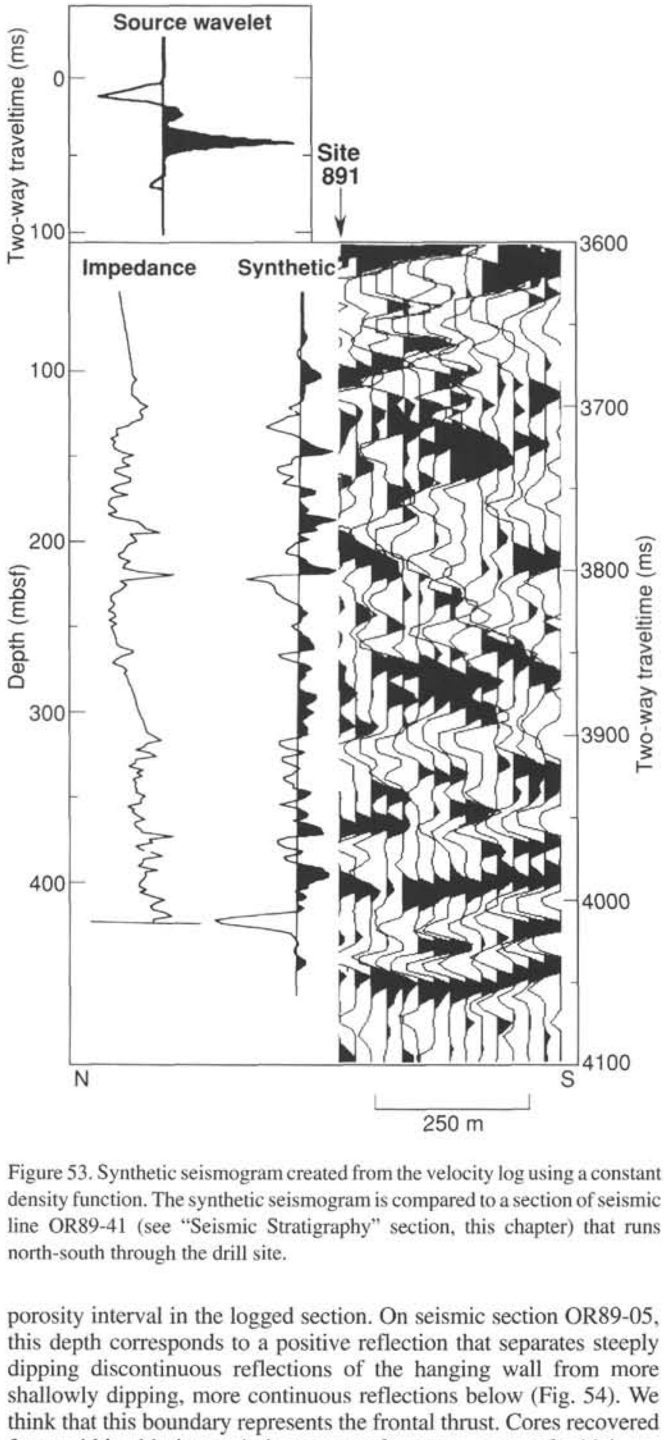

Figure 53. Synthetic seismogram created from the velocity log using a constant density function. The synthetic seismogram is compared to a section of seismic line OR89-41 (see "Seismic Stratigraphy" section, this chapter) that runs north-south through the drill site.

porosity interval in the logged section. On seismic section OR89-05, this depth corresponds to a positive reflection that separates steeply dipping discontinuous reflections of the hanging wall from more shallowly dipping, more continuous reflections below (Fig. 54). We think that this boundary represents the frontal thrust. Cores recovered from within this interval show many fractures, some of which are polished (See "Structural Geology" section, this chapter). The high values of density, velocity, and gamma-ray logs in this interval suggest that it is a compacted clay-rich zone. A possible interpretation is that the fault initially localized in this clay-rich layer and dewatered the zone through strain hardening.

Below 3960 ms at Site 891, the seismic layering becomes increasingly continuous, consistent with the lesser degree of deformation observed in the cores below 375 mbsf. Possibly, the section below 375 mbsf is being incorporated into the hanging wall because the frontal thrust at 375 mbsf is dewatered, and the porous sediments at the base of the hole provide a weak surface on which failure can occur. The lower line (A-A′–A″) in Figure 54 marks a possible surface onto which the frontal thrust may be stepping down. The interpreted fault offsets stratigraphic reflectors from A to A′ and continues from A′ to A″ subparallel to the sedimentary layering in the footwall.

The hanging wall is characterized by reflectors that dip seaward approximately parallel to the seafloor. We think that these are out-of-plane reflections, probably originating from the irregular surface of the seaward face of the first ridge. Moreover, development of an anticline as a result of translation up a uniformly inclined ramp predicts horizontal bedding surfaces at the position of Site 891 on the frontal ramp, not bedding dipping parallel to the slope (see "Seismic Stratigraphy" section, this chapter). Because the seaward-dipping reflectors are dominant and probably spurious, we have not attempted fine-scale interpretation of the hanging wall at Site 891.

Oblique Seismic Experiment

An oblique seismic experiment was conducted at Hole 889C (see "Operations" section, this chapter). The data will be processed by Dr. G.F. Moore at the University of Hawaii.

Formation MicroScanner Data

Two runs were made with the Formation MicroScanner (FMS) tool in Hole 891C at logging speeds of 550 m/hr. The first pass was from 436 to 312 mbsf, and the second pass was from 435 to 309 mbsf. Based on the FMS caliper data and the fact that the merged passes directly overlie each other, the entire borehole is consistently elliptical. As a result, the quality of certain intervals of Pass 1 and of almost all of Pass 2 is extremely poor. In Pass 1 the images are good only from 322 to 422 mbsf.

From the top of the logged interval (309 mbsf) to 368 mbsf, the images exhibit a high density of resistive polygonal features, broken by planar conductive features (Fig. 55), which exhibit abrupt variations in dip, and by parallel planes, some of which are across all four pads. This observation corresponds to fracture patterns described from the cores (see "Structural Geology" section, this chapter).

The most significant feature of the interval from 322 to 422 mbsf is a high-resistivity layer beginning at 368.2 mbsf and ending at 370.2 mbsf, which dips southeast at approximately 35° and coincides approximately with the depth of the frontal thrust. At this depth, steep fractures are observed (Fig. 56), and the caliper diameter is about 25 to 30 cm compared with the average of 40 cm for this hole.

Below approximately 370 mbsf (Fig. 57), conductivity in the images increases and fragmentation decreases, although steep fabrics exist. Below 380 mbsf, fewer fractures are observed.

Temperature

The Lamont-Doherty Geological Observatory temperature tool was run at the bottom of the geophysical tool string and at the bottom of the FMS tool. The data recorder from the tool run at the bottom of the geophysical tool string malfunctioned, preventing data recovery. The FMS is run at a speed of 550 m/hr, and it appears that the thermistor response lagged significantly. Because of this effect and because the hole temperature was reduced by circulation during hole conditioning immediately before logging, one cannot determine an equilibrium thermal profile from this logging run. Our recorded maximum temperature of 10°C at 428 mbsf is therefore a minimum estimate of equilibrium temperature.

Onshore Geochemical Processing

Figure 58 shows processed natural gamma-ray data collected by the geochemical tool string in Hole 891C. Figure 59 shows estimates of calcium carbonate and major oxide weight fractions derived from these data.

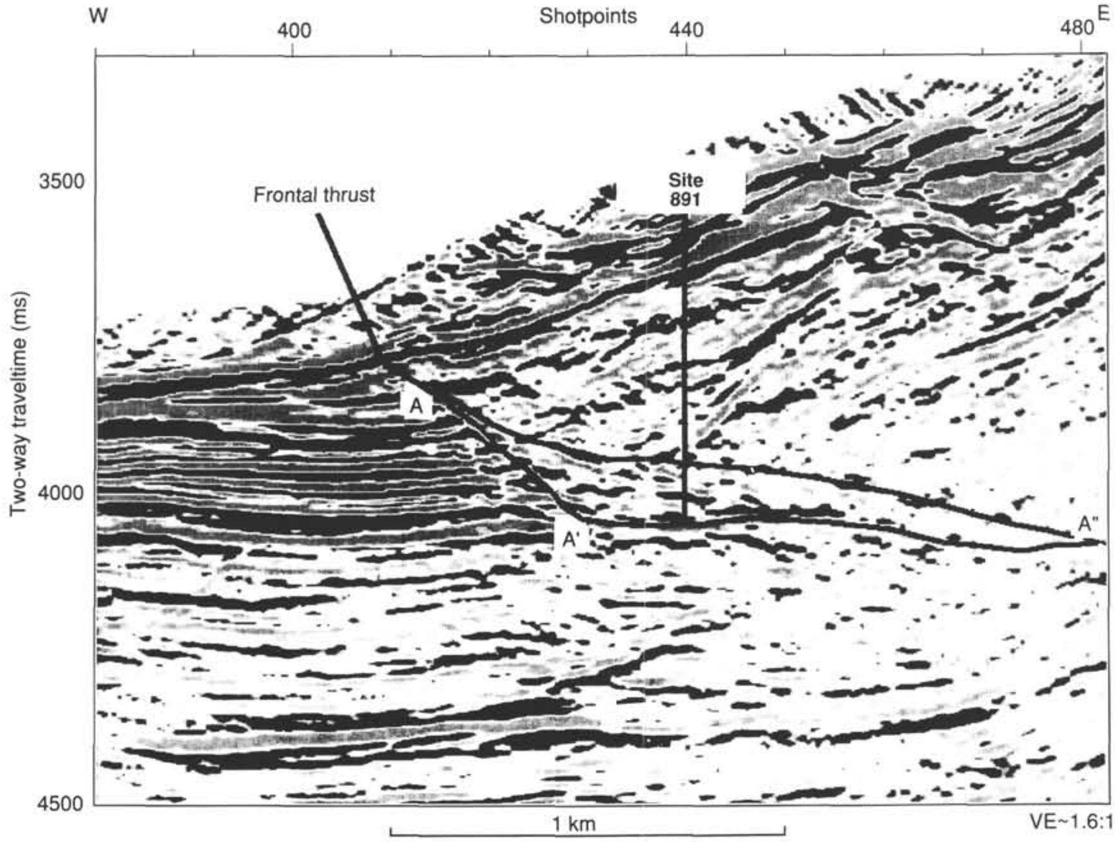

Figure 54. Seismic section OR89-05 at the frontal thrust. Site 891 is projected about 60 m to the south onto the line. The frontal thrust correlates with a thin zone of high velocity and high density. Lower line extending from A to A′ to A″ represents a surface onto which the frontal thrust may be stepping down. VE = vertical exaggeration.

SUMMARY AND CONCLUSIONS

Site 891 (proposed Site OM-3) lies at the foot of the continental slope off central Oregon, on the western flank of the first ridge on the lower continental slope (2663 mbsl; Fig. 1). At this location drilling penetrated the toe of the accretionary wedge and, at about 375 mbsf, intersected a seismically imaged, landward-dipping thrust fault connected to the décollement, which is inferred to be a significant fluid pathway. Site 891 was drilled to sample the pore fluids within the thrust fault, to record their temperature, to measure the in-situ permeability of the fault zone, and to determine the changes in physical properties associated with structural evolution and diagenesis. The scientific program achieved the first and last of these objectives.

Three holes were drilled at Site 891. Hole 891A was an aborted hole (total depth 9.9 mbsf), but the sampled fluid was clearly derived from >200 m sub-bottom depth. Hole 891B provided cores to a depth of 472 mbsf (Fig. 60). Hole 891C was drilled to 491 mbsf and logged.

Sediments recovered at this site are younger than middle Pleistocene as they are all normally magnetized (Brunhes Chron, <0.8 Ma) and most exhibit a characteristic late Pleistocene fauna (<0.6 Ma). Benthic foraminifers indicate that the sediments were originally deposited at lower bathyal depths.

The lithologies sampled consist dominantly of clayey silts and fine to medium sand. The latter are poorly sorted and are commonly cemented by carbonates, although weak carbonate cementation was observed in all lithologies. Allochthonous pebbles and diagenetic carbonate concretions are distributed randomly throughout the section. Several cores below 200 mbsf contain wood fragments. Because of the compositional and textural similarity of all sediments recovered at Site 891, only one lithostratigraphic unit was designated. Within this unit, three subunits were defined. Subunit IA (0–198.2 mbsf) displays cross-lamination, tilted beds, and convolute deformation. Subunit IB (198.2–383.9 mbsf) is marked by an increase in induration and fracturing, and a decrease in the degree of sorting. Subunit IC (383.9–472.3 mbsf [TD]), marks a return to less consolidated, less fractured, and better sorted sediments. The structural position, age, and composition of the sediments suggest that Site 891 accumulated as proximal Astoria Fan deposits before uplift.

Following uplift and removal of the site from the turbidite depositional regime of the fan, a portion of the uppermost sedimentary section at Site 891 was lost to erosion. Analysis of multichannel seismic line OR-5 indicates that displacement along the frontal thrust fault is about 2.7 km, resulting in 1 km of vertical elevation (throw). A comparison of the seismic sections at Site 891 and in the adjacent portion of Cascadia Basin suggests that about 250–300 m of surficial sediment has been eroded from Site 891, following uplift of the ridge (Fig. 4). The uplift occurred between 75,000 and 300,000 yr ago, based on the convergence rate, the displacement on the fault, and the proportion of shortening accommodated by the frontal thrust vs. that distributed over other faults on the margin. A related estimate based on mass-balance calculations suggests uplift 200,000 yr ago. As the site is positioned in a headless submarine canyon, erosion almost certainly occurred through slope failure, perhaps engendered by tectonically induced excess pore pressure.

Although poor core recovery precludes definition of distinct lithostratigraphic units, the pore-water chemistry and physical properties define three separate zones at Hole 891B. Zone 1 extends from the surface to 200 mbsf. This interval is characterized by (1) porosity that

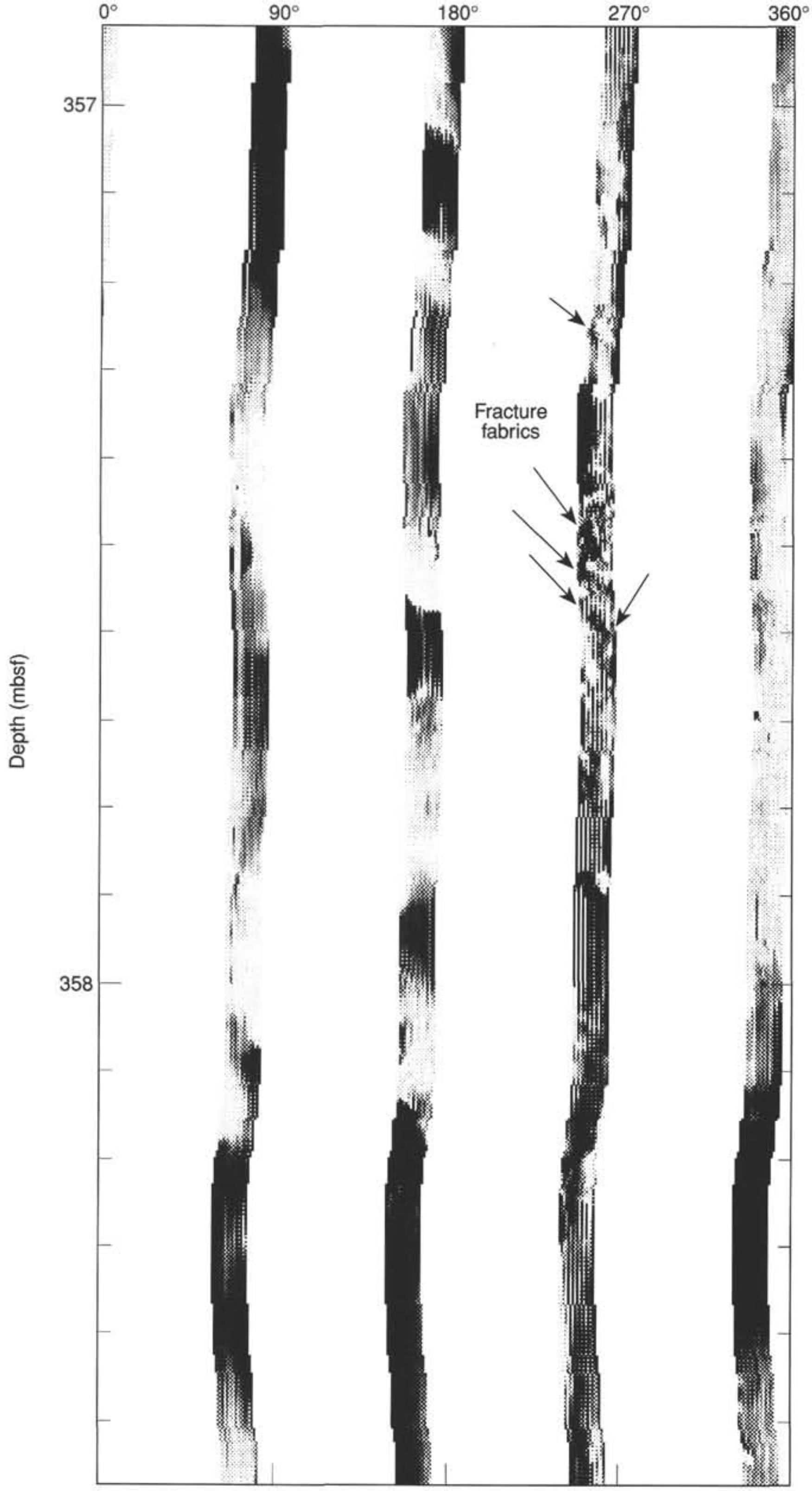

Figure 55. Steeply dipping, parallel planar features demonstrate the highly fractured fabric in the FMS image above the fault zone at 368 mbsf. These fabrics are seen as resistive (light) fragments crosscut by conductive (dark) features.

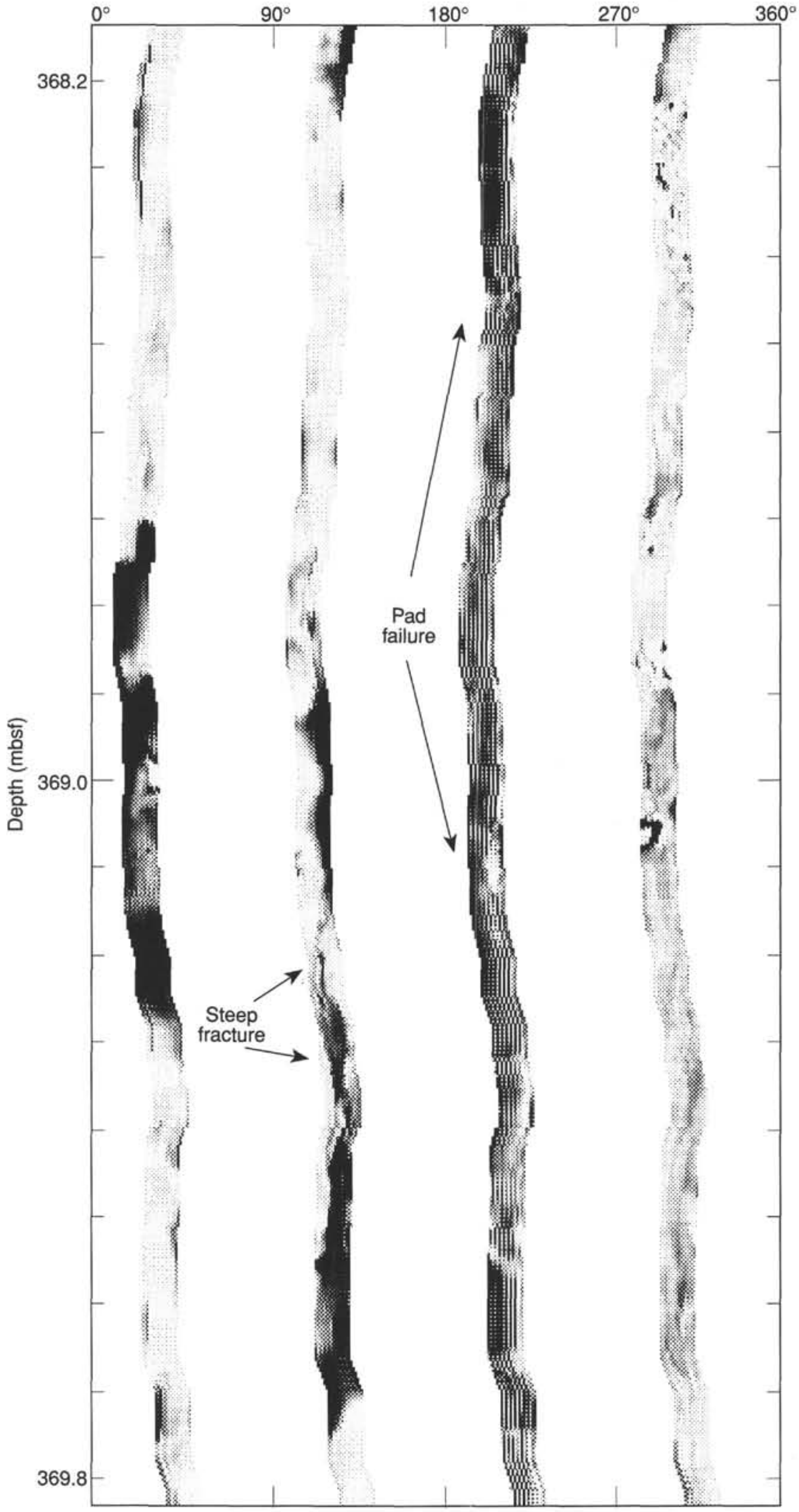

Figure 56. Formation MicroScanner (FMS) image showing a portion of the shear-consolidated fault zone. A conductive pattern representing a steep fracture runs up the southeast side of the borehole (Pad 2). This same fracture pattern is mirrored in Pad 4 at the northwest side of the hole. Vertical conductive features in this diagram are interpreted as steep fractures within the resistive sediment.

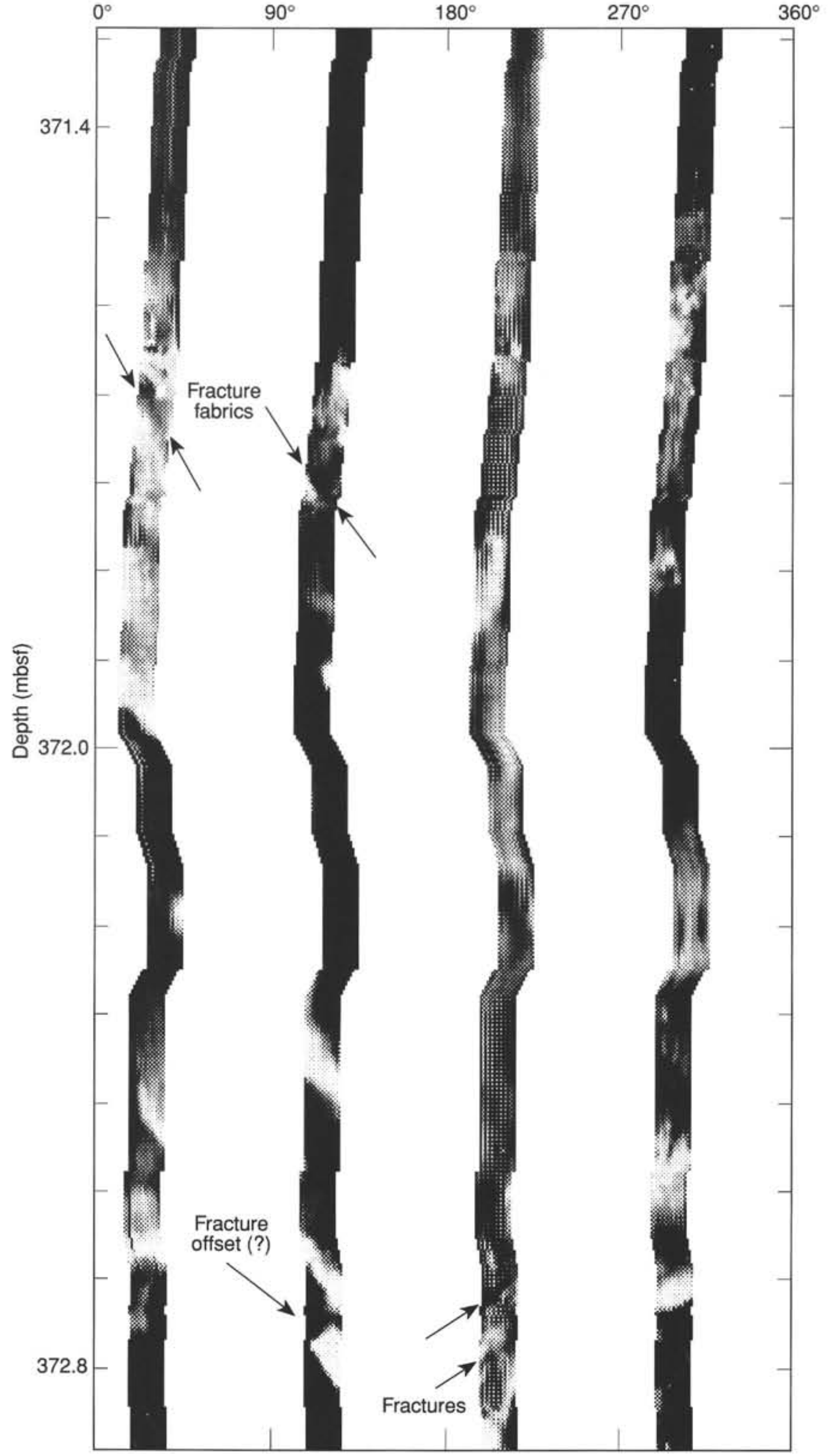

Figure 57. FMS image showing steeply dipping resistive layers that could be fractured bedding surfaces. Also visible are offsets, possibly microfaults, within both resistive and conductive layers.

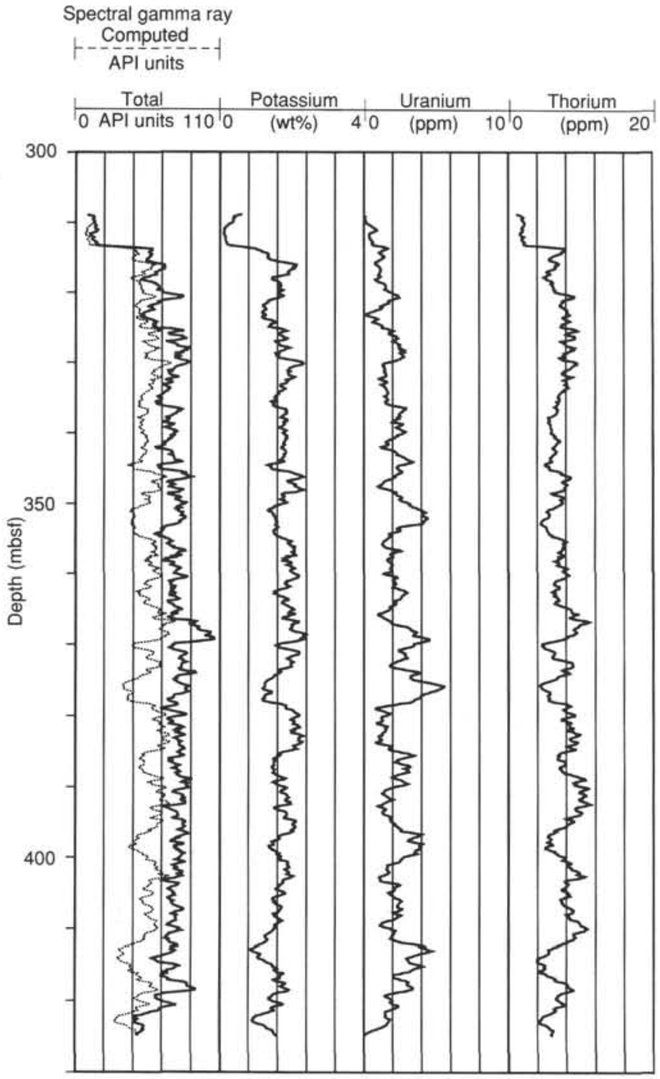

Figure 58. Processed natural gamma-ray data from Hole 891C.

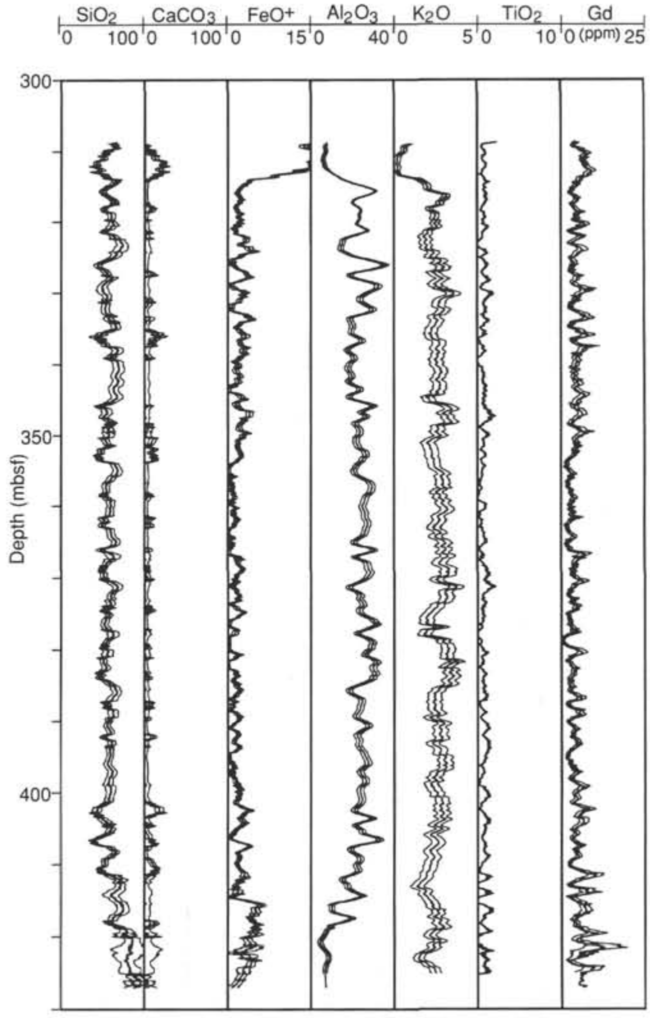

Figure 59. Estimates of calcium carbonate and major-oxide weight fractions from geochemical logs, Hole 891C.

declines regularly from about 50% at the seafloor to about 38% at depth (Fig. 39); (2) low concentrations of methane (2–8 ppmv), a virtual absence of higher hydrocarbons, and <5,000-ppmv carbon dioxide (Fig. 32); and (3) a low Cl^- concentration that increases regularly with depth from about 530 to 546 mM (Fig. 38), the presence of sulfate (10–28 mM, whereas below 200 mbsf sulfate is absent; Fig. 38), alkalinity is less than 10 mM (Fig. 38), and a stable Mg/Ca ratio between 5 and 6 (Fig. 38). Zone 1 appears to be a region of normal gravitational compaction that is dominated by sulfate reduction. A small, but distinct, discontinuity at 130 mbsf in the Cl^-, Mg/Ca, Li, and sulfate profiles suggests advective flow, probably along bedding, as there is no evidence in the cores or profiles of faults.

Zone 2, the interval between 200 and 440 mbsf, differs markedly from the overlying Zone 1, a fact that suggests little hydraulic communication between the two sections. Methane concentrations increase abruptly in Zone 2 to values that range from about 1000 to 56,000 ppmv (Fig. 32). The variability in the concentration of methane is high in this interval, but in general the values are sympathetic with variations in the organic carbon content (0.2–0.8 wt%), which indicates bacterial methanogenesis. Ethane, higher hydrocarbons, and carbon dioxide appear below 240 mbsf and reach maxima at 314, 340, 367, and 410 mbsf. These maxima define thermogenic (hydrothermal) hydrocarbon incursions that indicate fluid advection (Fig. 36). The presence of the olefin ethene (C_2H_4), which is unstable over geological time intervals, suggests that the fluid flow system is active. The total nitrogen/organic carbon ratio indicates that the organic components have a mixed terrestrial/marine origin. The Cl^- concentrations in Zone 2 are relatively constant at about 556 mM, well above the local bottom-water chlorinity of 541 mM (Fig. 38). These values, the abrupt disappearance of sulfate at 200 mbsf, and a complementary increase in alkalinity (from 6 to 27 mM) indicate that Zone 2 waters belong to a separate hydrogeologic system from those in Zone 1, and the interface between the two shows little evidence of diffusion between them. A marked decrease in Ca^{2+} and Mg^{2+} and the alkalinity change at about 200 mbsf suggest carbonate cementation, which may be reflected in the high velocities (2.2 km/s) and resistivities (2.6 Wm) recorded in the logs at 191 mbsf (Fig. 49).

The porosity distribution exhibits several discontinuities (at 260, 308, 375, and 440 mbsf) in Zone 2 that reflect fault zones or intervals of anomalous compaction (Fig. 39). The seismic data indicate that the position of the main frontal thrust fault occurs at about 375 mbsf, but apparently some secondary faults or splays from the frontal thrust cut the section at higher levels in Zone 2. Only the upper two discontinuities are apparent in the pore water (Li, Mg/Ca ratio, and silica) or gas (ΣC_2–C_6) chemistry and probably reflect advective flow along permeable faults or sand beds. The lack of a significant geochemical

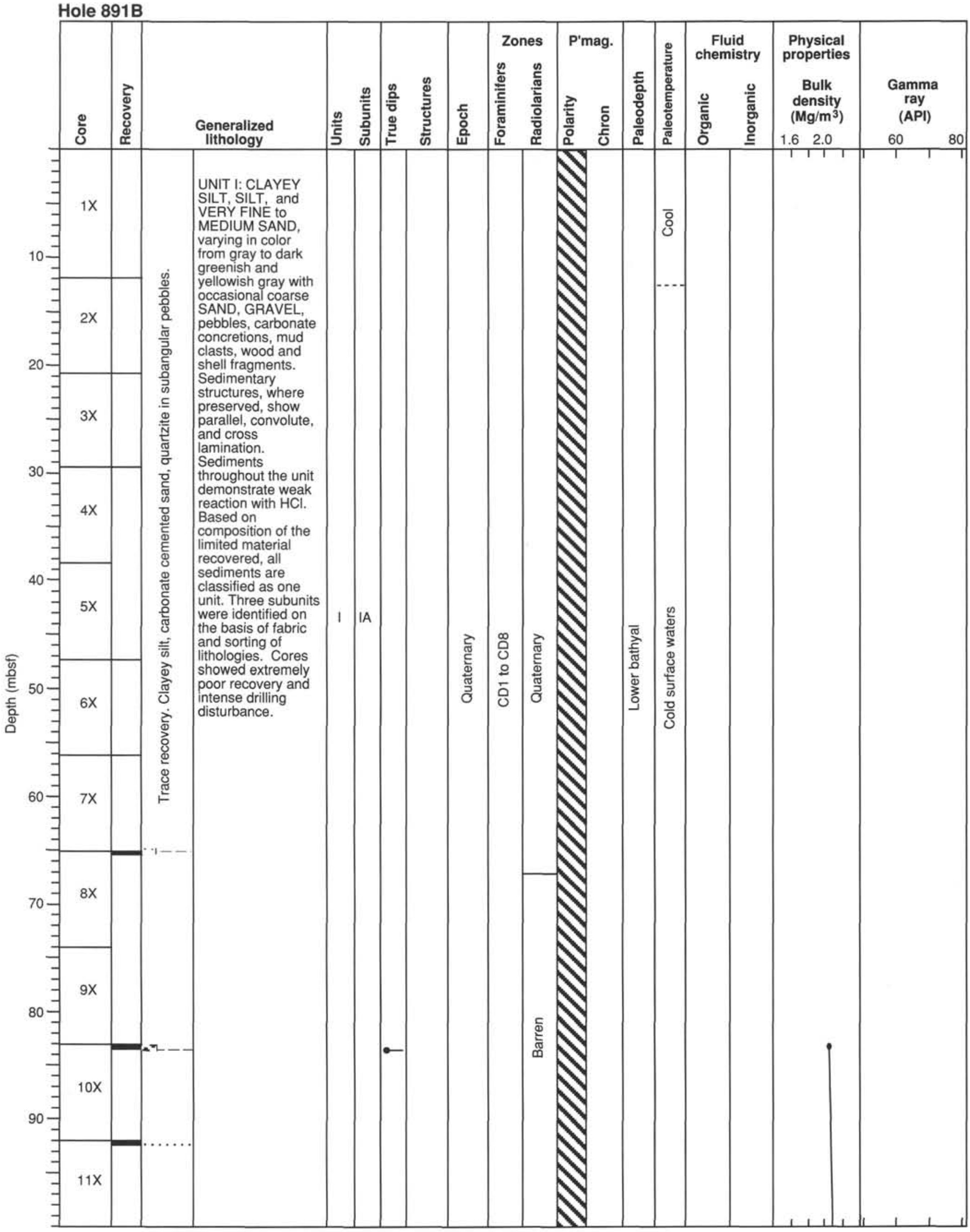

Figure 60. Master chart, Hole 891B.

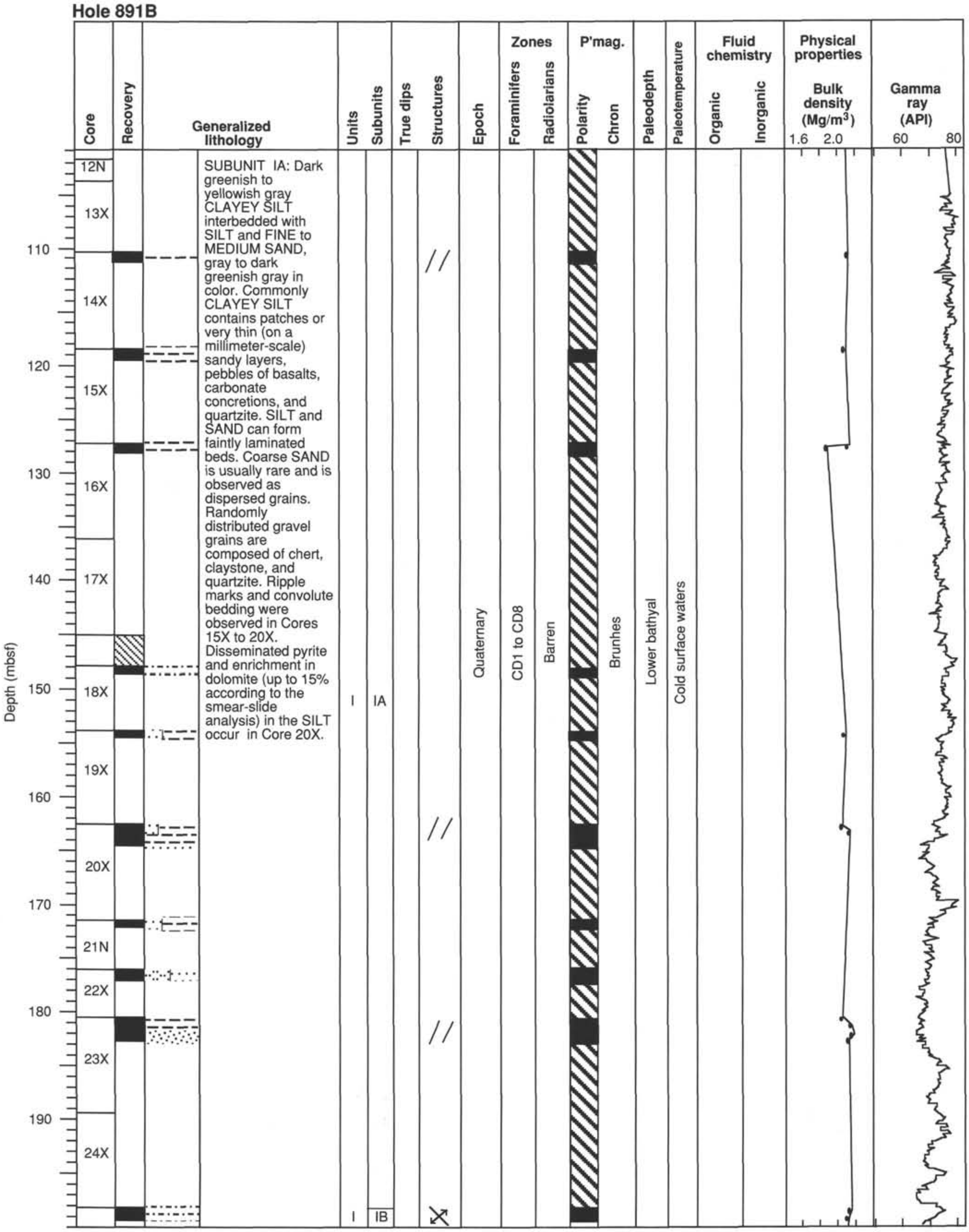

Figure 60 (continued).

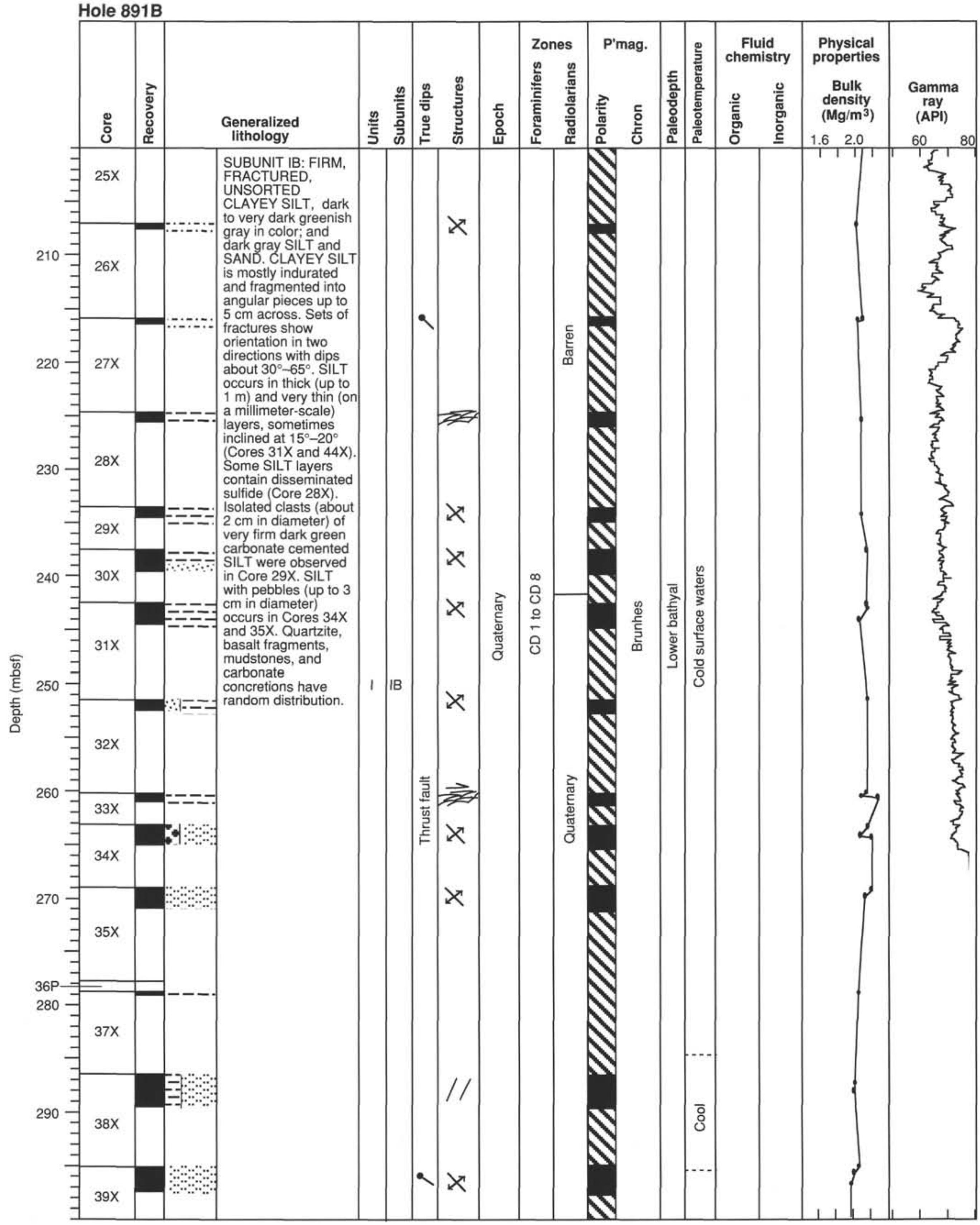

Figure 60 (continued).

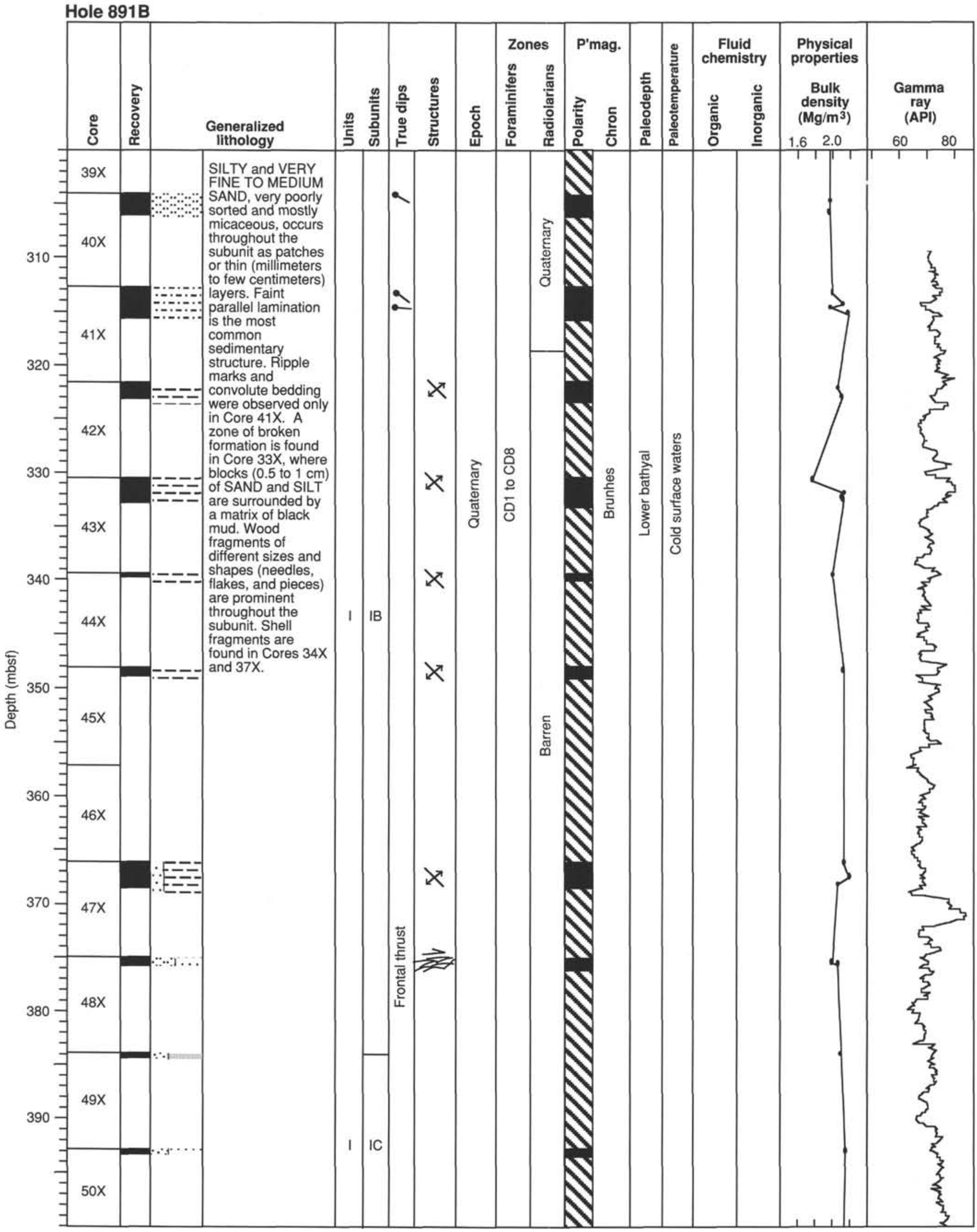

Figure 60 (continued).

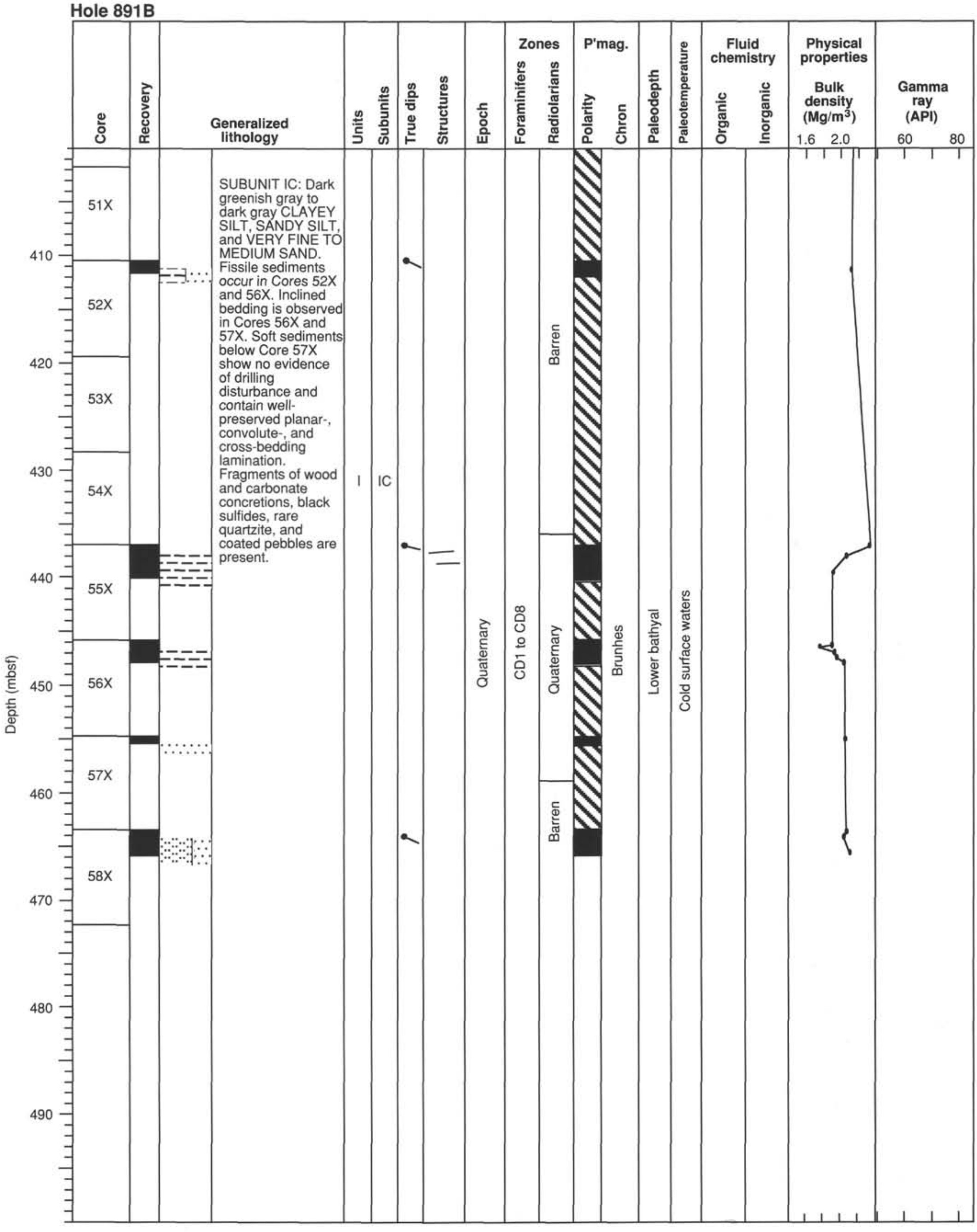

Figure 60 (continued).

anomaly at 375 mbsf suggests that the main thrust imaged on the seismic-reflection profile may support little or no fluid flow. The thrust is particularly well-defined in the records from the logs (370 mbsf), however, by strong positive anomalies in sonic velocity, resistivity, density, and natural gamma ray (Fig. 49). The log data imply an undilated fault zone defined by a tightly compacted (sheared) fault gouge rich in clays.

Zone 3 lies below 440 mbsf, and is defined primarily on the basis of a pronounced increase in porosity (from 40% to 60%) at this depth, followed by a sharp decline below (Fig. 39). A VSP-derived sonic velocity of about 1500 m/s in this zone confirms the porosity increase. Fluids beneath this boundary exhibit consistently high values of methane (30,000–40,000 ppmv) and low concentrations of higher hydrocarbons (<2.5 ppmv) and carbon dioxide (<5000 ppmv; Fig. 32). The pore waters are also characteristically low in Cl^- and high in Ca^{2+}, suggesting that they have been affected by clay dehydration reactions. Because there was no core recovery between 412 and 437 mbsf, the upper boundary of this zone is undefined. Zone 3 appears to represent the footwall section beneath ethe frontal thrust fault. The porosity inversion and geochemical signature suggest that the active portion of the frontal thrust may have stepped down to the section between 412 and 437 mbsf.

Structural analysis of the cores defines moderately steep bedding (about 40°) above 84 mbsf, overlying variable bedding dips (0°–50°; Fig. 21). Deformation bands appear sporadically in the lower half of Zone 1, but there are no other strain indicators in this interval. In contrast, Zone 2 exhibits numerous discrete fractures within the intervals 200–278 and 321–375 mbsf. Two fault zones were recognized within these two intervals at 263 and 375 mbsf by the development of shear fabrics and polished and slickenlined surfaces. Between the two fractured intervals (278–321 mbsf), no scaly fractures occur, but the development of a bedding plane fissility suggests a compaction fabric. Below 375 mbsf, few fractures were observed and bedding dips 14°–20°.

No successful in-situ temperature measurements were made at Site 891.

Although only three cores were recovered from Hole 891A, the pore-water chemistry (Cl^-, Si, phosphate, Mg^{2+}, Na^+, and Ca^{2+}) is substantially different from that characteristic of seawater, or of Zone 1 in Hole 891B. Rather, the concentrations are consistent with those observed in Zone 2, suggesting a minimum depth of origin of 200 mbsf. As Site 891 was drilled near the wall of the submarine canyon where fluid seeps have been observed from a submersible, it appears that Hole 891A sampled a fluid discharge zone. The disparity in pore-water composition between Holes 891A and 891B, which were laterally separated by about 30 m, emphasizes the spatial heterogeneity of fluid flow in this setting.

In summary, Site 891 represents a tectonically and hydrogeologically active setting at the toe of the Cascadia accretionary wedge. Although hanging-wall uplift and folding associated with seaward movement along the thrust ramp have simply tilted the beds in the upper 200 m of the section, at greater depths fabric modification and fluid flow are apparent. Fluids containing young, thermogenic gas are introduced at specific levels above 440 mbsf along fault splays or stratigraphic aquifers. The occurrence of hydrocarbon gases ranging from ethane through hexane, and the immaturity of the autochthonous kerogen and bitumen, requires that the fluids were derived from greater depths, probably from beneath the accretionary wedge. The primary fault zone, imaged on seismic-reflection profiles at 375 mbsf, sampled by coring, and characterized by logging, appears not to be a significant fluid pathway at the present time. Because the footwall (>440 mbsf) is geochemically distinct, however, we infer that the active portion of the frontal thrust fault has stepped down to the interval between 412 and 437 mbsf.

REFERENCES*

Archie, G.E., 1942. The electrical resistivity log as an aid in determining some reservoir characteristics. *Trans. Am. Inst. Min. Metall. Pet. Eng.*, 146:54–62.

Bouma, A.H., 1962. *Sedimentology of Some Flysch Deposits: A Graphic Approach to Facies Interpretation*: Amsterdam (Elsevier).

Bristow, J.F., Broglia, C., deMenocal, P.B., and Pratson, E.L., 1992. Data report: geochemical logging results from the Sea of Japan: Sites 798 and 799. *In* Tamaki, K., Suyehiro, K., Allan, J., McWilliams, M., et al., *Proc. ODP, Sci. Results,* 127/128 (Pt. 2): College Station, TX (Ocean Drilling Program), 1395–1410.

Brückmann, W., 1989. Typische Kompakationsmuster mariner Sedimente und ihre Modifikation in einem rezenten Akkretionskeil (Barbados Ridge). *Beitr. Geol. Inst. Univ. Tübingen, Rh. A,* 5:1–135.

Cande, S.C., and Kent, D.V., 1992. A new geomagnetic polarity time scale for the Late Cretaceous and Cenozoic. *J. Geophys. Res.,* 97:13917–13951.

Carson, B., Holmes, M.L., Umstattd, K., Strasser, J.C., and Johnson, H.P., 1991. Fluid expulsion from the Cascadia accretionary prism: evidence from porosity distribution, direct measurements, and GLORIA imagery. *Trans. R. Soc. London A,* 335:331–340.

Claypool, G.E., and Kaplan, I.R., 1974. The origin and distribution of methane in marine sediments. *In* Kaplan, I.R. (Ed.), *Natural Gases in Marine Sediments:* New York (Plenum), 99–140.

Dekkers, M., 1988. Some rock-magnetic properties of fine-grained hematite, goethite, and pyrrhotite [Ph.D. dissert.]. Univ. of Utrecht.

Goldfinger, C., Kulm, L.D., Yeats, R.S., Applegate, B., MacKay, M.E., and Moore, G.F., 1992. Transverse structural trends along the Oregon convergent margin: implications for Cascadia earthquake potential and crustal rotations. *Geology,* 20:141–144.

Grau, J.A., and Schweitzer, J.S., 1989. Elemental concentrations from thermal neutron capture gamma-ray spectra in geological formations. *Nucl. Geophys.,* 3:1–9.

Grau, J.A., Schweitzer, J.S., and Hertzog, R.C., 1990. Statistical uncertainties of elemental concentrations extracted from neutron-induced gamma-ray measurements. *IEEE Trans. Nuclear Sci.,* 37:2175–2178.

Hertzog, R., Colson, L., Seeman, B., O'Brien, M., Scott, H., McKeon, D., Wraight, J., Grau, J., Ellis, D., Schweitzer, J., and Herron, M., 1989. Geochemical logging with spectrometry tools. *SPE Formation Evaluation,* 4:153–162.

Karig, D.E., and Lundberg, N., 1990. Deformation bands from the toe of the Nankai accretionary prism. *J. Geophys. Res.,* 95:9099–9109.

Kent, D., Opdyke, N.D., and Ewing, M., 1971. Climatic change in the North Pacific using ice-rafted detritus as a climatic indicator. *Geol. Soc. Am. Bull.,* 82:2741–2754.

Kulm, L.D., Suess, E., Moore, J.C., Carson, B., Lewis, B.T., Ritger, S.D., Kadko, D.C., Thornburg, T.M., Embley, R.W., Rugh, W.D., Massoth, G.J., Langseth, M.G., Cochrane, G.R., and Scamman, R.L., 1986. Oregon subduction zone: venting, fauna, and carbonates. *Science,* 231:561–566.

Kulm, L.D., von Huene, R., et al., 1973. *Init. Repts. DSDP,* 18: Washington (U.S. Govt. Printing Office).

Lagoe, M.B., and Thompson, P.R., 1988. Chronostratigraphic significance of Late Cenozoic planktonic foraminifera from the Ventura Basin, California: potential for improving tectonic and depositional interpretation. *J. Foraminiferal Res.,* 18:250–266.

Lewis, B.T.R., and Cochrane, G.R., 1990. Relationship between the location of chemosynthetic benthic communities and geologic structure on the Cascadia subduction zone. *J. Geophys. Res.,* 95:8783–8793.

Lock, G.A., and Hoyer, W.A., 1971. Natural gamma-ray spectral logging. *The Log Analyst,* 12:3–9.

Lovell, M.A., 1985. Thermal conductivity and permeability assessment by electrical resistivity measurements in marine sediments. *Mar. Geotechnol.,* 6:205–241.

Lundberg, N., and Moore, J.C., 1986. Macroscopic structural features in Deep Sea Drilling Project cores from forearc regions. *In* Moore, J.C. (Ed.), *Structural Fabrics Preserved in Deep Sea Drilling Project Cores from Forearcs.* Mem.—Geol. Soc. Am., 166:13–44.

*Abbreviations for names of organizations and publication titles in ODP reference lists follow the style given in *Chemical Abstracts Service Source Index* (published by American Chemical Society).

MacKay, M.E., Moore, G.F., Cochrane, G.R., Moore, J.C., and Kulm, L.D., 1992. Landward vergence and oblique structural trends in the Oregon margin accretionary prism: implications and effect on fluid flow. *Earth Planet. Sci. Lett.*, 109:477–491.

Marlowe, I.T., Brassell, S.C., Eglinton, G., and Green, J.C., 1984. Long-chain unsaturated ketones and esters in living algae and marine sediments. *In* Schenck, P.A., de Leeuw, J.W., and Lijmbach, G.W.M. (Eds.), *Advances in Organic Geochemistry 1983.* Org. Geochem., 6:135–141.

Moore, J.C., Brown, K.M., Horath, F., Cochrane, G., MacKay, M., and Moore, G.F., 1991. Prisms: effects of permeability variations. *Philos. Trans. R. Soc. London,* 335:275–288.

Moore, J.C., Orange, D., and Kulm, L.D., 1990. Interrelationship of fluid venting and structural evolution: *Alvin* observations from the frontal accretionary prism. *J. Geophys. Res.*, 95:8795–8808.

Musgrave, R.J., Delaney, M., Stax, R., and Tarduno, J.A., 1993. Magnetic diagenesis, organic input, interstitial water geochemistry, and paleomagnetic record of the carbonate sequence of the Ontong Java Plateau. *In* Berger, W.H., Kroenke, L.W., Mayer, L.A., et al., *Proc. ODP, Sci. Results,* 130: College Station, TX (Ocean Drilling Program), 527–546.

Mutti, E., and Ricci Lucchi, F., 1972. Le torbiditi dell'Appennino settentrionale: introduzione all'analisi di facies. *Mem. Soc. Geol. Ital.,* 11:161–199.

Oremland, R.S., Whiticar, M.J., Strohmaier, F.E., and Kiene, R.P., 1988. Bacterial ethane formation from reduced, ethylated sulfur compounds in anoxic sediments. *Geochim. Cosmochim. Acta,* 52:1895–1904.

Pratson, E.L., Broglia, C., and Jarrard, R., 1993. Geochemical well logs through Cenozoic and Quaternary sediments from Sites 815, 817, 820, 822, and 823. *In* McKenzie, J.A., Davies, P.J., Palmer-Julson, A., et al., *Proc. ODP, Sci. Results,* 133: College Station, TX (Ocean Drilling Program), 795–817.

Ruckebusch, G., 1983. A Kalman filtering approach to natural gamma ray spectroscopy in well logging. *Inst. Electr. Electron. Eng.* [trans., on autom. contl.], AC-28(3):372–380.

Schweitzer, J.S., Grau, J.A., and Hertzog, R.C., 1988. Precision and accuracy of short-lived activation measurements for in situ geological analyses. *J. Trace Microprobe Techniques,* 6:437–451.

Scott, H.D., and Smith, M.P., 1973. The aluminum activation log. *Log Anal.,* 14:3–12.

Simoneit, B.R.T., 1977. Diterpenoid compounds and other lipids in deep-sea sediments and their geochemical significance. Geochim. Cosmochim. Acta, 41:463–476.

———, 1978. The organic geochemistry of marine sediments. *In* Riley, J.P., and Chester, R. (Eds.), *Chemical Oceanography* (2nd ed.) (Vol. 7): London (Academic Press), 233–311.

Suess, E., von Huene, R., et al., 1988. *Proc. ODP, Init. Repts.,* 112: College Station, TX (Ocean Drilling Program).

Suess, E., and Whiticar, M.J., 1989. Methane-derived CO_2 in pore fluids expelled from the Oregon subduction zone. *Palaeogeogr., Palaeoclimatol., Palaeoecol.,* 71:119–136.

Volkman, J.K., Eglinton, G., Corner, E.D.S., and Sargent, J.R., 1980. Novel unsaturated straight-chain C_{37}–C_{39} methyl and ethyl ketones in marine sediments and a coccolithophore *Emiliania huxleyi. In* Douglas, A.G., and Maxwell, J.R. (Eds.), *Advances in Organic Geochemistry 1979:* Oxford (Pergamon Press), 219–228.

von Huene, R., and Kulm, L.D., 1973. Tectonic summary of Leg 18. *In* Kulm, L.D., von Huene, R., et al., *Init. Repts. DSDP:* Washington (U.S. Govt. Printing Office), 961–976.

Whiticar, M.J., in press. Isotope tracking of methanogenesis and methylotrophy. *In* Adams, D.D., Seitzinger, S.P., and Crill, P.M. (Eds.), *Cycling of Reduced Gases in the Hydrosphere:* Stuttgart (Schweizerbart.).

Whiticar, M.J., and Suess, E., 1990. Hydrothermal hydrocarbon gases in the sediments of the King George Basin, Bransfield Strait, Antarctica. *Appl. Geochem.,* 5:135–147.

Zehnder, A.J.B. (Ed.), 1988. *Biology of Anaerobic Microorganisms:* New York (Wiley).

Ms 146IR-009

NOTE: For all sites drilled, core-description forms ("barrel sheets") and core photographs can be found in Section 6, beginning on page 429. Forms containing smear-slide data can be found in Section 7, beginning on page 591.

Hole 891C: Resistivity-Velocity-Natural Gamma Ray Log Summary

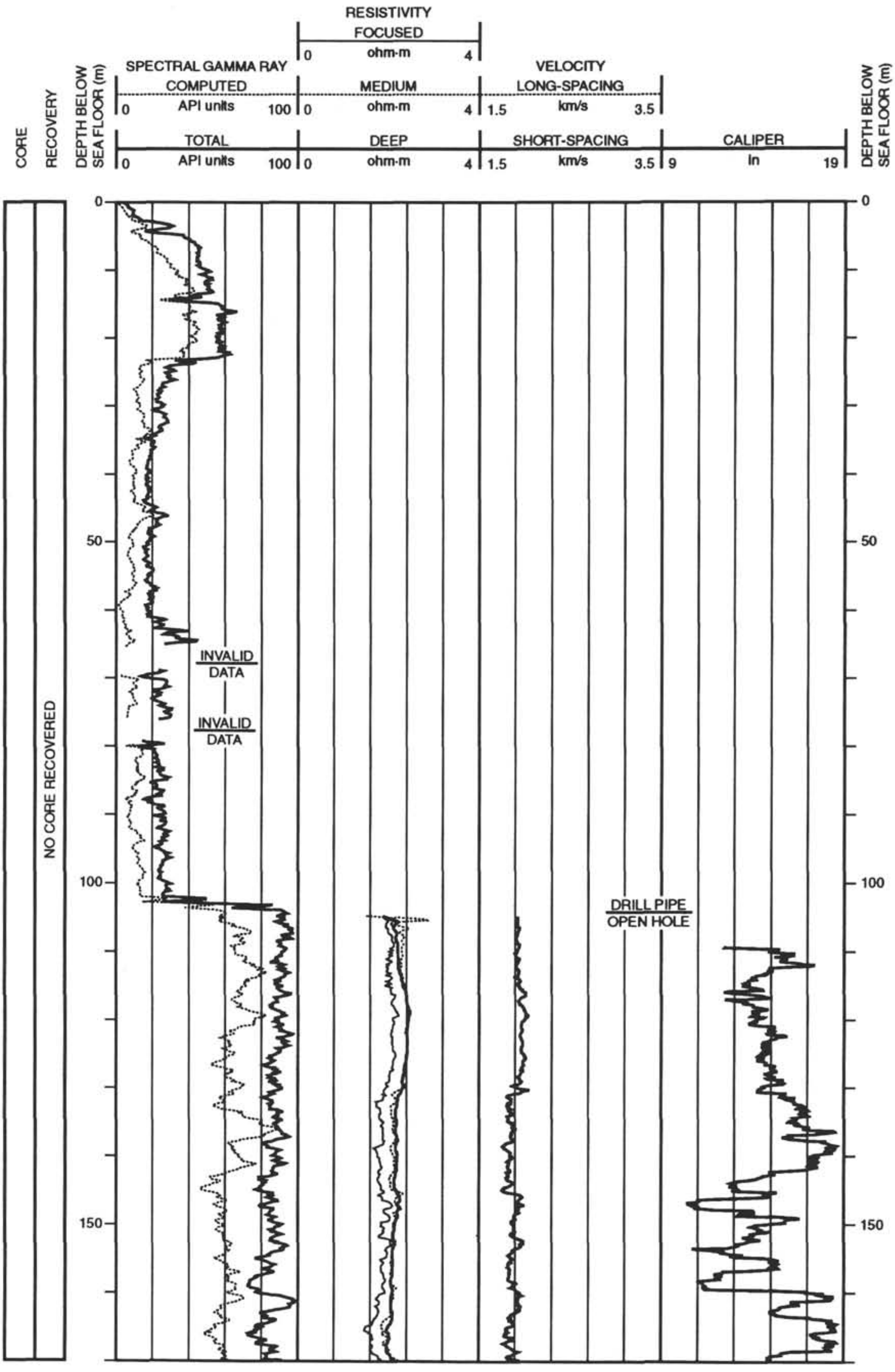

Hole 891C: Resistivity-Velocity-Natural Gamma Ray Log Summary (continued)

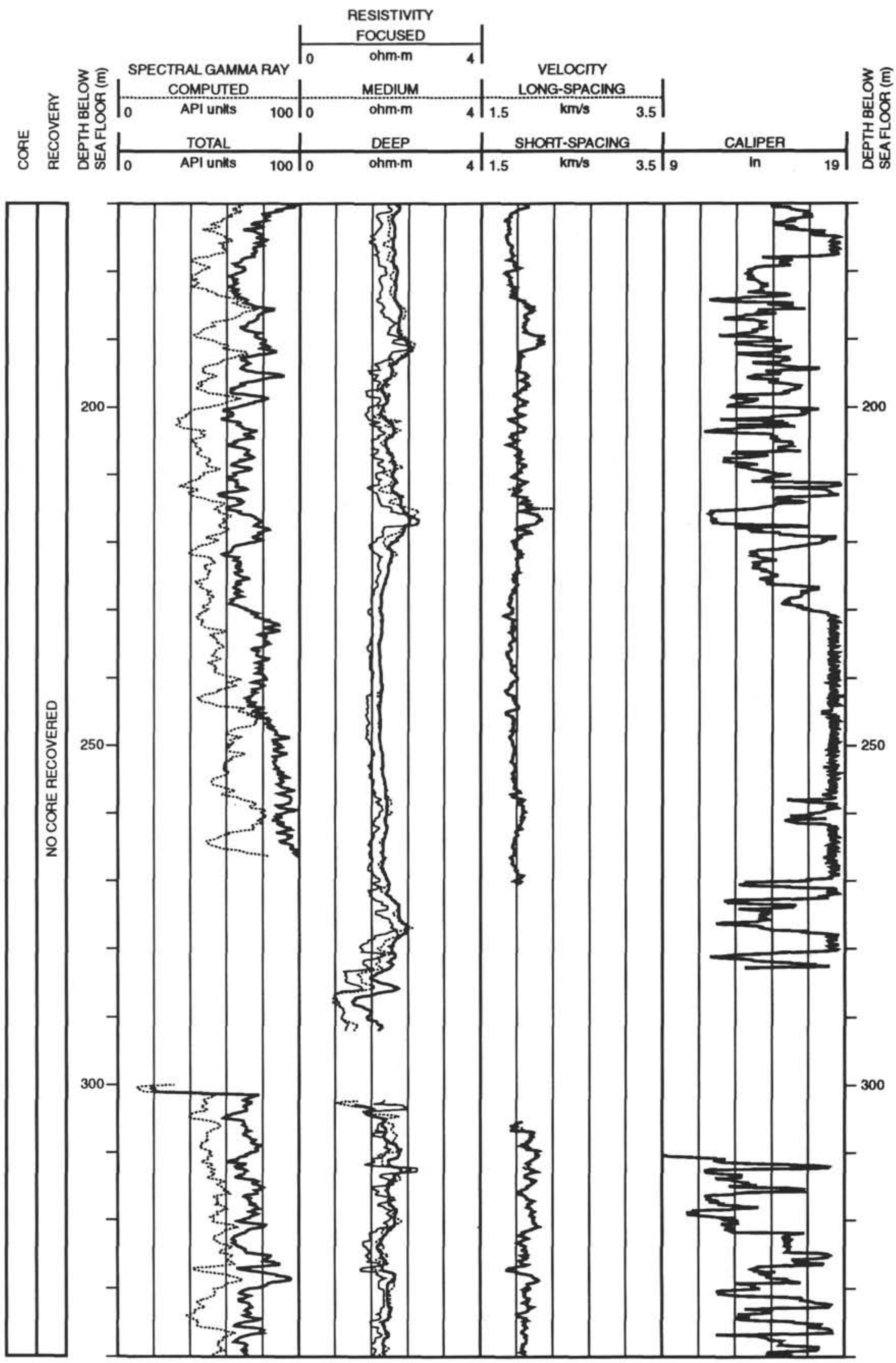

Hole 891C: Resistivity-Velocity-Natural Gamma Ray Log Summary (continued)

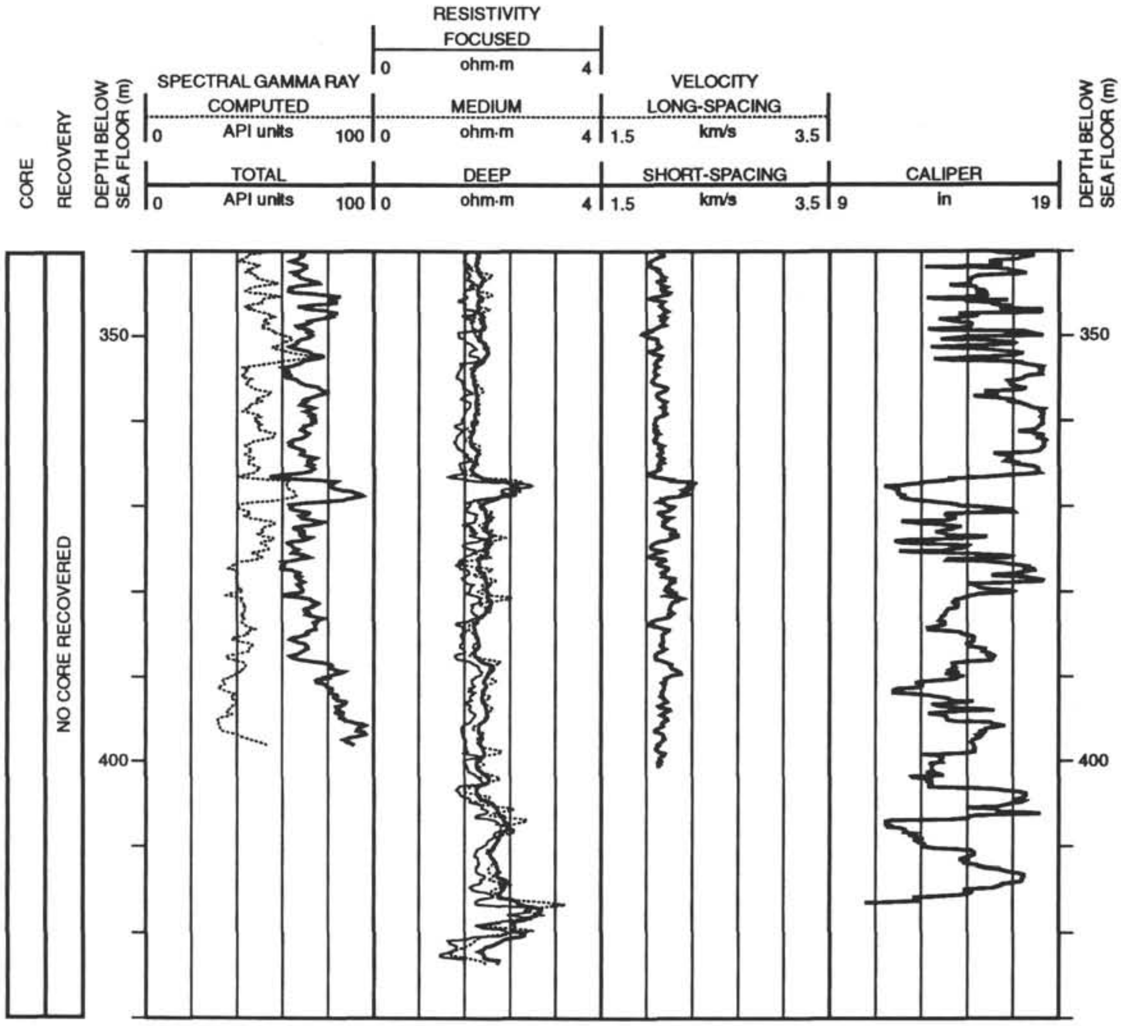

Hole 891C: Density-Porosity-Natural Gamma Ray Log Summary

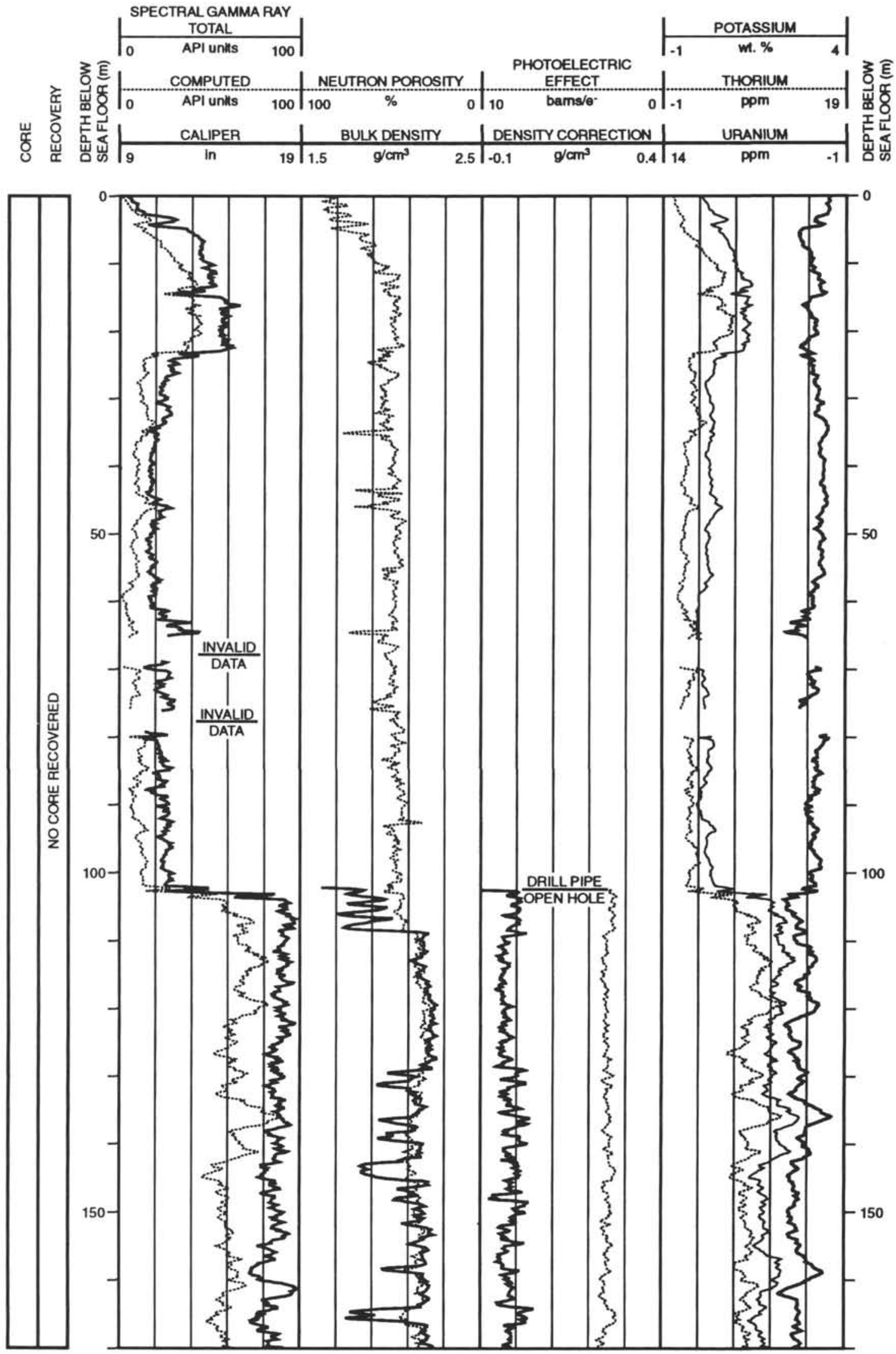

Hole 891C: Density-Porosity-Natural Gamma Ray Log Summary (continued)

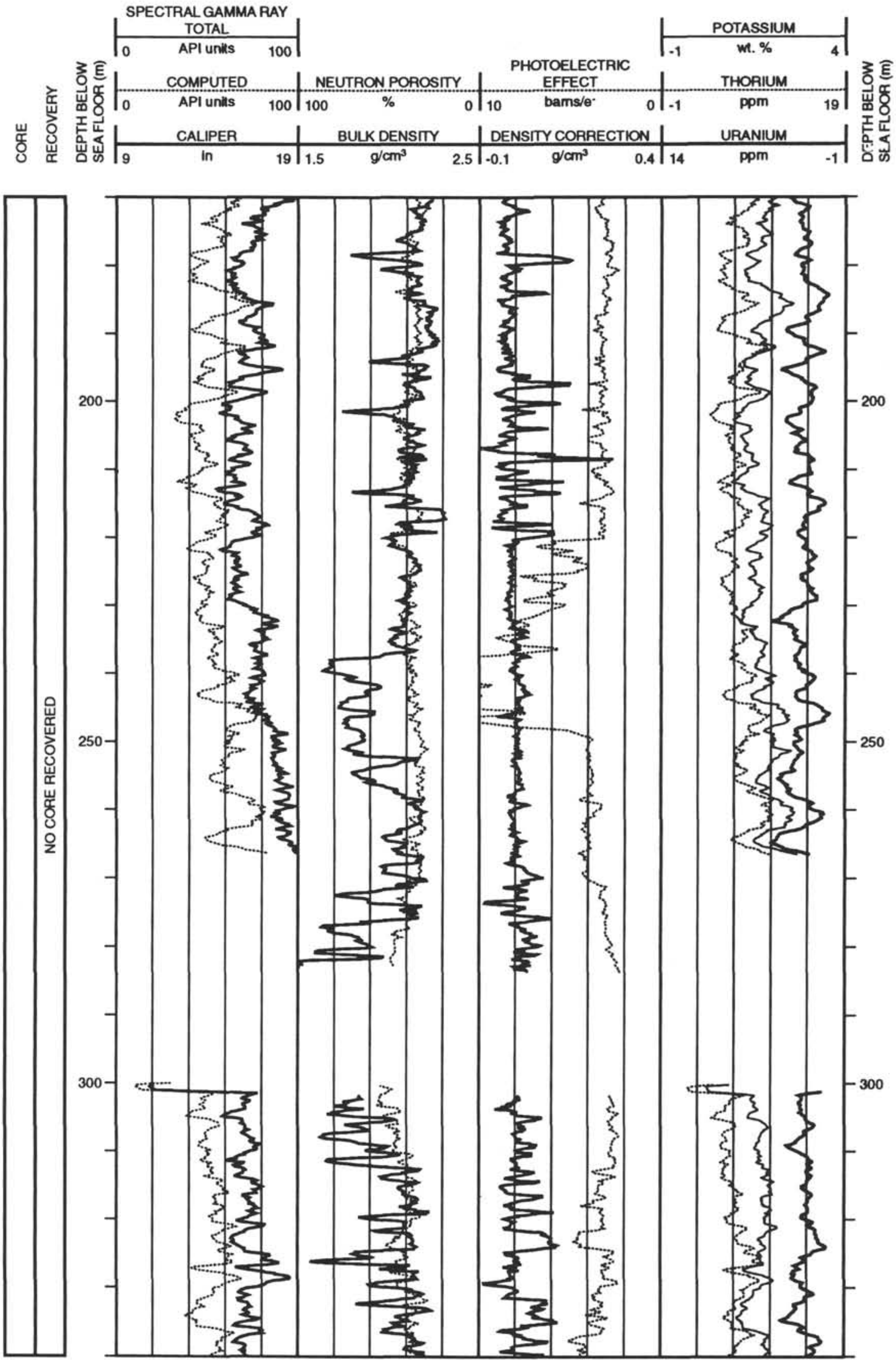

Hole 891C: Density-Porosity-Natural Gamma Ray Log Summary (continued)